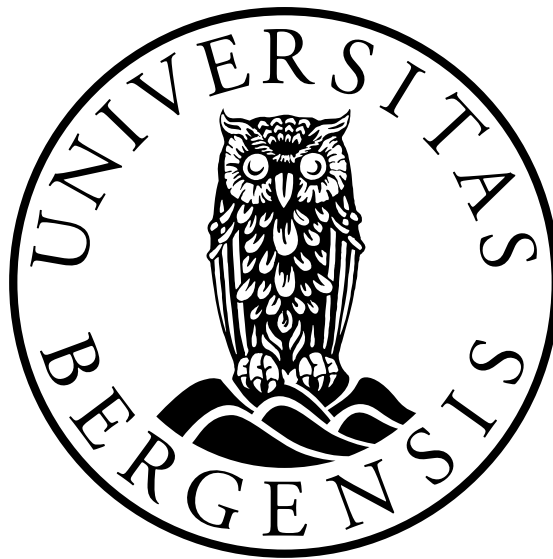# A novel application of Spherical Elementary Currents with Ground Magnetometers − Analysis of By effects on the auroral electrojets

Simon Walker

Thesis for Master Degree in Physics at University of Bergen

2020

Acknowledgements

Simon James Walker
Bergen, November 2020

"Every day sees humanity more victorious in the struggle with space and time"

Guglielmo Marconi

Abstract

This thesis advances inversion and optimisation techniques used with spherical elementary currents (SECS) to perform a statistical analysis of the auroral electrojets based on ground magnetic field measurements. The divergence-free currents in the northern ionosphere above Fennoscandia are modelled using SECS and constrained by measurements from twenty ground magnetometers. A new regularisation technique is implemented that enables the model to find more physical currents.

An electrojet detection algorithm is developed to identify the properties of the auroral electrojets based on the model output. The width, the peak sheet current density and the total current of the electrojet are identified. These electrojet properties are collected with the goal of investigating the so called explicit B_y effect on the electrojets. This effect refers to the influence of IMF B_y polarity on the magnetosphere environment. Studies have shown, using the AL index, that the westward electrojet exhibits an explicit B_y effect that suppresses the westward electrojet during the winter when B_y is negative and, less significantly, during the summer when B_y is positive. Investigations into the eastward electrojet, using the AU index, have shown no B_y effect. The peak SECS derived sheet current density in the westward and eastward electrojet are expected to be similar to the AL and AU indices, respectively. Peaks of the westward electrojet show a variation that is consistent with the explicit B_y effect during the winter but not during the summer. The peaks of the eastward electrojet show no B_y effect in either season and, therefore, agrees with the previous studies. The total current through the electrojets provide an improved measure of the strength of the electrojets. The strength of the eastward electrojet exhibits no clear explicit B_y effect. Whereas, the westward electrojet is stronger during the summer when B_y is negative and, more clearly, when B_y is positive during the winter. The most interesting B_y effect was found within the electrojet widths. During the summer, eastward electrojet is wider when B_y is positive and the westward electrojet is wider when B_y negative. No such effect is seen during the winter. Through the analysis of average sheet current density profiles and statistical ionospheric convection patterns, this behaviour is attributed to the effects of lobe reconnection. Lobe convection cells influence the poleward boundary of the electrojets found using the algorithm. These lobe cells are greatly affected by the polarity of B_y and, consequently, create a B_y effect in the poleward boundary of the electrojets.

This may be the first time such a large time series of divergence-free current maps have been analysed. The new electrojet properties found in this study further our understanding of the B_y effect, while the methodology outlined within this thesis allows for a more effective investigation into divergence-free currents with opportunities to advance the techniques used and expand its application.

Contents

Chapter 1

Introduction

The ionosphere is the portion of the Earth's atmosphere that is ionised, primarily via solar photoionisation of neutral atmospheric gases. The ionosphere is dynamic and highly variable in the auroral regions at high latitudes due to the influence of the solar wind and interplanetary magnetic field (IMF). Interactions between the IMF and the magnetosphere, the region encapsulating the Earth's magnetic field and plasma environments, excite plasma flows and convection within the polar ionosphere. Perhaps the most energetic phenomenon resulting from these interactions is the substorm, a triggered release of energy in the magnetotail that stimulates sunward convection of ionospheric plasma at dawn and dusk.

Currents within the auroral ionosphere are the result of plasma flows in and around the polar cap, and along magnetic field lines at high latitudes that thread both the magnetosphere and the ionosphere. The former (i.e., horizontal ionospheric currents, otherwise known as Hall and Pedersen currents) result from differences in neutral collision frequencies for ions and electrons. They are responsible for closure of the latter (i.e., field-aligned currents). Both Hall and Pedersen currents circulate around the polar cap. Helmholtz decomposition (*Helmholtz*, 1858) can be used to separate the circulating and closure currents respectively into "divergence-free" and "curl-free" components. These different current systems are described in detail in section 2.2. According to Fukushima's theorem (*Fukushima*, 1994), ground-based magnetometers can only measure the divergence-free component of the horizontal currents; they cannot "see" the curl-free component. Therefore, this thesis focuses on the divergence-free part of the current system.

A large limiting factor for ground-based magnetometer measurements is that they cannot produce an overall view of the divergence-free currents. However, a combination of many magnetometers can be used to constrain a representation of 2D divergence-free currents. A system of spherical elementary currents can then be used to represent a divergence-free current system that correspond closely to the measured magnetic field perturbations. This project makes use of the SECS concept, including recent developments presented by *Vanhamäki and Juusola* (2020), and applies it to a selection of twenty ground based magnetometers in Fennoscandia to produce robust estimates of the equivalent currents and radial magnetic field perturbations along a fixed magnetic meridian of $105°$ magnetic longitude.

The most common methodology for constraining the SECS model is compared with a new technique that utilises prior knowledge of typical ionospheric current structure to

encourage more physical solutions. These methods are discussed in detail in Chapter 3, where it is also shown that 1) regularisation can be used to discourage variations in the east-west component of the divergence-free current, and 2) both methods discourage large changes over a small spatial area. The methodology that allows the SECS model to account for the effect that currents within the Earth (which are primarily induced by the ionosphere) have on magnetometer measurements are presented in detail.

Here the SECS technique is used with a consistent set of twenty magnetometers in Fennoscandia. A static set of magnetometers allows for differences within the results to be attributed to a change of driving conditions, such as solar wind velocity or IMF vector, rather than a change in data availability and model geometry. In other words, the problems that variable data coverage would otherwise introduce are eliminated by using a consistent set of magnetometers.

The modelled divergence-free currents and radial magnetic field perturbations are then evaluated along the magnetic meridian ($105°$) for which the density of ground-based magnetometers is greatest. This is done to reduce the spatial domain of the SECS output, as model output on a two-dimensional grid would increase the required computational time without any clear scientific advantage: the model is less accurate farther from magnetometer measurements, and as such it is difficult to consistently interpret model output across a longitudinally extended region. In contrast, using a fixed set of points in relation to the location of magnetometers sites, as has been done here, enables comparison of model output at different times.

The specific sites chosen allow for a derivation of statistics covering almost twenty years at a temporal resolution of one minute. There are a vast array of investigations that can be made from the estimated meridian equivalent currents and radial magnetic field perturbations. An example time series, in section 3.7.1, shows that these estimates provide a unique view of substorm dynamics and ultra low frequency (ULF) waves, and opens new possibilities for investigating these phenomena.

Recent work within the Dynamics of the Asymmetric Geospace at the Birkeland Centre for Space Science, where this study has been carried out, and other recent work have investigated the "explicit B_y effect" (*Holappa and Mursula*, 2018; *Holappa et al.*, 2020a; *Liou et al.*, 2020; *Reistad et al.*, 2020). This effect refers to differences in the magnetospheric and ionospheric response to different IMF B_y polarities. Observed manifestations of this effect include a suppression of the westward electrojet, as indicated by the auroral lower (AL) index, and increased substorm occurrence for a specific combinations of B_y polarity and dipole tilt.

Discussions of the underlying cause have pointed to possible differences in solar wind-magnetosphere coupling on the dayside and magnetotail stability as a result of different B_y polarity. These could be starting points in seeking an explanation for the explicit B_y effect; it is nevertheless clear that further investigation is required. With that it mind, this study uses the SECS model generated to verify current observations of the explicit B_y effect and create a unique data product that explores how different IMF B_y polarities affect the electrojets.

To go beyond a statistical overview of divergence-free currents in the northern hemisphere across all magnetic local times, an algorithm that extracts basic properties of the auroral electrojet, including width, peak amplitude, total current and the occurrence of multiple electrojets, is devised chapter 3.

Using statistics of these electrojet properties, it is shown that the response of the

peak amplitude and total current of the electrojet to changes in the polarity of B_y verify the findings of previous studies. The eastward electrojet peak amplitude and total current exhibit no explicit B_y effect, as expected, while the total current of the westward electrojet displays a dependence on IMF B_y polarity that agrees with statistics presented by *Holappa and Mursula* (2018). The widths of the electrojets, on the other hand, display a previously unreported seasonal dependence on IMF B_y polarity. Both the westward and eastward electrojet widths vary greatly during the summer depending on the polarity of B_y while there is no clear dependence during the winter. This observation can be attributed to ionospheric convection cells that are driven by lobe reconnection being favoured more than typical Dungey cycle cells in the summer.

Last, it has long been known that strong geomagnetic events that drive large ionospheric currents can cause considerable damage to critical infrastructure, including power grids and gas pipes. There is therefore a need to understand what controls the behaviours of these currents, as increased knowledge leads to improvements in the design of affected technology and to better preparation for these events.

Chapter 2

Background Physics

In this chapter the core physical concepts relevant to this study will be outlined and discussed.

2.1 The Solar Wind and The Magnetosphere

The two most significant influences our Sun has on the Earth's magnetosphere-ionosphere system are through 1) solar radiation (most importantly extreme ultraviolet), and 2) the solar wind and its accompanying interplanetary magnetic field (IMF). Solar activity—including, for example, sunspots and coronal mass ejections—follows a cyclic variation with an average frequency of 11 years. This cycle is related to a reversal in the polarity of the Sun's magnetic field, which occurs every 22 years on average. Evidence that the Sun has a direct impact on the Earth and near Earth environment can be found by looking for this 11-year solar cycle in measurable properties of the ionosphere and magnetosphere. The fact that solar variability and magnetospheric changes are linked has been known for over 150 years. The first description of this connection was given by Sabine in 1852, who reported that a reduction in the number of sunspots on the solar surface correlated with a reduction in magnetic field disturbances (*Milan et al.*, 2004). Solar radiation heavily influences ionospheric plasma density, as it is the primary source of photons for the process of photo-ionisation. The solar wind and IMF are the primary drivers for the shape and dynamics of the magnetosphere and near-Earth plasma flows.

2.1.1 Magnetic Reconnection

Magnetic reconnection is an important process in IMF-magnetosphere coupling, although it is far from unique to this area of research. Magnetic reconnection occurs when magnetic field lines of opposing field polarity interact with sufficient pressure forces. Figure 2.1 shows magnetic reconnection in two stages and how magnetic field lines reconnect to form new magnetic structures.
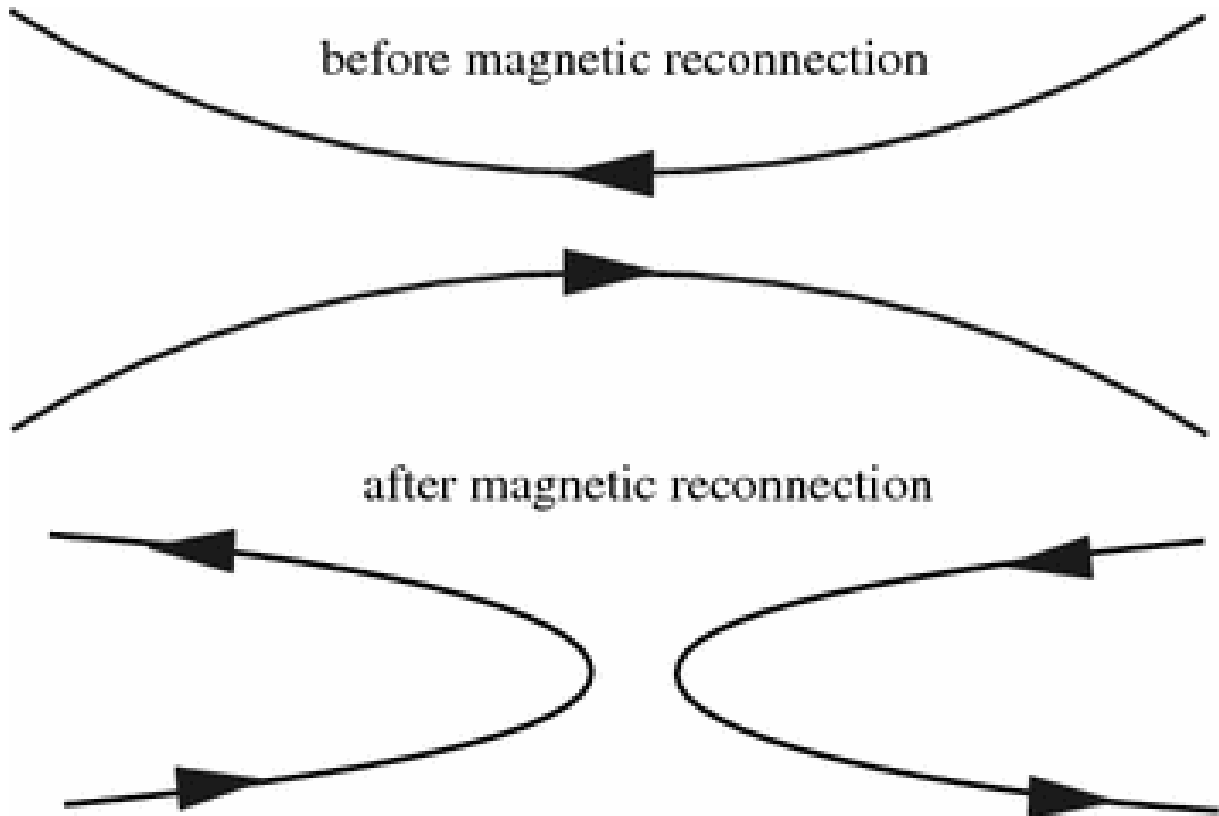
Figure 2.1: A diagram that simplifies magnetic reconnection into two stages, taken from Wang (2016)

Figure 2.2 shows magnetic reconnection using the Sweet-Parker model. The Sweet-Parker model was developed in 1956 and was one of the earliest attempts to encapsulate the dynamics of the interface of opposing magnetic field lines (*Kulsrud*, 2001; *Loureiro and Uzdensky*, 2015). Although there have been a large number of attempts to improve upon this model, some of which have been shown to describe phenomena that the Sweet-Parker model cannot, the core concepts of the reconnection process have remained consistent. Between the opposing magnetic field lines a current sheet forms to accommodate the change in magnetic field. Magnetic flux is directed into the current sheet towards an area called the diffusion region. Within this region ideal magnetohydrodynamics (MHD) breaks down and magnetic field lines are no longer frozen into the plasma. It is within this region that magnetic field lines reconnect (*Biskamp*, 1994). There is a magnetic flux outflow from the diffusion region where newly reconnected field flow away from the reconnection site and bringing plasma along with it.
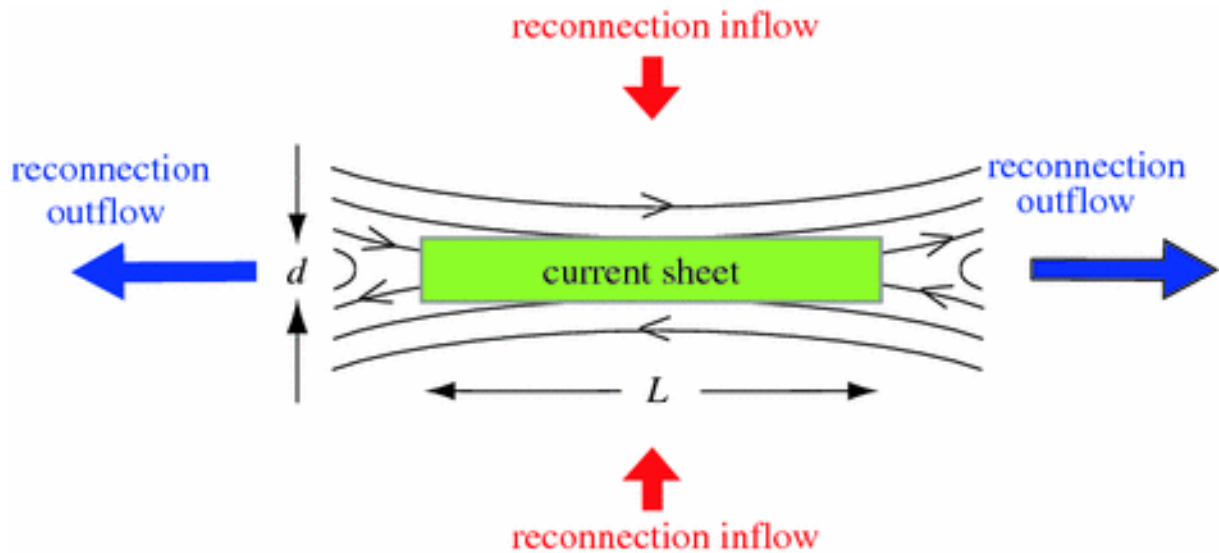
Figure 2.2: A diagram presenting the Sweet-Parker model for magnetic reconnection, taken from Wang (2016)

2.1.2   Magnetosphere

The magnetosphere is a dynamic and fluctuating environment. It is defined by how the Earth's magnetic field is embedded into the interplanetary medium and encapsulates countless plasma populations, current systems and controls our experiences of geomagnetic activity.

Figure 2.3 shows the main shape and features of the magnetosphere due to solar wind and IMF influences. The bow shock or bow wave is the first feature the solar wind encounters in the Sun-Earth system; it is where the supersonic solar wind is slowed to become subsonic and then continues to slow as it approaches the Earth's magnetosphere. The next boundary reached is the magnetopause, this region is the interface between the IMF and Earth's magnetosphere. If there are no processes which allow a coupling of the IMF with the magnetosphere and subsequent opening of magnetic field lines, almost all charged particles are prevented from reaching beyond the magnetopause. The solar wind pressure shapes the magnetosphere, compressing the sunward side while stretching the magnetopause beyond 60 Earth radii (*Shang et al.*, 2020) on the anti-sunward side.
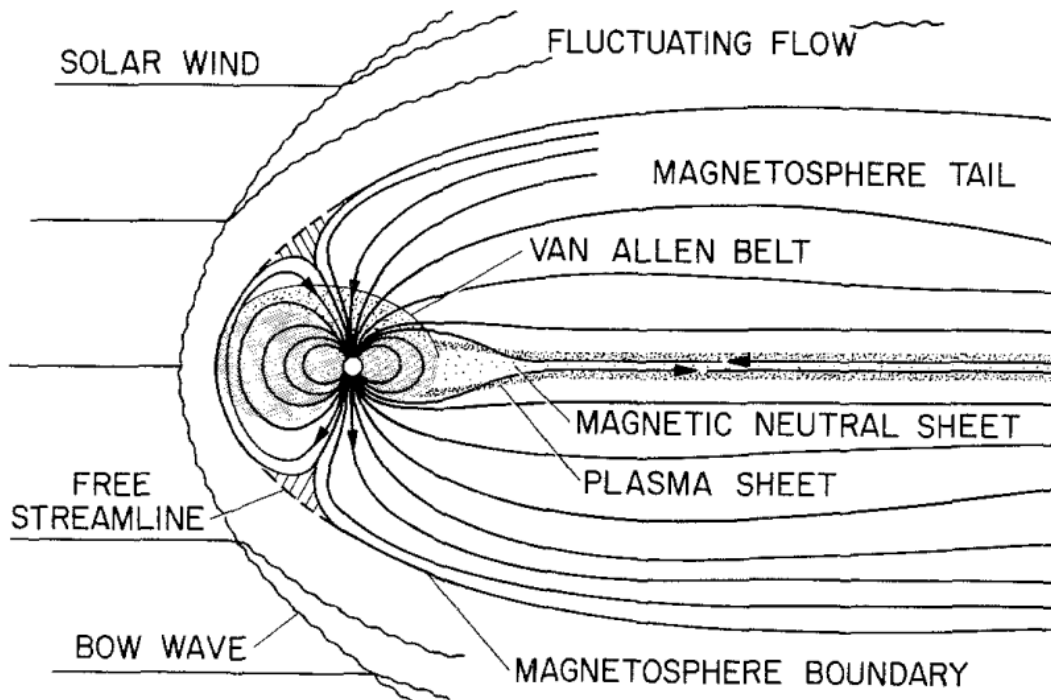
Figure 2.3: Diagram showing the main features of the Earth's magnetosphere taken from Wolfe and Intriligator (1970)

However, the IMF, solar wind and magnetosphere interaction isn't stable. Fluctuations in solar activity, the solar wind speed and composition, the solar streamer belt and the heliospheric current sheet mean that the IMF is contorted and twisted into incredibly different orientations. The changeable nature of the IMF orientation leads to variable magnetospheric dynamics. A northward orientated IMF typically has weaker effects. However, the draping of IMF field lines can cause an IMF magnetolobe interface whereby the magnetic field lines are in opposition. Opposing magnetic field lines with sufficient pressure on either side will reconnect, coupling the IMF to the geomagnetic field and injecting energy into the plasma local to the reconnection point and triggering various plasma processes. As can be expected, high reconnection rates on the day side magnetopause occur when the IMF has a southward orientation.

Figure 2.4 shows the Dungey cycle. The Dungey cycle describes how the IMF-magnetosphere system develops after dayside reconnection and how the reconnected magnetosphere magnetic field lines actively return to their initial configuration. IMF geomagnetic field coupling, for a southward orientated IMF, opens the closed, dayside field lines and then the solar wind pulls the field lines across the polar caps into the magnetotail (steps 1 through to 3 in figure 2.4). Opened field lines are later closed via reconnection in the tail. Tail reconnection can trigger a series of plasma processes that culminate in plasma sheet particles accelerating along magnetic field lines and bombarding the ionosphere (step 4 through to 6 in figure 2.4). This process and subsequent magnetospheric and ionospheric behaviours are referred to as substorms and are discussed further in section 2.2. Substorms are also associated with strong auroras, which occur when accelerated electrons excite atmospheric gases. The relaxation of these excited states leads to the energy being released in various wavelengths of electromag-

netic radiation.
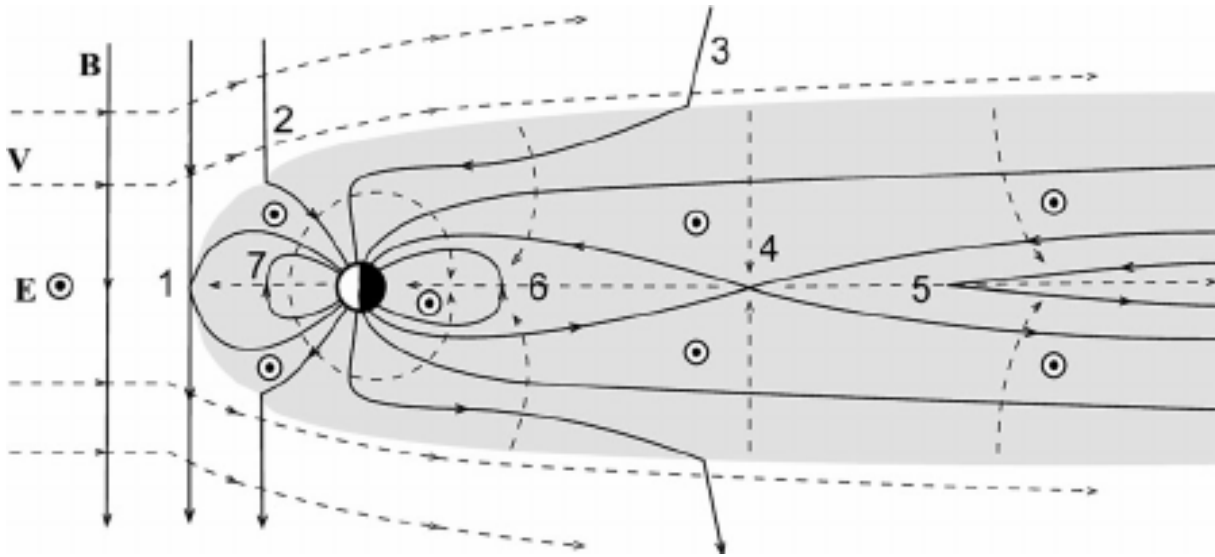
Figure 2.4: Diagram showing the day side opening of flux and the night side closing of flux (the Dungey Cycle) taken from Seki et al. (2015)

2.2   Polar Ionospheric Currents and Substorms

The polar ionosphere is very dynamic and has a wide range of influences whose origins can be traced back to the solar wind and IMF (*Milan et al.*, 2017). In this section the large scale characteristics of the polar ionosphere relevant to the research topic are discussed in terms of their origin and influences.

The ionosphere is a global atmospheric shell that has a measurable density of plasma. Figure 2.5 shows the general structure of the ionosphere and how it varies depending on the solar cycle and the time of day. As can be suspected from figure 2.5, ionospheric plasma density is heavily dependent on solar irradiance. This is due to the process of photo-ionisation where photons, primarily of a solar origin, impact neutrals, removing electrons and creating electron and ion pairs. The ionosphere owes its name to the population of ions and its plasma, whose density and behaviours can have large effects on a number of technologies. Ionospheric layers/regions arise due to the varied neutral atmospheric composition where constituents are ionised more efficiently by different wavelengths of light and due to the different penetration depths of wavelengths of light. At the lower layers, D and C, high energy radiation such as galactic cosmic rays are responsible for a larger portion of the photo-ionisation. In all regions of the ionosphere, the plasma density is constantly depleted by the process of recombination and transport of plasma. This is why the density drops so significantly from day to night, most significantly in the D and E region. In the polar ionosphere, changes in photo-ionisation seasonally cause a very significant variation in the plasma density vastly changing the dynamics and behaviours from Summer to Winter.
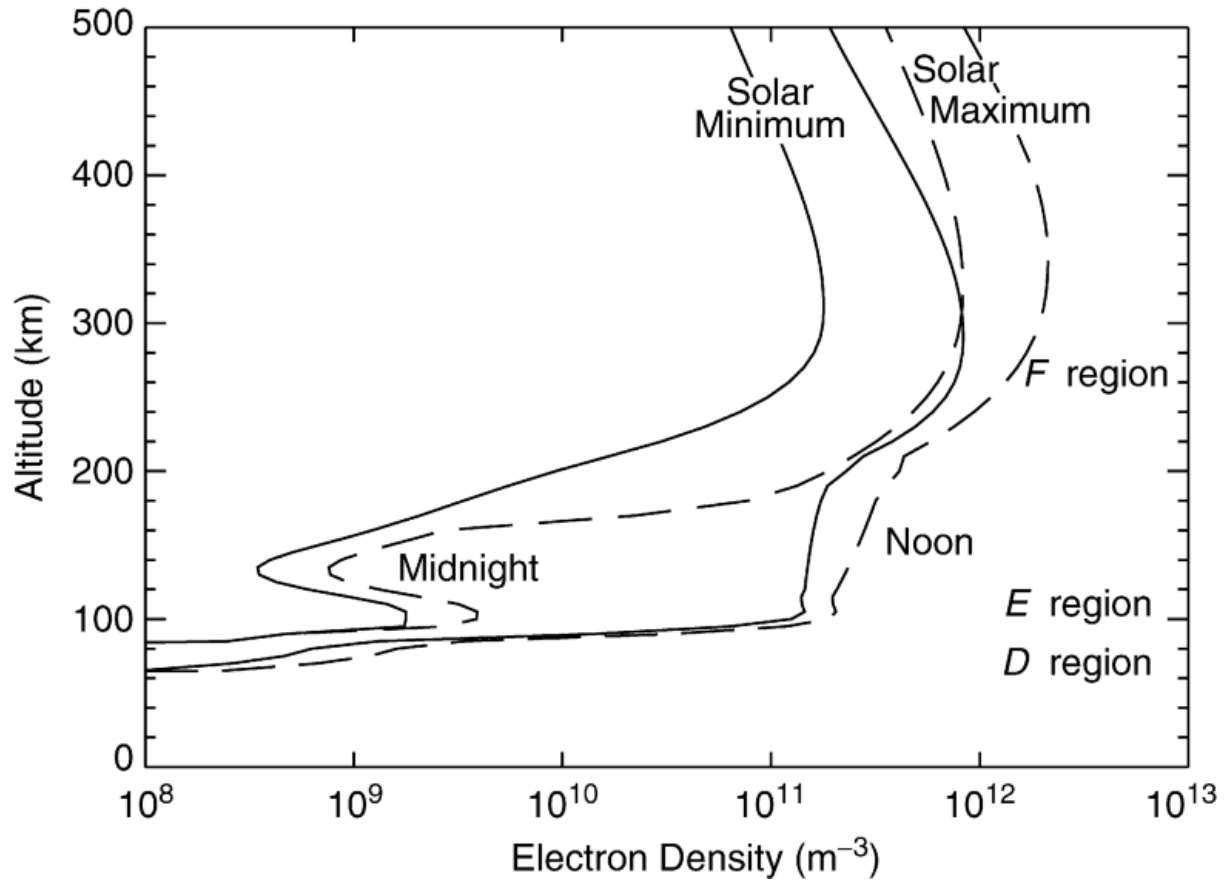
Figure 2.5: Electron density structure of the ionosphere at 18°N, 67°W during the September equinox for solar minium, maximum, noon and midnight, taken from Richmond (2007)

The Dungey cycle (figure 2.4), introduced in section 2.1, is an important framework to keep in mind when understanding the large scale plasma flows and current systems in the polar ionosphere. Opened field lines that are coupled with the IMF are pulled across the polar cap by the continuous stream of the frozen in solar wind. This in turn has an influence on the ionospheric plasma within the polar cap. Equation 2.1 shows that an anti-sunward bulk plasma velocity ($\mathbf{V}$) and a downward (upward) magnetic field ($\mathbf{B}$) in the northern (southern) hemisphere creates a perpendicular electric field ($\mathbf{E}$) from dawn to dusk across the polar cap (*Vasyliunas*, 2012; *Vasyliunas and Song*, 2005):

$$\mathbf{E} = -\mathbf{V} \times \mathbf{B}. \tag{2.1}$$

This equation is valid in the upper ionosphere and most of the magnetosphere, and implies that the magnetic field and plasma are frozen-in. Further down in the ionosphere however, the ion neutral collisions cause the ion velocity, in the direction of the flow of magnetic flux, to be diminished. This not only causes a bending of the magnetic field lines but also creates a sunward Hall current across the polar cap.

In steady state, the electric current and the electric field in the neutral frame of reference are related by the ionospheric Ohm's law. Integrated over the height of the ionosphere, this is

$$\mathbf{J} = \int \sigma \cdot \mathbf{E}' dh = \Sigma_P \mathbf{E}'_\perp + \Sigma_H \mathbf{B} \times \mathbf{E}'/B + \Sigma_\| \mathbf{E}'_\| \tag{2.2}$$

This equation describes the height integrated ionospheric current, $J(Am^{-1})$, in terms of two components. The Hall current, which can be seen directed sunward across the polar cap in figure 2.6, is defined as $\Sigma_H \frac{\mathbf{B} \times \mathbf{E}'}{B}$ in equation 2.2. Where Σ_H is the Hall conductance, $\mathbf{B}$ is the magnetic field and $\mathbf{E}'$ is the electric field in the frame of the rotating Earth, consequently the neutral wind is approximated to zero. Pedersen currents, which are shown in green in figure 2.6, are defined as $\Sigma_P \mathbf{E}'_\perp$. They flow across the polar cap from dawn to dusk connecting the region 1 field aligned currents. They also connect the region 1 and 2 currents on the dawn and dusk flanks. When conductance is uniform Pedersen currents can be considered curl-free as they alone close the field aligned currents, otherwise it is a combination of the Hall and Pedersen currents. This concludes the dynamics involved in steps 2 to 3 in figure 2.4. Steps 4 to 6 in figure 2.4 involve the closure of magnetic flux through magnetotail reconnection, the creation of a plasmoid in the solar wind and the dipolarisation of the tailward geomagnetic field lines.
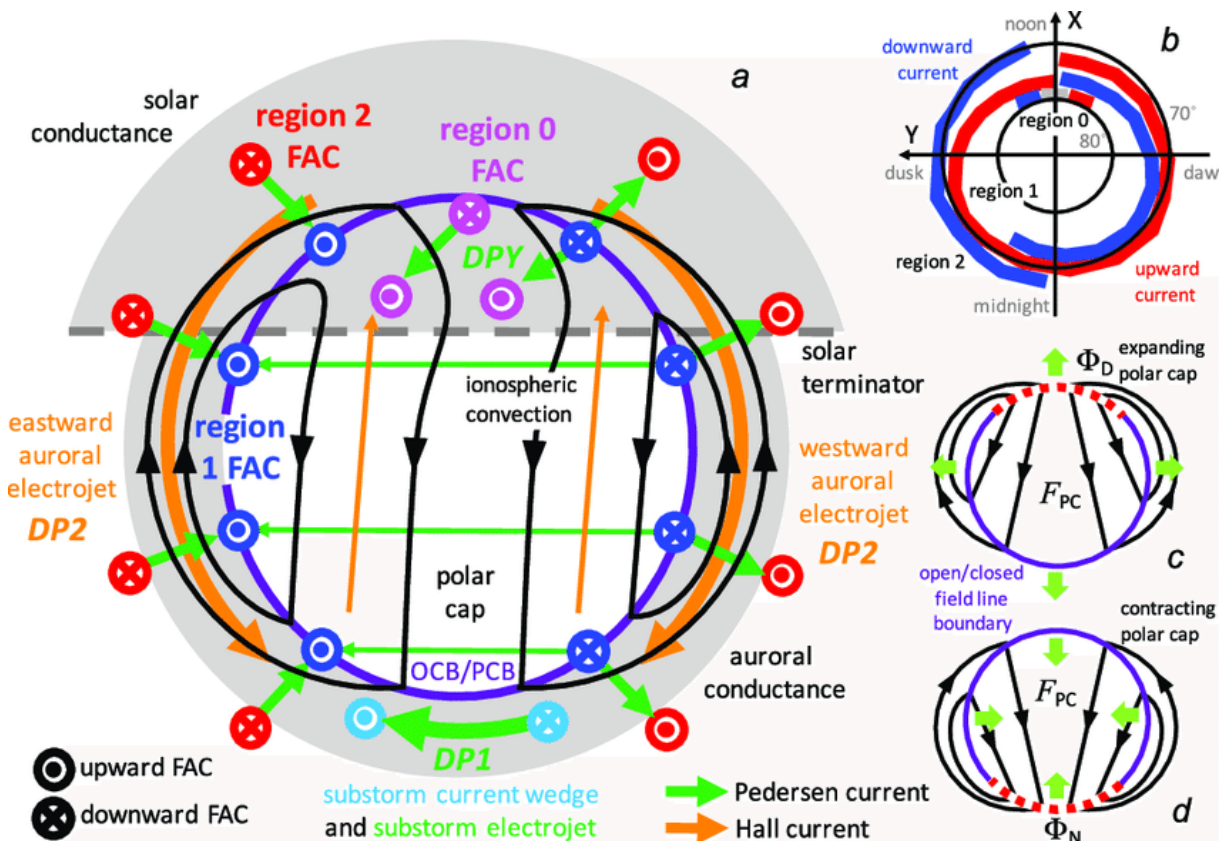
Figure 2.6: Diagram of ionospheric currents and convection, a pattern that occurs in both hemispheres. The top of the figure is noon and the bottom is midnight. Figure taken from Milan et al. (2017)

To replenish the closed magnetic flux on the day side and prevent an over abundance of magnetic flux in the night side geospace, the closed magnetic field lines convect sunward along the dawn and dusk flanks. This explains how to get from step 6 to 7 in figure 2.4. Similar to the polar cap convection there is a bulk plasma velocity and equation 2.1 will once again describe an electric field. However, this time the electric field will be orientated from dusk to dawn on the dawn and dusk flanks. Furthermore, equation 2.2 can be used again to explain the current systems seen on the dawn and dusk flanks in figure 2.6. A combination of the ion neutral collisions slowing the ion flow

and the still frozen in electrons cause an anti-sunward current. When the conductivity is uniform these divergence free currents, that circulate the flanks and through the polar cap, are considered to be the Hall currents.

Conductance Σ_H, Σ_P and $\Sigma_\parallel$, in equation 2.2, are the height-integrated Hall (σ_H), Pedersen (σ_P) and parallel ($\sigma_\parallel$) conductivity, respectively. These conductivities vary with altitude primarily due to changes in the effects of solar irradiance and particle precipitation. The altitude profile of the conductivities is shown in figure 2.7. The parallel conductivity ($\sigma_\parallel$) is large above 100 km, where this study is focused, as the charged particles there are highly mobile along the magnetic field lines. This makes the parallel electric field ($E_\parallel$) negligible. The Pedersen and Hall conductivity change according to the conditions within the ionosphere. The most variable ionospheric property is the ionospheric plasma density.

$$\sigma_P = \frac{N_e e}{B}\left(\frac{v_{in}\Omega_i}{v_{in}^2 + \Omega_i^2} + \frac{v_{en\perp}\Omega_e}{v_{en\perp}^2 + \Omega_e^2}\right) \tag{2.3}$$

$$\sigma_H = \frac{N_e e}{B}\left(\frac{\Omega_e^2}{v_{en\perp}^2 + \Omega_e^2} - \frac{\Omega_i^2}{v_{in}^2 + \Omega_i^2}\right) \tag{2.4}$$

Equation 2.3 and 2.4 show how the Pedersen and Hall conductivity depend on conditions within the ionosphere. Where: σ_P is the Pedersen conductivity, σ_H is the Hall conductivity, N_e is the electron density, e is electron charge, B is the magnitude of the magnetic field, v_{in} and v_{en} are the ion neutral and electron neutral collision frequency for momentum transform, respectively, and Ω_i and Ω_e are the ion and electron gyro frequency, respectively. The subscript $\perp$ is used to denote that it is the component perpendicular to the magnetic field, B. The electron density in the ionosphere increases due to photo-ionisation, which is higher during polar summer and during solar maximum. The inclusion of electron density in equation 2.3 and 2.4 shows that the Hall and Pedersen conductivity are seasonally variable in the polar ionosphere and solar cycle dependent. The seasonal dependence shows that on average polar ionospheric currents are strongest during the summer and when solar activity is high.

Solar irradiance is not the only factor that can drive changes in ionospheric conductivity. Energetic particles precipitating into the ionosphere, often shortened to particle precipitation, ionise neutrals and change the Hall and Pedersen conductance profiles.

$$\Sigma_P = \frac{40 e_c}{16 + e_c^2}\Phi_E^{\frac{1}{2}} \tag{2.5}$$

$$\frac{\Sigma_H}{\Sigma_P} = 0.45(e_c)^{0.85} \tag{2.6}$$

Equation 2.5 and 2.6 are known as the Robinson relations (*Robinson et al.*, 1987). Σ_P and Σ_H are the Pedersen and Hall conductance respectively, e_c is the average electron energy and Φ_E is the energy flux of the electrons. These relations show that an increase in the energy flux of electrons due to particle precipitation will increase the Pedersen and Hall conductance and the Hall/Pedersen conductance ratio.
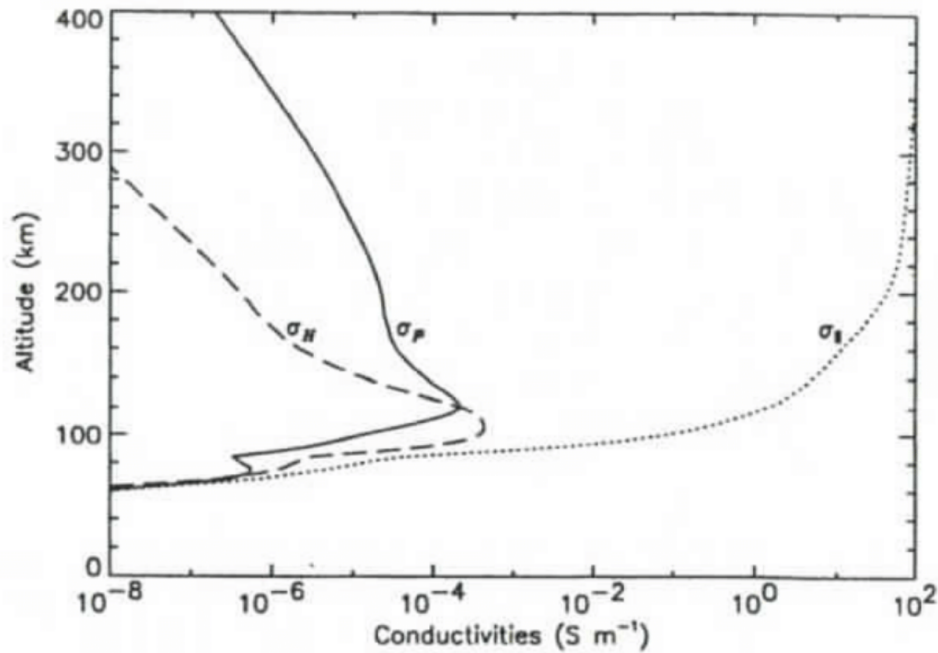
Figure 2.7: Height profile of Pedersen, Hall and parallel ionospheric conductivities at $44.6°N$, $2.2°E$ *during solar minimum on the 21st of March, taken from Richmond (1995)*

2.2.1 Substorms

The concept of substorms has been around since the discussion of space weather and geomagnetic activity began. Primarily, substorms refer to a clear signature in magnetic field measurements that distinguishes itself clearly from small scale background variations. This section introduces the origin, stages and current theories on this topic, that are relevant to this study.

Magnetotail reconnection is an important feature of polar ionosphere dynamics, it is the driver of substorm phenomena. Magnetotail reconnection can inject the plasma sheet with energy accelerating the plasma along magnetic field lines and bombarding the upper ionosphere. This consequently excites the neutrals and leads to a release of the energy as electromagnetic radiation in the form of auroral displays. Substorms typically last between one and three hours and go through three distinct phases. These phases are growth, expansion (starting with a so-called substorm onset), and recovery. The evolution of substorms in terms of phases was first introduced by *Akasofu* (1964) and furthered by *McPherron* (1970) with the introduction of the growth phase. Historically, substorms were identified through ground based measurements and as such the substorm phases are typically classified by how they register in magnetometer and auroral observatory data. When looking at substorms the H component of auroral zone magnetometers is of most importance. This component is a measure of the magnetic field fluctuations in the local magnetic north direction. Perturbations in this component correspond to an east-west equivalent ionospheric current, or electrojet. As such the amplitude of a perturbation gives information on the strength of the electrojet. During the growth phase, signatures in the H component are minimal. However, for a number of substorms it is common to see a small rise. During the expansion and leading into

the onset, there is steep rapid decline in the H component signifying an increase in the electrojet strength eventually reaching the lowest value in the H component for the substorm. Finally, the recovery phase represents a magnetospheric relaxation. A slowly decaying H component shows that the electrojets are weakening. The recovery phase is the longest lived and as such is often interrupted by a new substorm.

2.2.2 Harang Discontinuity

In 1946 Leiv Harang began investigating the behaviours in between the eastward and westward electrojets using ground based magnetometer stations. He found a reversal in the direction of the auroral electrojet within a small region (*Harang*, 1946; *Koskinen and Pulkkinen*, 1995). More recent studies have chosen to call this region the Harang discontinuity (HD) and have subsequently found that the location and signature strength is dependent on the polarity and magnitude of the IMF components B_y and B_z (*Kissinger et al.*, 2013; *Koskinen and Pulkkinen*, 1995).
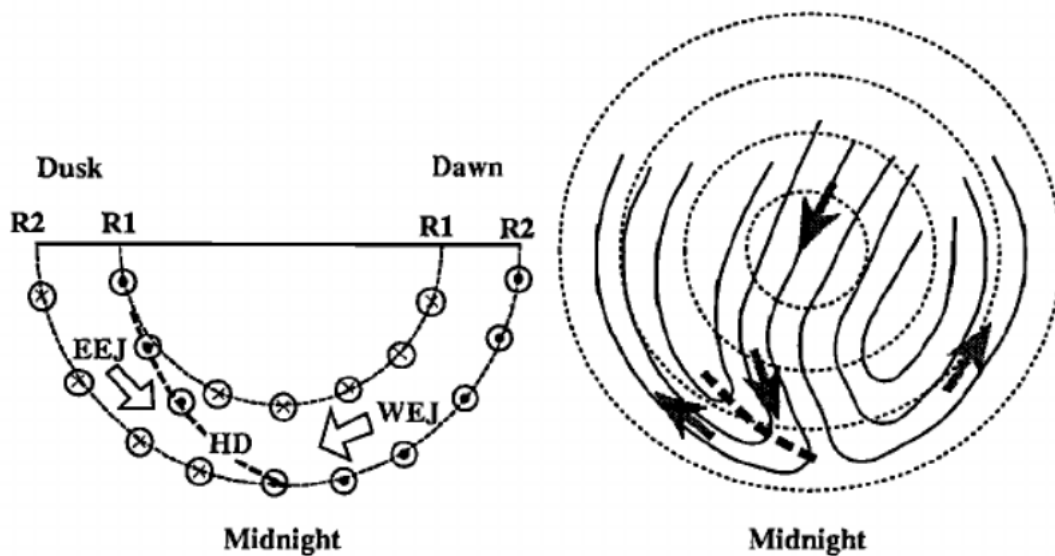
Figure 2.8: Figure showing the Harang Discontinuity in terms of the electrojets and region 1 (R1) and region 2 (R2) field aligned currents in the left diagram. And in terms of the ionospheric convection in the right diagram. The figure is taken from Koskinen and Pulkkinen (1995)

Figure 2.8 shows the HD in terms of the electrojets and field aligned currents (left diagram) and ionospheric convection (right diagram). As the diagram shows, the HD follows upward field aligned currents from the region 1 and region 2 current systems across the electrojet from a pre midnight magnetic local time (MLT) through to midnight. Substorm onsets typically occur within this region due to the connection of its field lines into the inner edge of the plasma sheet, at approximately 10 Earth Radii (*Angelopoulos et al.*, 2008; *Liou*, 2010). This region has a strong, but as yet not fully understood, connection to the magnetotail reconnection point and is known for plasma processes that accelerate plasma along the magnetic field lines into the polar ionosphere (*Angelopoulos et al.*, 2008).

2.2.3   Fukushima's Theorem

An important part of this study is decomposing the currents seen in the ionosphere into constituents that can be measured by ground magnetometers. This section introduces the decomposition that this study uses and discusses its implication on the signatures of the decomposed current vector field.

Using Helmholtz decomposition (*Helmholtz*, 1858) any vector field can be decomposed into two components, a divergence free and a curl free component. In the context of the ionosphere, this is can be done for height integrated currents,

$$\mathbf{J}_\perp = \mathbf{J}_{df} + \mathbf{J}_{cf}, \tag{2.7}$$

where $\mathbf{J}_\perp$ is the height integrated current and $\mathbf{J}_{df}$ and $\mathbf{J}_{cf}$ are the divergence free and curl free components of the height integrated current, respectively. The more common description of the height integrated currents is as a combination of Hall and Pedersen currents.

$$\mathbf{J}_\perp = \mathbf{J}_H + \mathbf{J}_P \tag{2.8}$$

Where $\mathbf{J}_H$ and $\mathbf{J}_P$ are the Hall and Pedersen currents respectively.

Understanding the physicality of the divergence-free and curl-free currents is important when attempting to model them and draw conclusions from their behaviours. *Laundal et al.* (2015) discussed and evaluated the conditions under which the Hall current ($\mathbf{J}_H$) is equal to the divergence-free current ($\mathbf{J}_{df}$) and the Pedersen current ($\mathbf{J}_P$) is equal to the curl-free current ($\mathbf{J}_{cf}$). *Laundal et al.* (2015) states that when the gradients of the Hall and Pedersen conductances in the direction parallel to ionospheric convection are zero, the Hall current can be equated to the divergence-free current and the Pedersen current can be equated to the curl-free current.

The seasonal extremes within the polar regions, as discussed in section 2.2, lead to varying conductance conditions. During the summer the conductance is high and approximately uniform whereas during the winter the conductance is low and easily changed due to particle precipitation events. Therefore, during the summer the Hall and Pedersen currents can, approximately, on average be described by divergence and curl-free currents respectively. However, during the winter the assumption of no gradient in the conductances is not accurate and therefore the relationship of Hall and Pedersen currents with divergence and curl-free currents is not as simple.

Fukishima's theorem shows that curl-free currents within the ionosphere show no ground magnetic field perturbations and explains why before satellites with magnetometers were used to investigate ionospheric currents there were two theories on ionospheric currents and neither could be disregarded.
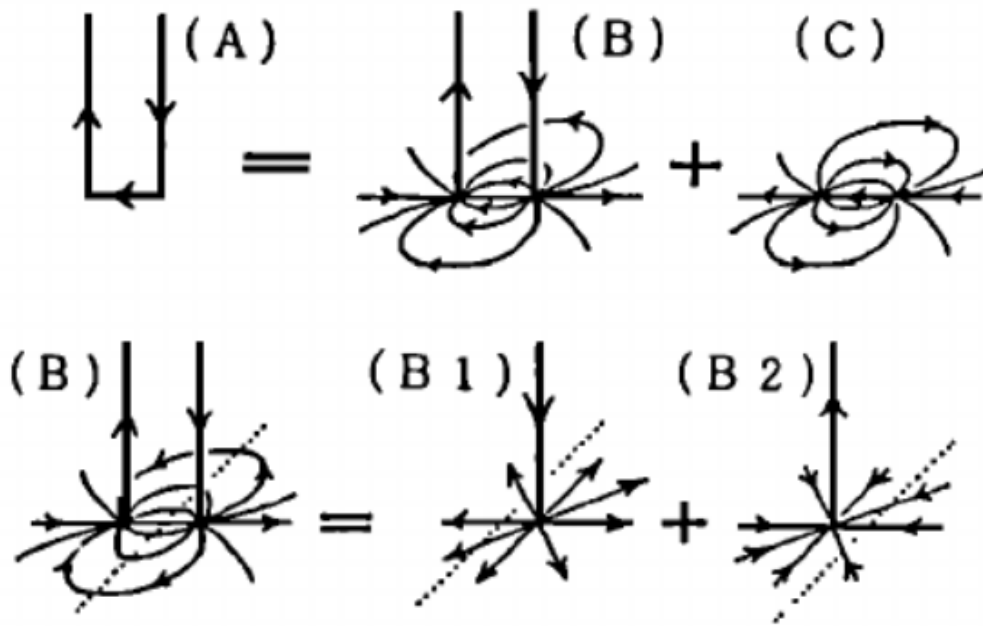
Figure 2.9: "Diagrams showing the equivalence in ground magnetic effect of current systems A and C, because there is no magnetic field produced below the ionosphere by current system $A - C = B = B1 + B2$" taken from Fukushima (1994)

Figure 2.9 is taken from *Fukushima* (1994) and illustrates how the theories by Birkeland, A, and Chapman, C, have the same ground magnetic effect. The current B is the difference between current systems A and C and can be separated into two components B1 and B2. It is simple to see that in the B1 and B2 systems the magnetic field below the systems, as a sum of the in (out) flowing current and the radial currents that are directed away from (towards) the source (sink) of the current system, is zero. As such the magnetic effect on the ground from B is zero and, consequently, the magnetic field under the current systems from A and C are the same and neither theory can be disproved using ground magnetometers. With the use of satellites with on board magnetometers, it has been long confirmed that Birkeland's interpretation of the ionospheric currents is correct and Chapman's theory has been disproved.

This study makes use of only ground magnetometers to study the ionospheric currents. It is therefore important to understand the implications of Fukushima's theorem on the current systems that are being measured. The use of ground magnetometers limits this study to the investigation of divergence-free currents. Although curl-free currents cannot be investigated, the electrojets are divergence-free and this study is able to perform an in depth analysis on their properties using ground magnetometers.

2.3 Telluric Currents

Telluric currents are natural or induced currents within the Earth. Even as early as the rise of telegraph systems, their impacts on technology have been significant and notable. This section introduces their origin and the problems that arise from their effects in terms of both scientific investigation relevant to this study and in a more general sense that influences society.

There are a large number of causes of telluric currents with a variety of cyclic dependencies (*Helman*, 2013). This study focuses on the high latitude regions of the Earth in which Geomagnetically Induced Currents (GICs) are strongest. From a technological perspective this induction is highly problematic. Not only can intense ionospheric currents, associated with strong geomagnetic substorms, induce currents in the Earth but also in conducting man made structures such as pipes, electrical wires and telephone wires. This is problematic because it can cause corrosion of pipes, leading to leaks, and high voltages in wires that are in excess of what the systems can handle, creating temporary and permanent outages in the operations of the grids (*Taltavall*, 1915). In terms of this project the telluric currents and GICs are problematic due to their associated magnetic field. The magnetic field created by these currents changes the magnetic field measured by ground level magnetometers and, when using the modelling method discussed in section 3.1, it can lead to the incorrect assumption that the magnetic disturbances measured are only caused by ionospheric currents. Therefore, the modelled currents will not describe the true ionospheric currents (*Pulkkinen et al.*, 2003a). The significance of this effect can be very high, such that *Tanskanen et al.* (2001) reported that during intense substorm events up to 40% of the auroral lower index has been due to ground induced currents. Methodology designed to account for the effects of telluric currents on the modelling of ionospheric currents is discussed in section 3.6.

2.4 Explicit B_y Effect

The explicit B_y effect is a phenomenon of intense ongoing research where the goal is to understand and outline the effects on geospace associated with the polarity of the IMF B_y component, which appear to be different around the two solstices. The following section will discuss the current knowledge and theories within this research area.

When discussing the impact of IMF conditions on the Earth's magnetosphere, the B_z (north-south) component is considered most significant as it is the factor that dictates where and at what rate day side reconnection can take place. The Newell coupling function, equation 2.9, is commonly used in an attempt to quantify the day side reconnection rate and the driving conditions on the magnetosphere. It is defined as

$$\frac{d\phi_{MP}}{dt} = v^{\frac{4}{3}} B_T^{\frac{2}{3}} \sin^{\frac{8}{3}}\left(\frac{\theta}{2}\right),$$ (2.9)

where v is the solar wind velocity, $B_T = \sqrt{B_z^2 + B_y^2}$ is the transverse component of the IMF, and θ is the IMF clock angle and is equal to $arctan2(B_y, B_z)$. As can be seen, consideration of the B_y component is required for a greater understanding of the magnetospheric and ionospheric response. IMF B_y influence on reconnection and solar wind - magnetosphere coupling has always been considered to be equal in terms of polarity which is apparent in its treatment in the Newell coupling function (equation 2.9). However, since 1975 there have been observations, through the ionospheric response to IMF B_y, challenging this common assumption (*Friis-Christensen and Wilhjelm*, 1975; *Vennerstrøm and Friis-Christensen*, 1987). The polarity of the IMF B_y component can have a significant effect at times around the solstices. *Reistad et al.* (2020) investigated the effect of the polarity of B_y on the size of the polar cap. During a negative dipole

tilt positive B_y was found to lead to a larger polar cap in both hemispheres and during a positive dipole tilt negative B_y was found to increase the size of the polar cap. Changes within the size of the polar cap can be related to the day side reconnection rate, the more flux that is opened on the day side the larger the polar cap will become. However, polar cap size is also affected by magnetotail processes. More rapid closing of magnetic field lines in the tail will lead to a smaller polar cap.

A study that is currently under review, by *Ohma et al.* (2020), used five independent substorm lists to show how the explicit B_y effect on the occurrence of substorms. They found that for a positive dipole tilt, the typical condition in northern hemisphere summer, a negative B_y causes a higher frequency of substorms. And for a negative dipole tilt, the typical condition in northern hemisphere winter, a positive B_y causes a higher frequency of substorms. Substorms are a process driven by magnetotail dynamics and these results suggest that there is not only a difference in the IMF-magnetosphere coupling on the day side due to the polarity of B_y, but there is also a possibility that there is an explicit B_y effect in the magnetotail response. *Holappa and Mursula* (2018) and *Holappa et al.* (2020b) have also seen an explicit B_y effect in geomagnetic activity. *Holappa and Mursula* (2018) investigated the explicit B_y effect on the eastward and westward electrojets in the northern hemisphere using the auroral upper (AU) and auroral lower (AL) indices, respectively. They found a suppression of the westward electrojet in the winter when B_y is positive and when B_y is negative during the summer. They found no clear explicit B_y effects on the eastward electrojet. *Holappa and Mursula* (2018) used the K index to investigate geomagnetic activity in the southern hemisphere and found that during southern hemisphere winter the K index is suppressed when B_y is positive, however no clear trends were found during the summer. (*Holappa et al.*, 2020b) took a different approach to investigate the explicit B_y effect on geomagnetic activity. Analysing the change in the flux of precipitating electrons in both hemispheres allowed *Holappa et al.* (2020b) to investigate the explicit B_y effect in a different way. Between 20 and 4 MLT the precipitation of electrons is higher for B_y positive in both hemispheres in northern hemisphere winter and for B_y negative in both hemispheres during southern hemisphere winter. Particle precipitation increases the conductance of the ionosphere, therefore a reduction in precipitation can be a possible explanation for the suppression of the westward electrojet and the correlation of the explicit B_y effect in both. All the research up to now cannot conclusively show if it is the effect of B_y polarity on dayside IMF-magnetosphere coupling or on magnetotail structure, dynamics and plasma processes or a combination of both that create the explicit B_y effect observed in the polar ionosphere.

Chapter 3

Method

This chapter begins by describing spherical elementary currents (SECS) and progresses to outline the common way SECS models are created and optimised. Using this as a starting point, this chapter builds upon this method and shows how to implement a new inversion technique that improves the physicality of the divergence-free currents that are modelled. The chapter presents, in detail, the steps taken to find the best methodology for creating a spherical elementary current model that can find the divergence-free currents within the northern polar ionosphere using ground based magnetometer measurements. The chapter goes on to describe an algorithm that can find the electrojet properties that are presented and discuss in the chapter 4 and 5.

3.1   Spherical Elementary Current Systems (SECS)

Spherical elementary current systems (SECS) is a key concept for this study and is the foundation for which the work has been built on. This methodology section will discuss what is already known on the topic and the physics that it is derived from.

Using a system of spherical elementary currents with applications in the ionosphere, is a concept that was first introduced by *Amm* (1997). The concept uses Helmholtz decomposition in order to separate the height integrated currents into divergence ($\mathbf{J}_{df}$) and curl-free ($\mathbf{J}_{cf}$) components as shown in equation 3.1, where $\mathbf{J}$ is the ionospheric current density (*Laundal et al.*, 2015; *Untiedt and Baumjohann*, 1993):

$$\mathbf{J}_{\perp} = \mathbf{J}_{df} + \mathbf{J}_{cf}. \tag{3.1}$$

By separating the current in this manner, the divergence-free and curl-free currents can be modelled separately and then the combination of them will produce the entire current system. Curl-free currents can be imagined as the superposition of curl-free elementary systems. The pole of each system relates to the a source and sink of the curl-free currents and as such the amplitude of each system is scaled by the field aligned currents into the ionosphere. A second set of spherical elementary current systems can be created to model the divergence-free currents.
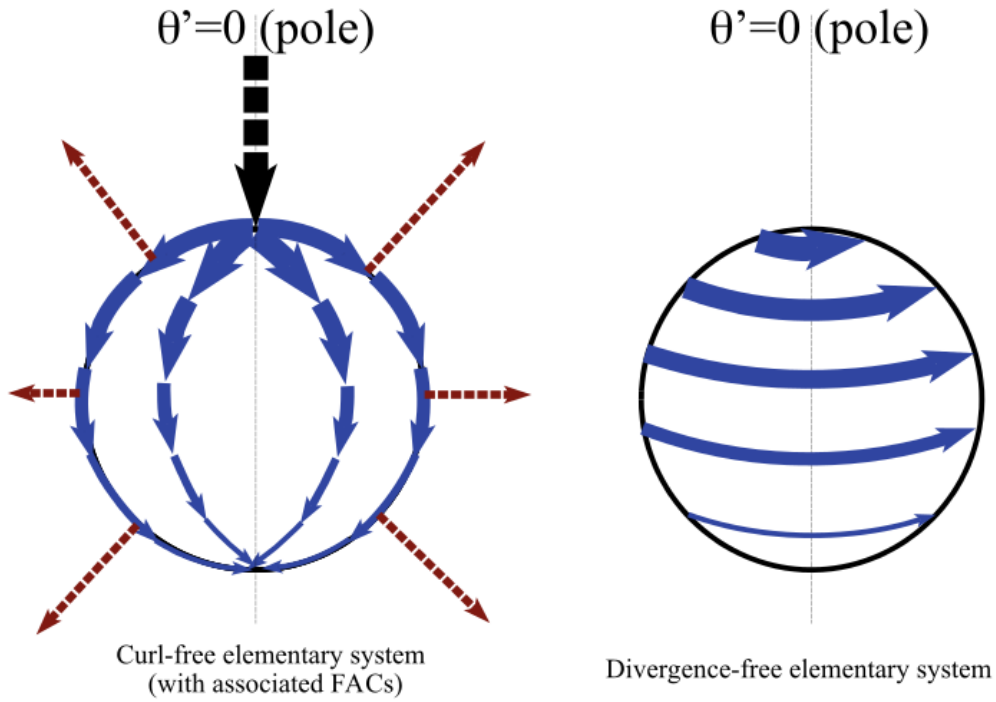
Figure 3.1: Representation of curl-free (left) and divergence-free (right) Spherical Elementary Current Systems from Vanhamäki and Juusola (2020). A superposition of curl (divergence) free systems can be used to to represent any curl (divergence) free vector field.

The next stage is to be able to describe the current at any point within these elementary systems. Equations 3.2 and 3.3, derived by *Amm* (1997), describe the currents in both systems which are in the south ($\hat{\mathbf{e}}_{\theta'}$) and east ($\hat{\mathbf{e}}_{\phi'}$) direction respectively.

$$\mathbf{J}_{cf}(\mathbf{r}') = \frac{I_{0,cf}}{4\pi R_I} cot(\frac{\theta'}{2})\hat{\mathbf{e}}_{\theta'} \qquad (3.2)$$

$$\mathbf{J}_{df}(\mathbf{r}') = \frac{I_{0,df}}{4\pi R_I} cot(\frac{\theta'}{2})\hat{\mathbf{e}}_{\phi'} \qquad (3.3)$$

Where R_I is the radius of the ionospheric layer, θ' is the colatitude of the evaluation point in terms of the SECS system, $\mathbf{r}'$ is the radial location of the evaluation point in terms of the SECS system and I_0 is a scalar that is unique to each system and can be used to describe the relative amplitudes of spherical elementary systems and subsequently compare the currents produced by the systems.

Measurements of magnetic field perturbations are needed to begin describing real currents in these SEC systems. The correct scalar (I_0) for the pole is needed in order to find the currents that relate to the magnetic field perturbations measured. *Amm and Viljanen* (1999), *Vanhamäki and Juusola* (2020) and *Juusola et al.* (2006) have derived analytical expressions of the magnetic field emanating from a singular SEC system. By superposing the magnetic field from each system at the location of measurements, a balance of SEC system amplitudes can be found that closely resemble the measurements. And, subsequently, demonstrate a current system that would result in these magnetic perturbations. Equations 3.4, 3.5 and 3.6, where r_m is the radial position of the evaluated point and R_I is the radial position of the ionospheric layer, show how the radial

and theta magnetic field components of a divergence-free spherical elementary system and the full vector of the magnetic field of a curl-free spherical elementary system can be calculated.

$$\mathbf{B}_r^{DF}(r,\theta',\phi') = \frac{\mu_0 I_{0,df}}{4\pi r_m} \begin{cases} \frac{1}{\sqrt{1+(\frac{r_m}{R_I})^2 - 2(\frac{r_m}{R_I})cos(\theta')}} - 1, & r_m < R_I \\[3mm] \frac{\frac{R_I}{r_m}}{\sqrt{1+(\frac{R_I}{r_m})^2 - 2(\frac{R_I}{r_m})cos(\theta')}} - \frac{R_I}{r_m}, & r_m > R_I \end{cases} \tag{3.4}$$

$$\mathbf{B}_\theta^{DF}(r,\theta',\phi') = \frac{-\mu_0 I_{0,df}}{4\pi r_m sin(\theta')} \begin{cases} \frac{\frac{r_m}{R_I}-cos(\theta')}{\sqrt{1+(\frac{r_m}{R_I})^2 - 2(\frac{r_m}{R_I})cos(\theta')}} + cos(\theta'), & r_m < R_I \\[3mm] \frac{1-\frac{R_I}{r_m}cos(\theta')}{\sqrt{1+(\frac{R_I}{r_m})^2 - 2(\frac{R_I}{r_m})cos(\theta')}} - 1, & r_m > R_I \end{cases} \tag{3.5}$$

$$\mathbf{B}^{CF}(r,\theta',\phi') = \frac{-\mu_0 I_{0,cf}}{4\pi r_m} \begin{cases} 0, & r_m < R_I \\ cot(\frac{\theta'}{2})\hat{\mathbf{e}}_{\phi'} & r_m > R_I \end{cases} \tag{3.6}$$

Due to the nature of the spherical elementary currents, the magnetic perturbations from a divergence-free system have vectors in the radial and theta directions, in the SEC system, and a curl-free system has magnetic field perturbations in the phi direction, also in the SEC system.

3.1.1   Conversion to global co-ordinates

In order to superpose SEC systems to retrieve the system amplitudes and replicate real current systems, vector components and coordinates in each SEC system need to be translated from the SEC co-ordinate system to a global co-ordinate system, such as the Geodetic co-ordinate system. Equations 3.7, 3.10 and 3.11, derived by *Vanhamäki et al.* (2003), and figure 3.2 show how vectors and positions can be converted to and from the spherical elementary co-ordinate system. The superscript *el* is used for the global co-ordinates of the SEC pole, the subscript *k* is used for the global co-ordinates of the evaluated point, θ' is the colatitude of the evaluated point in terms of the SEC system co-ordinates and *C* can be found from equations 3.8 and 3.9. Vectors $\hat{\mathbf{e}}_\theta$ and $\hat{\mathbf{e}}_\phi$ in equations 3.10 and 3.11 are in directions east and south, respectively. The vectors with primes are defined in reference to the SEC pole while those without are in terms of the global co-ordinate system.

$$cos(\theta') = cos(\theta_k)cos(\theta^{el}) + sin(\theta_k)sin(\theta^{el})cos(\phi^{el} - \phi_k) \tag{3.7}$$

$$cos(C) = \frac{cos(\theta^{el}) - cos(\theta)cos(\theta')}{sin(\theta)sin(\theta')} \tag{3.8}$$

$$sin(C) = \frac{sin(\theta^{el})sin(\phi^{el} - \phi)}{sin(\theta')} \tag{3.9}$$

$$\hat{\mathbf{e}}_{\theta'} = \hat{\mathbf{e}}_\theta cos(C) - \hat{\mathbf{e}}_\phi sin(C) \tag{3.10}$$

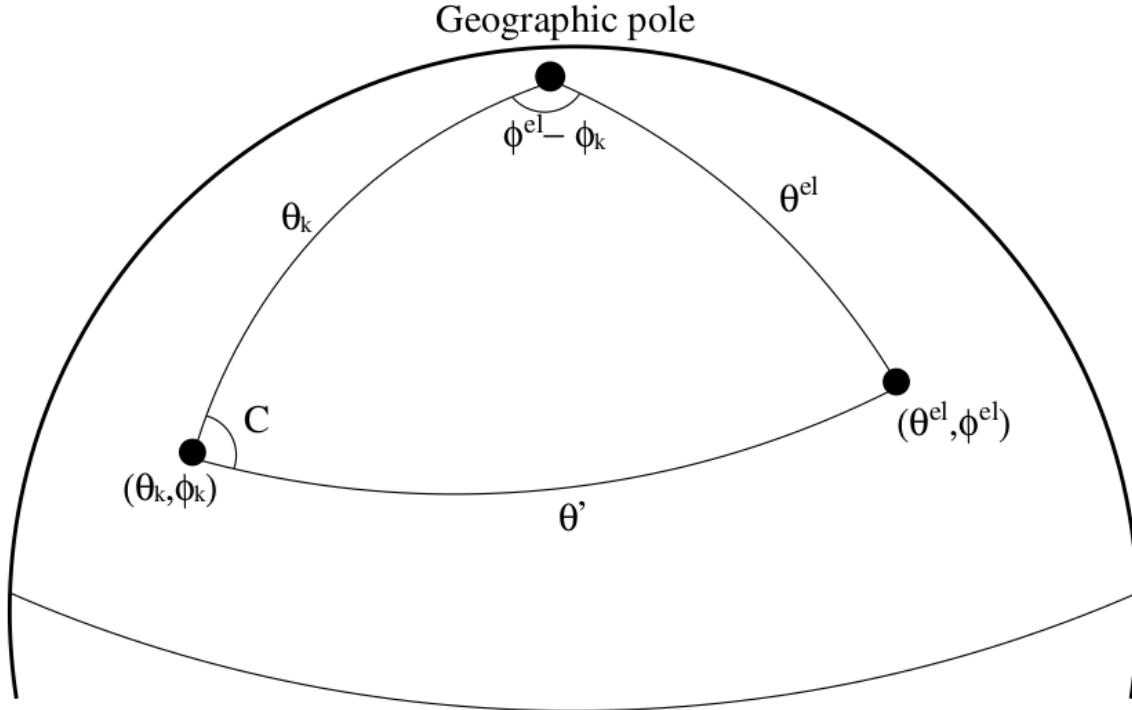$$\hat{\mathbf{e}}_{\phi'} = \hat{\mathbf{e}}_\theta sin(C) + \hat{\mathbf{e}}_\phi cos(C) \tag{3.11}$$

Figure 3.2: SEC co-ordinate transformation to and from global co-ordinates from Vanhamäki and Juusola (2020), where θ^{el} and ϕ^{el} are the global co-ordinates of the SEC pole, θ_k and ϕ_k are the global co-ordinates of the evaluated point and θ' is the colatitude of the evaluated point in terms of the SEC system co-ordinates.

3.1.2 Singularities

One problem with the SECS model, as described by *Vanhamäki and Juusola* (2020), is singularities. Figure 3.3 shows that for small values of θ' the evaluated sheet current density becomes infinite. This means that, without adjustments, sheet current densities evaluated close to a SEC pole cannot be trusted due to their unrealistic magnitudes.

Vanhamäki and Juusola (2020) outlined a modification, equations 3.12 and 3.13, that changes the behaviours of the evaluated currents close to SEC poles:

$$\mathbf{J}_{cf}(\mathbf{r}') = \frac{I_{0,cf}}{4\pi R_I}\hat{\mathbf{e}}_{\theta'} \begin{cases} \cot^2(\frac{\theta_0}{2})\tan(\frac{\theta'}{2}) & \theta' < \theta_0 \\ \cot(\frac{\theta'}{2}) & \theta' \geq \theta_0 \end{cases} \tag{3.12}$$

$$\mathbf{J}_{df}(\mathbf{r}') = \frac{I_{0,df}}{4\pi R_I}\hat{\mathbf{e}}_{\phi'} \begin{cases} \cot^2(\frac{\theta_0}{2})\tan(\frac{\theta'}{2}) & \theta' < \theta_0 \\ \cot(\frac{\theta'}{2}) & \theta' \geq \theta_0 \end{cases} \tag{3.13}$$

In equations 3.12 and 3.13 θ_0 is a variable to be chosen as the colatitude limit for the modifications to begin. This isn't a fixed value for all set ups as it depends on the spacing between SEC poles so a consistent SEC pole grid is needed. Figure 3.4 shows how the modifications in equation 3.13 change the solution close to the SEC pole and return more sensible magnitudes of currents.

Divergence Free Sheet Current Density for a range of θ'

Figure 3.3: A graph showing how $\cot(\frac{\theta'}{2})$ in equation 3.3 affects the solution for divergence-free currents close to the SEC poles (small values of θ')

In this study the singularity limit chosen is related to a spacing of less than 50 km between the pole and the evaluation point. This is equivalent to a limit of approximately $0.44°$.

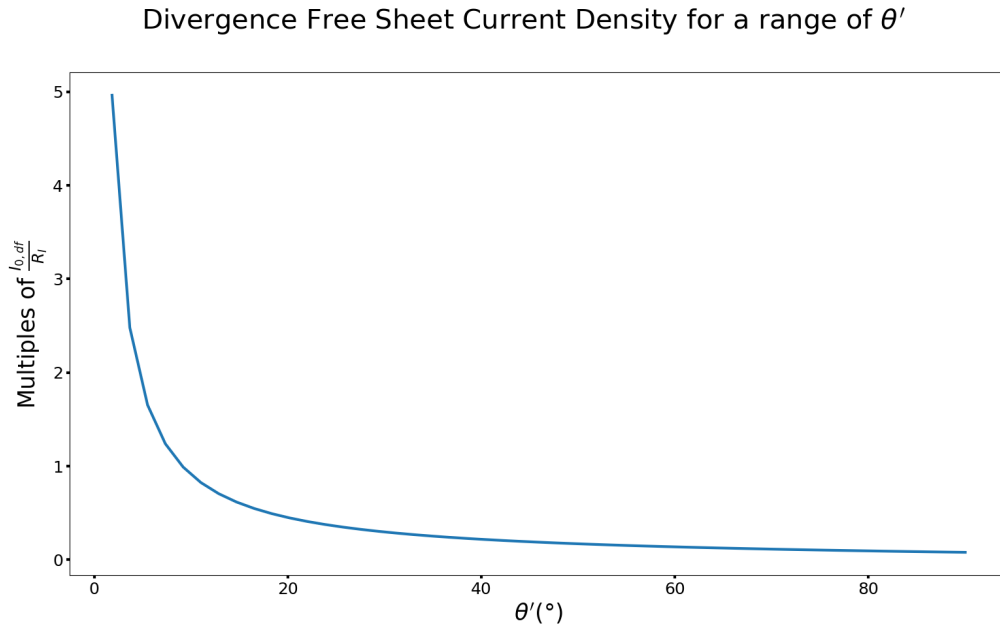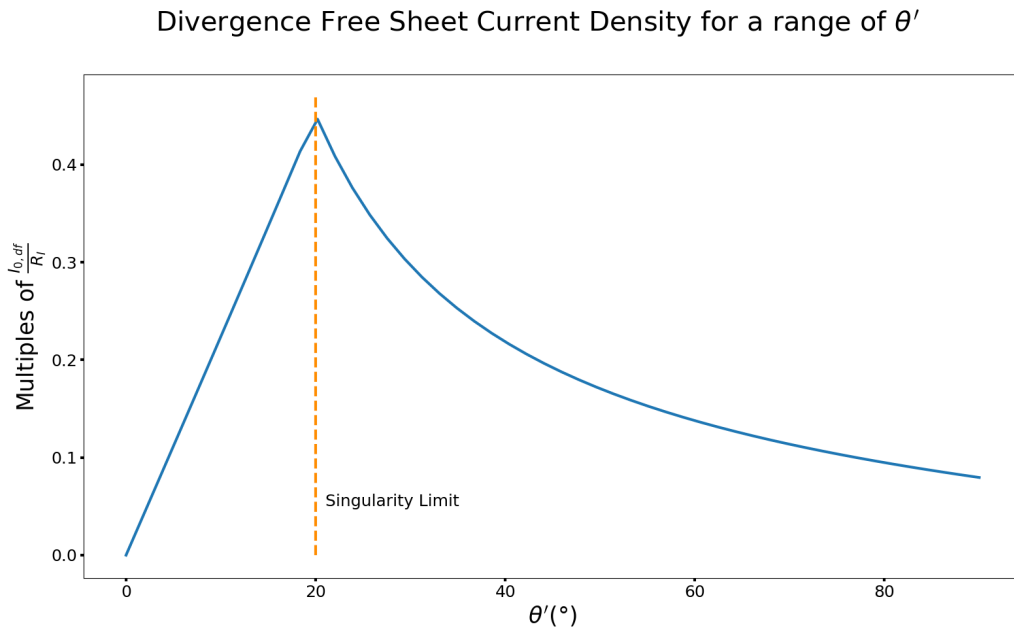Divergence Free Sheet Current Density for a range of θ'

Figure 3.4: A graph showing how the modifications in equation 3.13 affect the solution for divergence-free currents close to the SEC poles (small values of θ') using a singularity limit of 20°

3.2   Cubed Sphere

The choice of grid is an important factor when attempting to make a SECS model. Firstly, if a SEC pole is too close to a magnetometer, in relation to the SEC pole spacing, then the SEC pole amplitude becomes very small. This can be predicted from equations 3.5 and 3.4, where a small colatitude θ' causes incredibly large magnetic perturbations for a given amplitude I_0. Conversely, the SEC pole amplitude would need to be incredibly small to replicate realistic measurements of the magnetic field. Surrounding SEC poles would then compensate and have increased amplitudes so the model still replicates other measurements accurately. All this brings disorder and rapid fluctuations to the SEC pole amplitudes making it less likely to represent the ionospheric currents.

A regular grid in a geographic co-ordinate system would cause an increasing density of SEC poles for higher latitudes. The cubed sphere concept, created by *Ronchi et al.* (1996), is used in this study to create a regular grid of SEC poles without this issue. The idea to use this method for creating a SEC pole grid came from *Laundal et al.* (2020). The concept is to place a sphere inside a cube and project co-ordinates from the spherical surface onto the corresponding cube face. The cube is typically defined to have the centre of one face to be aligned with the pole of the spherical surface, however for this application, due to its regional nature, one face is centred on the the chosen grid centre instead. This is not the only projection from a spherical system that could be used to define a regular grid of SEC poles however, there are some key advantages to using the cubed sphere. The SEC pole grid is created in the cubed sphere projection, with a regular spacing that equates to a spacing of 50*km*, which allows the gradients in the SEC pole amplitudes across the cube face to be calculated with ease. While remaining in a spherical system this is difficult due to the curvature of the Earth. *Ronchi et al.* (1996) provides the equations to not only translate points to and from the cubed sphere projection but also the gradients. In section 3.7, the calculation of gradients is used to constrain the model and to favour small gradients in the currents in the magnetic east-west direction.

3.3   Data Selection

The selection of magnetometers to be used in this study is important. This section outlines why the magnetometer sites used in this study where selected.

To be able to perform comparisons between modelled divergence-free currents at different times the magnetometer sites must be the same. Changes within the number of or location of magnetometers will change the current system the model will evaluate. This means that when one compares the modelled current from times that have different selections of magnetometer sites the differences between currents cannot be credibly attributed to changes in conditions.

The goal of this study is to preform long time scale statistics on the auroral electrojets. To do this the magnetometer sites not only need long time periods of operation but also to be operating at the same time as enough other magnetometers that a model can be made with sufficient accuracy. A selection of twenty magnetometers in Fennoscandia from the IMAGE and INTERMAGNET magnetometer networks are chosen for this

study. They provide good spatial coverage of the region and they are available at the same time for over 19 years in total, with minute resolution data, and the coverage spans from the beginning of 2000 up to the end of 2019.

With this combination of magnetometer sites and using the cubed sphere grid of SEC poles, described in section 3.2, the sheet current densities across Fennoscandia can be modelled.
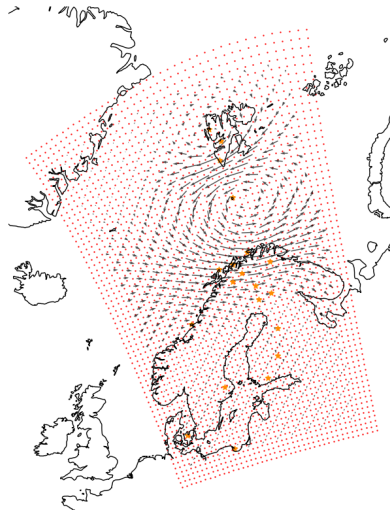
Figure 3.5: Plot showing the magnetometer location as stars, the cubed sphere SEC pole grid as red points and quivers are used to represent evaluated currents on a smaller cubed sphere grid.

Figure 3.5 shows the location of the magnetometers used in this study using orange stars, the SEC pole grid as red points and quivers show the current at the evaluation grid used for regional plots to visualise the impacts of different inversion and optimisation techniques tested.

3.4 Singular Value Decomposition and the Moore-Penrose Inverse

Singular Value Decomposition (SVD) is the technique that is used most commonly for the inversion requirements for SECS and to constrain the model to yield more physical results. The following section outlines how it works and relates it to the context of this study with the purpose of investigating divergence-free currents. Due to their nature the curl-free currents cannot be investigated by ground magnetometers, as discussed in section 2.2 and can be seen in equation 3.6. Therefore, the following methodology sections will focus on modelling techniques for divergence-free currents.

3.4.1 Background

Equation 3.4 and 3.5 show a linear dependence of the magnetic field from a divergence-free current, evaluated using SECS, on the amplitude of the SEC poles, $I_{0,df}$. Equation 3.14 represents this relation in terms of matrix algebra, where a matrix G, which depends on the relative positioning of the SEC poles and the points of evaluation, is multiplied by a vector containing the SEC pole amplitudes, $\mathbf{m}$, to find the magnetic field perturbations, $\mathbf{d}$.

$$G\mathbf{m} = \mathbf{d} \tag{3.14}$$

By evaluating the SECS model at the location of the magnetometers both G and $\mathbf{d}$ have known values. The SEC pole amplitudes, vector $\mathbf{m}$, is the variable to be found and doing so will enable the modelling of the magnetic field perturbations and currents anywhere. Multiplying both sides of equation 3.14 by the inverse of G, as shown in equation 3.15, would allow $\mathbf{m}$ to be found as $G^{-1}G$ becomes an identity matrix.

$$G^{-1}G\mathbf{m} = G^{-1}\mathbf{d}. \tag{3.15}$$

However, later in this section a different method for performing the inversion, that can be performed computationally and efficiently, will be discussed. For this method to be applied to the SECS problem it would be preferable if the matrix to be inverted was square, the reason for this be discussed later. So with that in mind, equation 3.16 shows relation 3.14 multiplied by G transposed giving $G^T G$ to be inverted so a solution for $\mathbf{m}$ can be found.

$$G^T G\mathbf{m} = G^T \mathbf{d} \tag{3.16}$$

$G^T G$ by its nature is always a square matrix so the inversion will now be possible and the solution for $\mathbf{m}$ can be written as

$$\mathbf{m} = [G^T G]^{-1}\mathbf{d}. \tag{3.17}$$

3.5 Singular Value Decomposition (SVD)

Singular value decomposition (SVD) is a technique that can be used to break down a matrix into three components, as shown in 3.18 (*Bart et al.* (2004)).

$$G = U\Sigma V^T \tag{3.18}$$

In the context of the SECS problem, G takes the form of the $3m \times p$ matrix in equation 3.19, where m is the number of magnetometers and p is the number of SEC poles. In equation 3.19, Gx_{mp} scales the amplitude of SEC pole p, in relation to the geometry of the system, for its contribution to the magnetic field observed at magnetometer m in direction x. Assuming static SEC poles and magnetometer locations, this G matrix can then be applied at each time step. However, if the SEC poles or magnetometers are not static, which is not the case for this study, then a new G matrix would have to be generated each time there is change in their positions. Matrices U and V are both

orthogonal and have dimensions $p \times p$ and $3m \times 3m$ respectively.

$$G = \begin{vmatrix} Ge_{11} & Ge_{12} & \implies & Ge_{1p} \\ Ge_{21} & Ge_{22} & \implies & Ge_{2p} \\ \Downarrow & \Downarrow & & \Downarrow \\ Ge_{m1} & Ge_{m2} & \implies & Ge_{mp} \\ Gn_{11} & Gn_{12} & \implies & Gn_{1p} \\ Gn_{21} & Gr_{22} & \implies & Gn_{2p} \\ \Downarrow & \Downarrow & & \Downarrow \\ Gn_{m1} & Gn_{m2} & \implies & Gn_{mp} \\ Gr_{11} & Gr_{12} & \implies & Gr_{1p} \\ Gr_{21} & Gr_{22} & \implies & Gr_{2p} \\ \Downarrow & \Downarrow & & \Downarrow \\ Gr_{m1} & Gr_{m2} & \implies & Gr_{mp} \end{vmatrix} \tag{3.19}$$

Equations 3.20 and 3.21 show how Σ is related to diagonal matrix S and how S is comprised of the singular values, σ, of the G matrix, where r is the rank of G (*Bart et al.*, 2004). Σ is of the same dimensions as G and contains zeros to fill the matrix where S does not provide any values.

$$\Sigma = \begin{vmatrix} S & 0 \\ 0 & 0 \end{vmatrix} \tag{3.20}$$

$$S = \begin{vmatrix} \sigma_1 & 0 & \dots & 0 \\ 0 & \sigma_2 & \dots & 0 \\ \vdots & \vdots & \ddots & \vdots \\ 0 & 0 & 0 & \sigma_r \end{vmatrix} \tag{3.21}$$

$$\sigma_1 \geq \sigma_2 \geq \dots \geq \sigma_r > 0$$

There are two purposes for decomposing the G matrix, the first is to find the Moore-Penrose inverse or "pseudoinverse" (*Dresden*, 1920; *Penrose*, 1955). The second purpose is that before finding the inverse truncation can be performed. This involves manipulating the diagonal matrix S in a way that applies basic smoothing to the SEC pole amplitudes (*Bart et al.*, 2004). This method is called truncated SVD. $G^T G$ is used, as stated previously in this study, this is because SVD requires $p \leq 3m$ and for SECS it is common for the number of poles to exceed the number of magnetometers multiplied by 3. When using $G^T G$ the matrix for SVD and inversion has dimensions $p \times p$ which is acceptable. In equation 3.22 $G^T G$ has replaced G in equation 3.18 and shows that due to the nature of Σ the SVD can be reduced. Where U_r and V_r are U and V reduced to the rank of G, r.

$$G^T G = \begin{vmatrix} U_r, U_{p-r} \end{vmatrix} \begin{vmatrix} S & 0 \\ 0 & 0 \end{vmatrix} \begin{vmatrix} V_r^T \\ V_{p-r}^T \end{vmatrix} = U_r S V_r^T \tag{3.22}$$

The Moore-Penrose inverse is found through relation 3.23 where the superscript $+$ denotes a psuedo-inverse.

$$[G^T G]^+ = V_r S^{-1} U_r^T \tag{3.23}$$

To smooth the solution, which in turn will smooth the amplitudes of the SEC poles, a condition can be applied to S in the form $\sigma < condition \times \sigma_1$ whereby smaller amplitudes are removed from the fitting. This helps to smooth the solution as there are not such large extremes in the amplitudes of the poles.

3.6 Removal of Telluric Currents

Following on from section 2.3, this section aims to discuss how to adjust for the impact of telluric currents on the SECS model and discusses the methods that can be used.

As discussed in section 2.3, telluric currents can have a significant effect on the magnetometer measurements at ground level. This is problematic because with a basic method for solving equation 3.17 to find the SEC pole amplitudes it is assumed that the magnetic perturbations measured are solely created from the currents in the ionosphere. There are two ways, that have been tested in this study, to adjust the set up that can, to a certain degree, account for the influence of telluric currents on the magnetometer measurements and subsequently the ionospheric currents derived, through SECS, from those measurements. Figure 3.6 has four panels each showing the different outputs of the SECS model. In order from left to right, the first panel shows the location and amplitude of the SEC poles. The second panel shows the divergence-free current vectors as quivers and to make magnitude variations clearer it is additionally shown by the colour of the background. The third panel shows magnetic perturbations on the ground. The east, B_e, and north, B_n, components of the ground magnetic field perturbations are shown as quivers, while the radial component, B_r, is shown as the background colour. The red quivers are the measurements of B_e and B_n at the magnetometer sites. The final plot is to verify if the model is finding magnetic field perturbations at the magnetometer sites that are comparable to the measurements. If the trend of points for each component is similar to y=x, the blue line through the plot, then the model is finding similar values to the measurements.
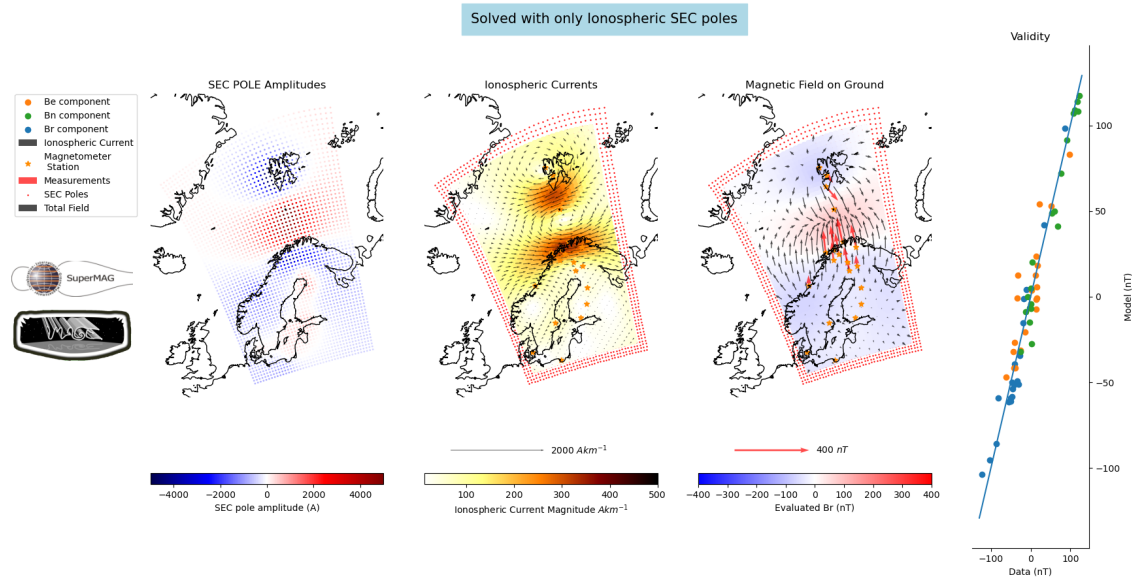
Figure 3.6: Plots showing the magnetic field, current, SEC pole amplitudes and the accuracy of a SEC model using only ionospheric SEC poles. Truncated SVD is used with a cutoff of 0.01. In the validity plot the model is plotted with the data so the accuracy of the solution at the magnetometer locations can be see by comparing the trend with the blue line that shows a y=x relation. Data has been taken from Longyearbyen, Bjørnøya, Tromsø, Hornsund, Abisko, Sodankyla, Nurmijarvi, Brorfelde, Ny-Ålesund, Hel, Rørvik, Sørøya, Andenes, Kevo, Kilpisjärvi, Muonio, Pello, Oulujärvi, Hankasalmi and Uppsala and is at 22:34 on the 5th of February 2000. Data retrieved via SuperMAG (Gjerloev, 2012)

3.6.1   Telluric Poles

The first method tested is very intuitive. The idea is that you place a second set of poles at the depth of the telluric currents and a superposition of the magnetic field from the telluric SECS and ionospheric SECS will be equal to the magnetometer measurements with a balance of amplitudes that mimics the ionospheric and telluric current contributions (*Pulkkinen et al.*, 2003b). In equation 3.24 the G matrix has become the G matrix from the ionospheric poles (in equation 3.19), denoted with a subscript *i*, merged horizontally with a G matrix from the telluric poles, denoted with subscript *t*.

$$
G = \begin{vmatrix}
Ge_{11_i} & Ge_{12_i} & \Longrightarrow & Ge_{1p_i} & Ge_{11_t} & Ge_{12_t} & \Longrightarrow & Ge_{1p_t} \\
Ge_{21_i} & Ge_{22_i} & \Longrightarrow & Ge_{2p_i} & Ge_{21_t} & Ge_{22_t} & \Longrightarrow & Ge_{2p_t} \\
\Downarrow & \Downarrow & & \Downarrow & \Downarrow & \Downarrow & & \Downarrow \\
Ge_{m1_i} & Ge_{m2_i} & \Longrightarrow & Ge_{mp_i} & Ge_{m1_t} & Ge_{m2_t} & \Longrightarrow & Be_{mp_t} \\
Gn_{11_i} & Gn_{12_i} & \Longrightarrow & Gn_{1p_i} & Gn_{11_t} & Gn_{12_t} & \Longrightarrow & Gn_{1p_t} \\
Gn_{21_i} & Gn_{22_i} & \Longrightarrow & Gn_{2p_i} & Gn_{21_t} & Gn_{22_t} & \Longrightarrow & Gn_{2p_t} \\
\Downarrow & \Downarrow & & \Downarrow & \Downarrow & \Downarrow & & \Downarrow \\
Gn_{m1_i} & Gn_{m2_i} & \Longrightarrow & Gn_{mp_i} & Gn_{m1_t} & Gn_{m2_t} & \Longrightarrow & Gn_{mp_t} \\
Gr_{11_i} & Gr_{12_i} & \Longrightarrow & Gr_{1p_i} & Gr_{11_t} & Gr_{12_t} & \Longrightarrow & Gr_{1p_t} \\
Gr_{21_i} & Gr_{22_i} & \Longrightarrow & Gr_{2p_i} & Gr_{21_t} & Gr_{22_t} & \Longrightarrow & Gr_{2p_t} \\
\Downarrow & \Downarrow & & \Downarrow & \Downarrow & \Downarrow & & \Downarrow \\
Gr_{m1_i} & Gr_{m2_i} & \Longrightarrow & Gr_{mp_i} & Gr_{m1_t} & Gr_{m2_t} & \Longrightarrow & Gr_{mp_t}
\end{vmatrix}
\tag{3.24}
$$

As a result the amplitude vector becomes equation 3.25.

$$\mathbf{m} = \begin{vmatrix} \mathbf{m_i} \\ \mathbf{m_t} \end{vmatrix} \qquad (3.25)$$

This means that under a perfect fit the sum of the magnetic field from the ionospheric and telluric SEC poles will be equal to the magnetic field measurements. Separate amplitudes for the ionospheric and telluric poles means that the ionospheric currents can be found with the telluric influences on the results accounted for. Figure 3.7 shows the solution when using ionospheric and telluric poles. There is no clear difference within the currents or accuracy of the new methodology. This may be due a number of reasons, such as the SVD truncation smoothing away the influence of the telluric poles, and in the future it could be improved by the addition of expected behaviours to the modelling or by applying the smoothing to the ionospheric G matrix and telluric G matrix separately before recombining to perform the inversion.

However, the main short coming of this method, even if improvements are made, is the size of the matrix for inversion and the extra amplitudes that need to be found. A compromise can be made, the ground currents can be assumed to be less changeable than the ionospheric currents and so to model them fewer SEC poles would be needed and they can be placed at greater depths to ensure the model solves the telluric pole amplitudes in a smoother way. But the telluric poles, even if technique improvements are made, add unnecessary complexity to the model.

Figure 3.7: Plots showing the magnetic field, current, SEC pole amplitudes and the accuracy of a SEC model using ionospheric and telluric SEC poles. Truncated SVD is used with a cutoff of 0.01. In the validity plot the model is plotted with the data so the accuracy of the solution at the magnetometer locations can be see by comparing the trend with the blue line that shows a y=x relation. Data has been taken from Longyearbyen, Bjørnøya, Tromsø, Hornsund, Abisko, Sodankyla, Nurmijarvi, Brorfelde, Ny-Ålesund, Hel, Rørvik, Sørøya, Andenes, Kevo, Kilpisjärvi, Muonio, Pello, Oulujärvi, Hankasalmi and Uppsala and is at 22:34 on the 5th of February 2000. Data retrieved via SuperMAG (Gjerloev, 2012)

3.6.2 Image Current

This method makes the assumption that the currents in the ground are solely due to induction from the ionospheric currents, an assumption used in *Pulkkinen et al.* (2003b), and as such a direct relationship between the ionospheric and telluric currents can be found. Therefore, the amplitudes of the telluric and ionospheric poles will be a factor of one and other. This relationship is defined by saying that the radial components of the magnetic field from the telluric currents and the ionospheric currents cancel at a defined depth. Work by *Juusola et al.* (2016) derived that an image current at a depth of $\frac{R_C^2}{R_I}$, where R_C is cancellation radius and R_I is the radius of the ionospheric currents, and telluric SEC pole amplitudes of $-\frac{\mathbf{m_I} R_I}{R_C}$, where $\mathbf{m_I}$ is the amplitudes of the corresponding ionospheric SEC poles, would cause a cancellation of the radial contributions from the two SEC pole systems.

Subsequently, a new G matrix is created that incorporates the contribution of the ionospheric and telluric SEC systems.

$$G = \begin{vmatrix} Ge_{11_i} + Ge_{11_t} & Ge_{12_i} + Ge_{12_t} & \Longrightarrow & Ge_{1p_i} + Ge_{1p_t} \\ Ge_{21_i} + Ge_{21_t} & Ge_{22_i} + Ge_{22_t} & \Longrightarrow & Ge_{2p_i} + Ge_{2p_t} \\ \Downarrow & \Downarrow & & \Downarrow \\ Ge_{m1_i} + Ge_{m1_t} & Ge_{m2_i} + Ge_{m2_t} & \Longrightarrow & Ge_{mp_i} + Ge_{mp_t} \\ Gn_{11_i} + Gn_{11_t} & Gn_{12_i} + Gn_{12_t} & \Longrightarrow & Gn_{1p_i} + Gn_{1p_t} \\ Gn_{21_i} + Gn_{21_t} & Gr_{22_i} + Gr_{22_t} & \Longrightarrow & Gn_{2p_i} + Gn_{2p_t} \\ \Downarrow & \Downarrow & & \Downarrow \\ Gn_{m1_i} + Gn_{m1_t} & Gn_{m2_i} + Gn_{m2_t} & \Longrightarrow & Gn_{mp_i} + Gn_{mp_t} \\ Gr_{11_i} + Gr_{11_t} & Gr_{12_i} + Gr_{12_t} & \Longrightarrow & Gr_{1p_i} + Gr_{1p_t} \\ Gr_{21_i} + Gr_{21_t} & Gr_{22_i} + Gr_{22_t} & \Longrightarrow & Gr_{2p_i} + Gr_{2p_t} \\ \Downarrow & \Downarrow & & \Downarrow \\ Gr_{m1_i} + Gr_{m1_t} & Gr_{m2_i} + Gr_{m2_t} & \Longrightarrow & Gr_{mp_i} + Gr_{mp_t} \end{vmatrix} \tag{3.26}$$

Equation 3.26 shows the G matrix for the new image current technique, where each element is the sum of the contributions from the telluric and ionospheric SEC poles and the subscripts *i* and *t* refer to the ionospheric and telluric components. Because the ionospheric and telluric systems are dependent on the same amplitudes they are superposed within the G matrix, making its size no different to when only ionospheric currents are considered. The new G matrix is inverted in the same way as the earlier methodology, by finding the Moore-Penrose inverse via truncated SVD.

The Figures in 3.8 show the solution of a SECS analysis with the cancellation depths for the image currents at 100, 500 and 1000 kilometres, respectively. When using a cancellation depth of 100km, which equates to a telluric current depth of approximately 300km, the evaluated B_r component for depths close to the surface match the measurements poorly leading to a disagreement with the telluric current depth used in *Pulkkinen et al.* (2003a). This behaviour can be reasoned from how the magnetic field from the image and from the ionospheric currents combine. The theta component of the magnetic fields add therefore as the cancellation depth is reduced, which in turn means the image current is closer to the surface, the SEC pole amplitudes must be reduced in order to correctly match the data. The theta component, once converted from local to global co-ordinates, is constrained by magnetometer measurements in the north-south

and east-west direction. Whereas, the radial magnetic fields subtract from each other, this is needed for them to cancel at the cancellation depth, and is only constrained by the radial magnetometer measurements. With twice as many measurements, the theta component has a higher weighting in the inversion. This is seen in how the model values for the global B_ϕ and B_θ are closer to the magnetometer measurements in figure 3.8a than the model B_r are to the B_r magnetometer measurements. To fit the B_ϕ and B_θ measurements, the SEC amplitudes must be reduced. Therefore, the magnitude of the evaluated B_r component compared to the measured B_r component is greatly reduced. For this study a cancellation depth of 500km is used for a few key reasons; it allows for a good fit with the data, it is shallow enough to have an influence over the inversion and lastly a cancellation depth of 500km can be equated to a telluric current at a depth of approximately 1000km which should discourage small scale structures in the telluric currents from having an influence over the model.

Figure 3.8: Plots showing the magnetic field, current, SEC pole amplitudes and the accuracy of a SEC model using ionospheric SEC poles and varied cancellation depths for the Image currents. Truncated SVD is used with a cutoff of 0.01. In the validity plot the model is plotted with the data so the accuracy of the solution at the magnetometer locations can be see by comparing the trend with the blue line that shows a y=x relation. Data has been taken from Longyearbyen, Bjørnøya, Tromsø, Hornsund, Abisko, Sodankyla, Nurmijarvi, Brorfelde, Ny-Ålesund, Hel, Rørvik, Sørøya, Andenes, Kevo, Kilpisjärvi, Muonio, Pello, Oulujärvi, Hankasalmi and Uppsala and is at 22:34 on the 5th of February 2000. Data retrieved via SuperMAG (Gjerloev, 2012)
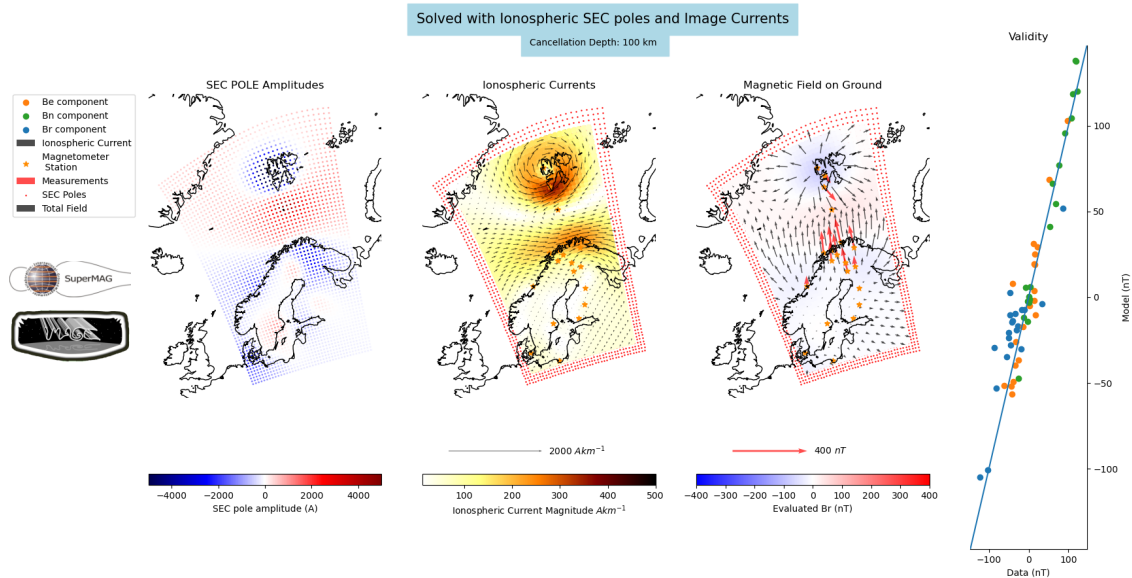
(a) Plot with a cancellation depth of 100km
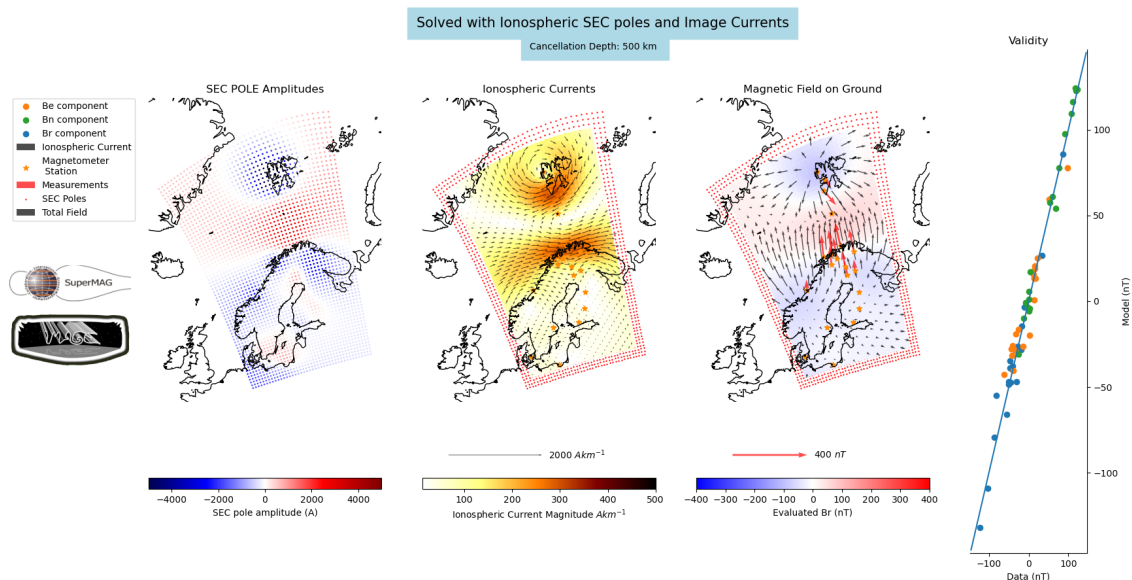
(b) Plot with a cancellation depth of 500km
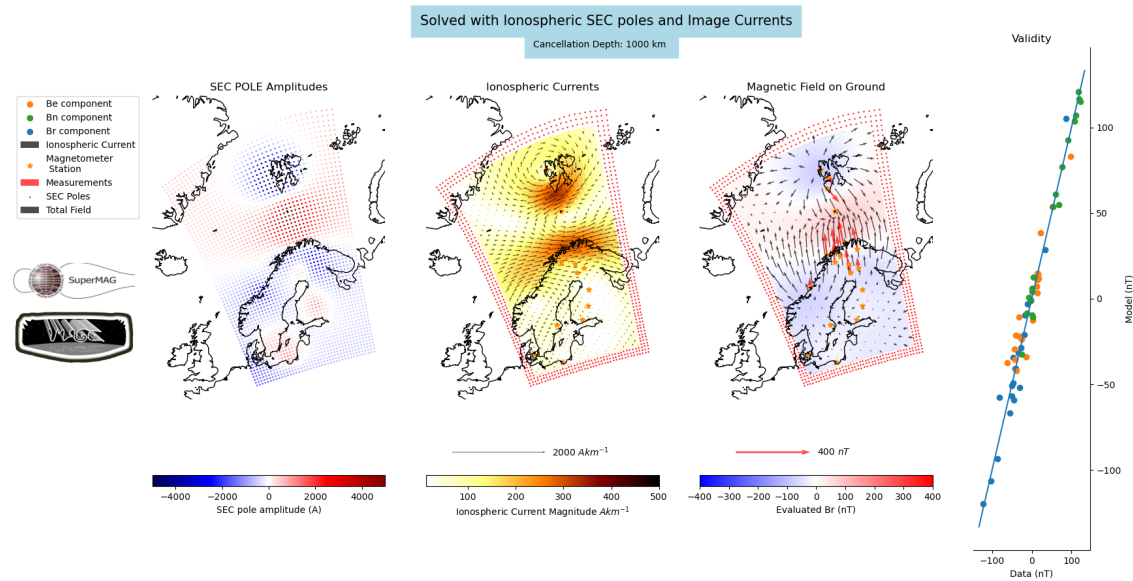
(c) Plot with a cancellation depth of 1000km

The shortcomings of this method are primarily due to an assumed fixed relationship between ionospheric and telluric currents, both temporally and spatially. The crustal properties over Earth can be highly variable in terms of composition which means the conductivity is very different and induction from ionospheric currents would in reality vary with this property. The wavelength of perturbations in the magnetic field also greatly affect the induced current's distribution in depth (*Jones*, 1980). To accurately adjust the model to compensate for the effect of telluric currents on ground magnetometer measurements, the telluric SEC pole method would be the best solution as it makes no assumption on the relationship between the ionospheric and telluric currents which should allow the model to be malleable to the impact of variable crustal conductances. However, a big advantage with the image current techique is that with an assumed relationship between ionospheric and telluric currents the G matrix (in equation 3.19) remains the same size as it would when not taking the telluric currents into account. This enables the use of a more coarse grid or a reduced computation time in comparison to using telluric poles.

After comparing the results and weighing up the advantages and disadvantages of each method, the image currents were used for this study. The reduced model complexity while capturing the telluric influences to a reasonable degree are considerable advantages for this study. This is because the data set being used is over 19 years of minute frequency data and any unnecessary model complexity will hinder the production of the data set within a reasonable time scale.

3.7 Solving a System of Equations

The previous sections have discussed methodology for creating the SECS model, using truncated SVD to smooth the solution and making adjustments that adapt the model for influences of telluric currents on ground magnetic field measurements. However,

there is still some work that can be done in improving the constraints on the model and coercing it to produce results that are a good representation of the data while typically exhibiting the behaviours that are expected of the current systems that are being modelled. In section 3.4, truncated SVD was discussed as a method of inversion and smoothing to find the amplitudes of the SEC poles that resemble a current backed up by physical understanding. In this section regularisation is introduced as an alternative method which allows the application of knowledge on the typical current system to constrain the inversion.

The last step in optimising the model set up is regularisation. In sections 3.4 and 3.6 truncated SVD is discussed and used to efficiently find the psuedoinverse of the G matrix (shown in equation 3.19) and manipulate the inversion to discourage large SEC pole amplitude variation in a small spatial frequency. Although this method is widely used with SECS analysis, other methods can yield much better results. The goal in improving the SECS solution is to add information and get a more physical output. In figures 3.6, 3.7 and 3.8 the currents show strong structure in both the east-west and north-south direction. The SECS analysis should find the large scale behaviours of the ionospheric currents and it can be argued that the output should have currents more closely resembling the typical east-west electrojets. To improve the model, the inversion needs to therefore incorporate constraints that discourage spatially rapid variations in the magnetic east-west currents when there is no significant indication from the data. Similarly, field-aligned currents are expected to have a smooth trend in magnetic east-west. The amplitudes of SEC poles can be a good representation of field aligned currents, under certain conditions. Therefore, an assumption of weak magnetic east-west gradients in the SEC pole amplitudes can be justifiably imposed on the solution. As a result, the horizontal currents will be encouraged into an electrojet structure. The regularisation technique utilised in *Laundal et al.* (2020) is the basis for the technique used in this study. Equation 3.27 is similar to that found in *Laundal et al.* (2020) however the covariance matrix isn't used here.

$$f_0 = (\mathbf{d} - G\mathbf{m})^T (\mathbf{d} - G\mathbf{m}) \tag{3.27}$$

f_0 is the cost function for when using standard least square. For an accurate representation of the data it must be minimised. This is logical as it is the difference between what is measured and what the model evaluates. This function is to be adjusted if extra information needs to added to the model. Equation 3.28 shows the final function f that wants to be minimised. It utilises the grid advantages discusses in section 3.2 by finding the gradient operator L_e that can be applied to $\mathbf{m}$ to find the magnetic east-west gradients allowing them to be constrained.

$$f = f_0 + \lambda_1 ||I\mathbf{m}||_2 + \lambda_2 ||L_e\mathbf{m}||_2 \tag{3.28}$$

$||I\mathbf{m}||_2$ is the euclidean norm of $\mathbf{m}$ (the SEC pole amplitudes) and λ_1 is the parameter that controls how limited its value can be. The purpose of minimising the euclidean norm of the SEC pole amplitudes is to encourage a less complex solution to the model, lower extremities in the amplitudes when compared spatially. $||L_e\mathbf{m}||_2$ is the euclidean norm of the magnetic east-west gradients of the SEC pole amplitudes. Minimising this parameter by increasing the value of λ_2 will reduce how much the SEC pole amplitudes will vary longitudinally. By differentiating the new cost function, equation 3.28, and

finding where it is equal to zero, a value for **m** can be found where the function is at its minimum. For example by differentiating the equation 3.27 and setting it equal to zero, equation 3.17 is found. Using this same approach with the improved cost function, equation 3.28, a new expression for the SEC pole amplitudes, **m**, can be derived that uses the desired regularisation. Equation 3.29 shows the new method for finding the SEC pole amplitudes.

$$\mathbf{m} = [G^T G + \lambda_1 I + \lambda_2 L_e^T \cdot L_e]^{-1} \mathbf{d} \tag{3.29}$$

λ_1 and λ_2 have to be balanced correctly to get the most physical result while also allowing the model to defy the expected behaviours when justified by the data. If λ_2 is too much larger than λ_1 then low longitudinal gradients are the most encouraged attribute, leading to the SEC pole amplitudes appearing as thin bands of consistent amplitudes. This occurs because the reduced influence of λ_1 allows high complexity latitudinaly and therefore rapid variations in amplitude as the latitude changes. On the other hand, if λ_1 is too much larger than λ_2 then variations in the amplitudes longitudinally can happen much quicker than is expected.
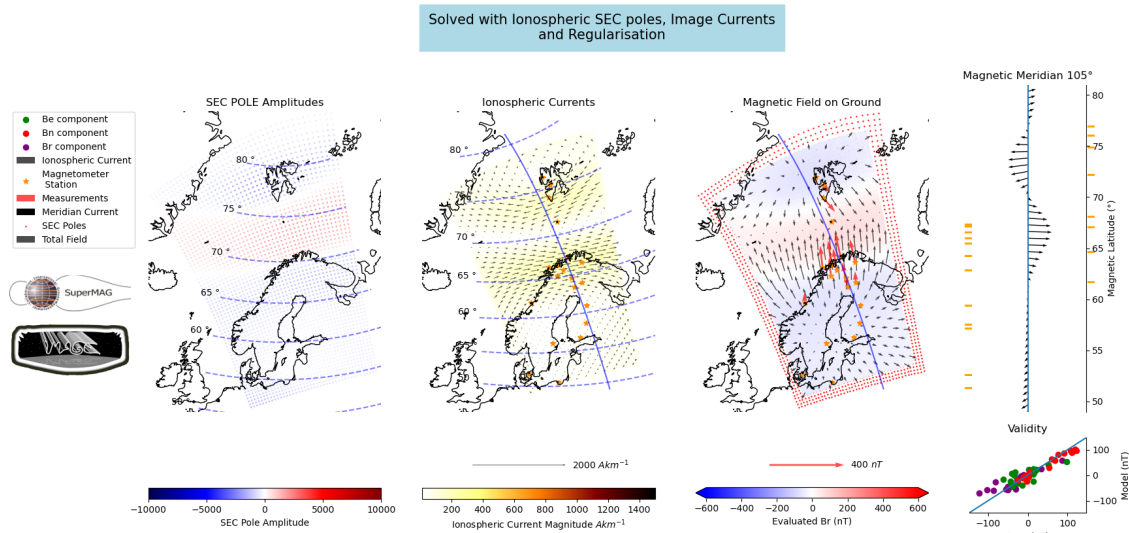

Figure 3.9: Plots showing the magnetic field, current, SEC pole amplitudes, accuracy of the SEC model using ionospheric SEC poles and Image currents. Regularisation from section 3.7 is used with λ_1 and λ_2 values of 10^{-23} and 10^{-21}, respectively.In the validity plot the model is plotted with the data so the accuracy of the solution at the magnetometer locations can be seen by comparing the trend with the blue line that shows a y=x relation. The blue line in the SEC pole amplitudes, ionospheric currents and magnetic field on ground plots shows the location of the magnetic meridian that is used for the statistical analysis of the data set. The SEC POLE Amplitudes plot contains geographic latitude contours every $10°$, shown as dashed blue lines, while the Ionospheric Currents plot contains geomagnetic latitude contours every $10°$, also shown as dashed blue lines. Data has been taken from Longyearbyen, Bjørnøya, Tromsø, Hornsund, Abisko, Sodankyla, Nurmijarvi, Brorfelde, Ny-Ålesund, Hel, Rørvik, Sørøya, Andenes, Kevo, Kilpisjärvi, Muonio, Pello, Oulujärvi, Hankasalmi and Uppsala and is at 22:34 on the 5th of February 2000. Data retrieved via SuperMAG (Gjerloev, 2012)

Figure 3.9 shows a solution using regularisation with λ_1 and λ_2 values of 10^{-23} and 10^{-21} respectively. Using this suitable balance, regularisation is chosen over truncated

SVD in this study because of the methods ability to add more information to the model which gives a model with more physical results.

3.7.1   Substorm Time Series Example

After performing the SECS analysis on a large temporal data set, a variety of data products can be produced. Most of these are introduced and discussed in chapters 4 and 5. The equivalent currents and radial magnetic field perturbations estimated along the $105°$ magnetic meridian can be presented as a time series and be used to show substorm dynamics. In this subsection a substorm list, based on auroral images taken from the IMAGE and POLAR satellites (*Frey et al.*, 2004a; *Liou*, 2010), is used to select periods within the night side magnetosphere when there is a substorm onset and meridian data. One example, out of over 200 events that where found, is presented and discussed to show the initial capabilities of this model and demonstrate further areas of research that are not the focus of this study.
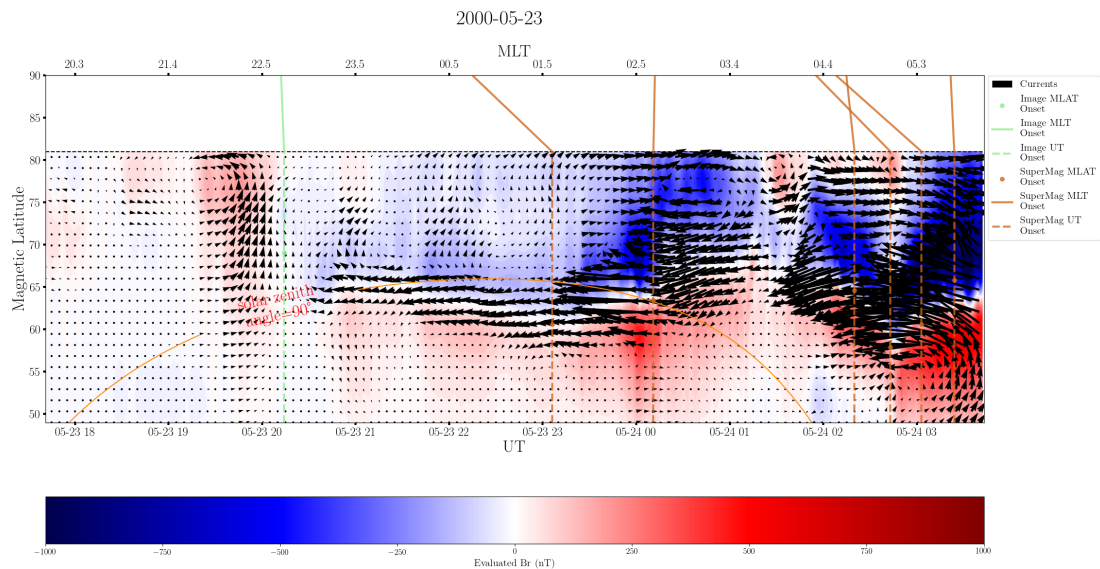

Figure 3.10: MLT and times series of the equivalent current and radial magnetic field perturbations evaluated along the $105°$ magnetic meridian for a substorm event on the 23rd and 24th of May 2000. The quivers show the direction and magnitude of the surface current densities and the background colour represents the direction and magnitude of the radial magnetic field perturbations. Dashed green lines, solid green lines, and green dots represent the UT, MLT and magnetic latitude of the onset of substorm from a substorm list that is based on auroral images from the POLAR and IMAGE satellites (Frey et al., 2004a; Liou, 2010). The brown dashed lines, solid brown lines and brown dots represent the UT, MLT and magnetic latitude of the onset of substorm from a substorm list that has been made by (Gjerloev, 2012; Newell and Gjerloev, 2011a,b) using magnetometer data.

Figure 3.10 is a substorm event that occurred on the 23rd and 24th of May 2000, it is an example of the initial capabilities of the SECS method developed in this study. The divergence-free currents and the radial component of the ground magnetic field perturbations are evaluated along the $105°$ magnetic longitude meridian, as is shown in figure 3.9. The data product from this technique is a minute resolution evaluation

along this meridian, whenever the magnetometers chosen for this study, which are in Fennoscandia, are available concurrently. In figure 3.10 the green lines and dots are used to show the MLT, magnetic latitude and time of substorm onsets from the IMAGE and POLAR based substorm list (*Frey et al.*, 2004a; *Liou*, 2010). The brown lines and dots are used to show the MLT, magnetic latitude and time of substorm onsets from SuperMAG (*Gjerloev*, 2012; *Newell and Gjerloev*, 2011a,b). A smaller angle between the dashed and solid lines show that the substorm onset occurred very close to the meridian, whereas larger angles show that the substorm onset occurred far from the meridian. The quivers in figure 3.10 show the strength and direction of the divergence-free current. The background colour of the plot shows the evolution of the evaluated radial magnetic field perturbations. The plots show an intensification of the auroral electrojets as a response to the onset of substorms and show that B_r tracks the north-south motion of the centre of the electrojets. Another feature within this plot and others that have not been presented is periodic fluctuations within the radial magnetic field which suggest that this model allows a visualisation of ULF (ultra low frequency) waves along magnetic field lines (e.g. between 01 and 02 UT). The dynamics within this plot and others made are not the focus of this study but they are an example of the potential of the SECS technique, they demonstrate how the initial data product can be used for a wide range of investigation and prove to be a great way to visualise the SECS model output to enable easier identification of features, trends and phenomena.

3.8   Electrojet Detection Algorithm

This section outlines the steps taken to systematically identify the properties of the auroral electrojets that are found within the sheet current densities evaluated along the $105°$ magnetic meridian. In the following section an algorithm is introduced that uses a sheet current density latitude profile to detect the auroral electrojets between $49°$ and $81°$ magnetic latitude. Electrojet properties such as width, peak sheet current density and total current through the electrojet are found. This allows statistical interpretations of electrojet properties to be performed in chapter 5. To analyse the nature of the auroral electrojet statistically, an algorithm has been derived to take the minute periodicity magnetic east-west sheet current density profiles and extract the boundaries, limits and total current though the electrojet. Figure 3.11 shows an artificial east-west sheet current density profile and demonstrates how the algorithm finds electrojet boundaries.
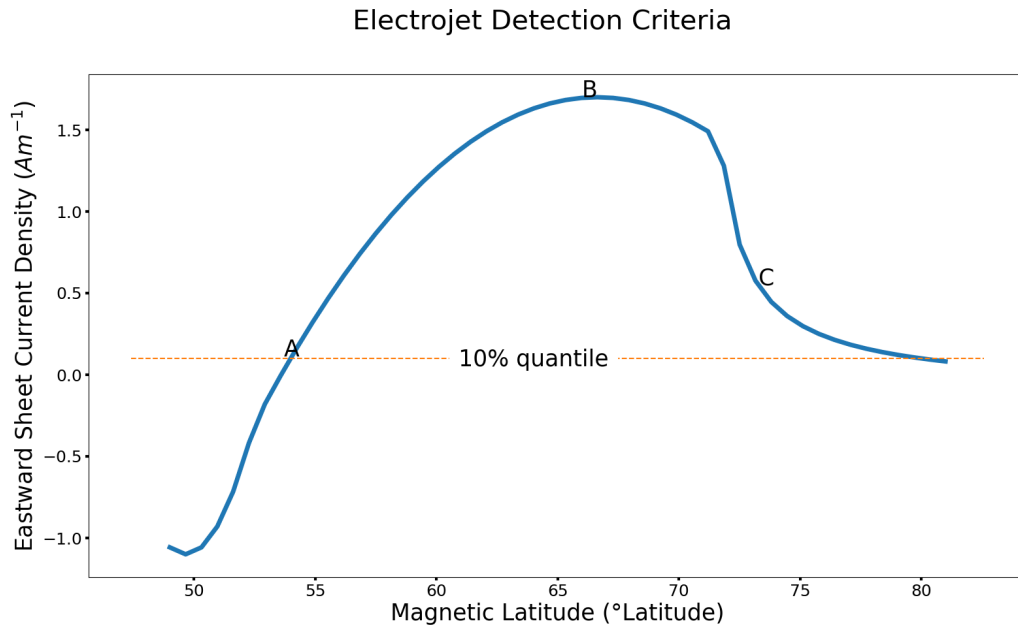
Electrojet Detection Criteria

Figure 3.11: (A). If the curve has a sufficient gradient then the boundary can be defined by where the curve crosses the 10% quantile. (B). Plateaus in the electrojet are exempt from the gradient threshold by allowing sheet current densities greater than 40% of the mean sheet current density between the quantile crossing points (or up to the end of the meridian if there isn't any) to be excluded from the gradient criteria. (C). When the curve doesn't cross the 10% quantile or the gradient of curve becomes shallow before reaching the 10% quantile, the boundary can be defined by where the gradient goes below 60% of the mean gradient between the quantile crossing points (or up to the end of the meridian if there isn't one).

First, the 10% quantile for the absolute east-west sheet current densities in the profile is found. Then the algorithm looks for the point where the profile crosses this boundary (when looking for the westward electrojet it looks for where the profile crosses the 10% quantile multiplied by -1). When there isn't a crossing for the equatorward or poleward boundary or both, then the crossing points are set at the corresponding limit of the meridian. To then improve these boundaries the steepness of the profile is considered. Near to the boundaries the gradient is expected to have a greater magnitude. The differential criteria is set that it must be greater than 60% of the mean absolute gradient between the initial electrojet boundaries. To ensure plateaus around the peak of the electrojet don't get affected, sheet current densities greater than 40% of the mean sheet current density between the initial boundaries are exempt from the differential criteria. The total current through the electrojet is then found by integrating the profile between the boundaries. The width can be found by finding the difference between the boundaries. And the peak sheet current density can be find by looking for the maximum value between the boundaries.

Figure 3.12 depicts three real sheet current density profiles and the electrojets boundaries found using the method. The plot shows that the algorithm has a relaxed criteria that leads to weak profiles still recording electrojets. Therefore, when using the data set it is important to apply further constraints. Typically this has been done by setting a minimum for the peak value of the electrojet detected.
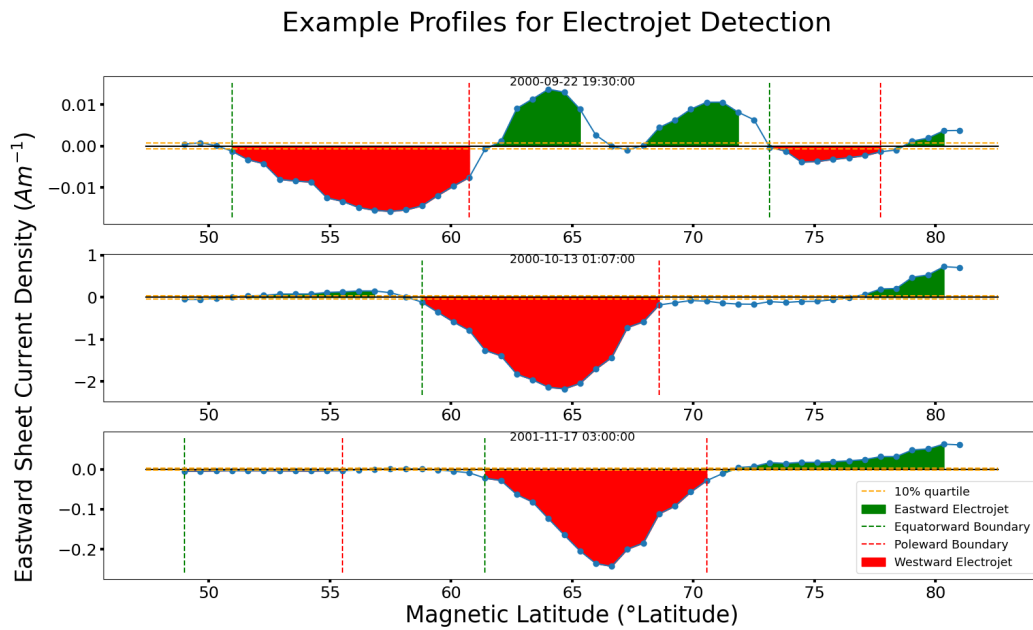
Figure 3.12: Three example profiles of currents in the magnetic east-west direction along the meridian, demonstrating the electrojet detection algorithm.

For the first profile in figure 3.12 the algorithm has detected two westward electrojets, one of which may be considered weak. This can give important information on areas where the electrojet is split into multiple parts. With this in mind, information from up to three of the strongest electrojets is recorded (the maximum number of electrojets detected per minute is six, three westward and three eastward electrojets). These properties allow an investigation into the disruption of the electrojet, presented and discussed in section 5.2.

Chapter 4

Validation and Summary Statistics

In this chapter the results produced from the methodology discussed in chapter 3 are checked against other data sets and against current knowledge to confirm the validity of the method. The results are summarised in some long term statistics to produce an overview of the data products and to demonstrate the plethora of opportunities for investigation, discussion and further research that they can provide.

4.1   SECS and AMPS Comparison

The AMPS model (*Laundal and Toresen*, 2018) can be used to take an input of solar wind parameters and yield the most likely divergence-free current and ground magnetic field perturbations. AMPS is useful for this study because the divergence-free current and radial magnetic field perturbations derived from the SECS model are parameterised by SW and IMF parameters, and by averaging our meridian profiles during similar conditions, a comparison is possible. This section uses the AMPS model to validate that the model that has been made is producing good results.

Average Current Structure IMF Bz>0
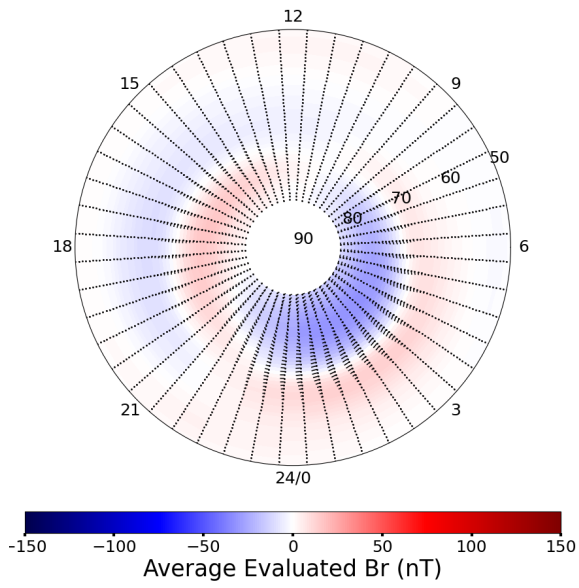
(a) Positive IMF Bz

Amps Current Structure Bz= +5
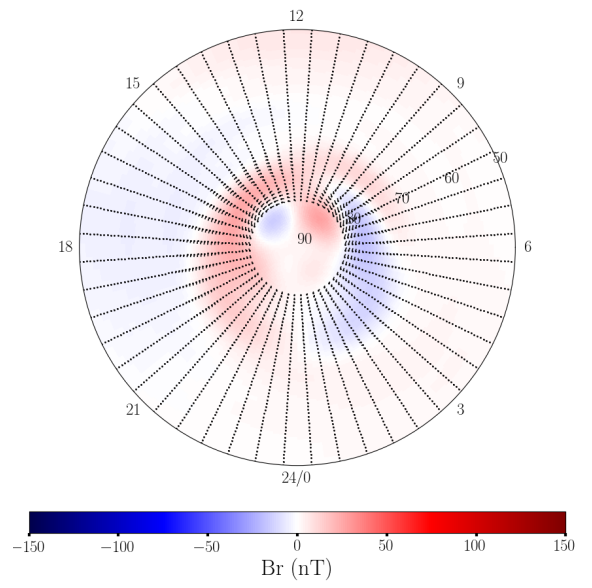
(b) IMF Bz=+5, IMF By=0

Average Current Structure IMF Bz<0

(c) Negative IMF Bz

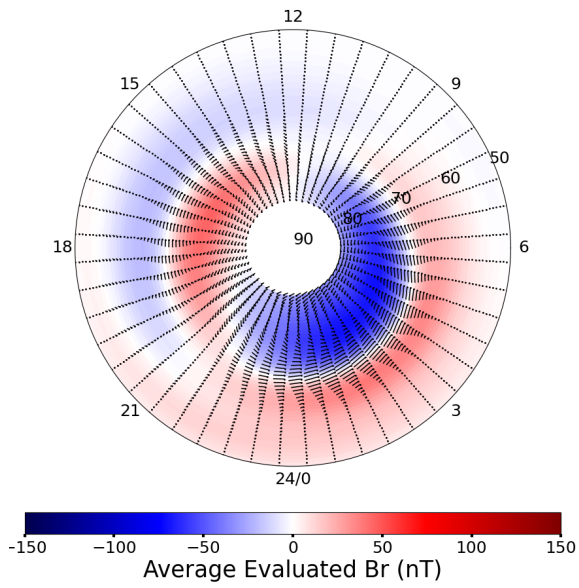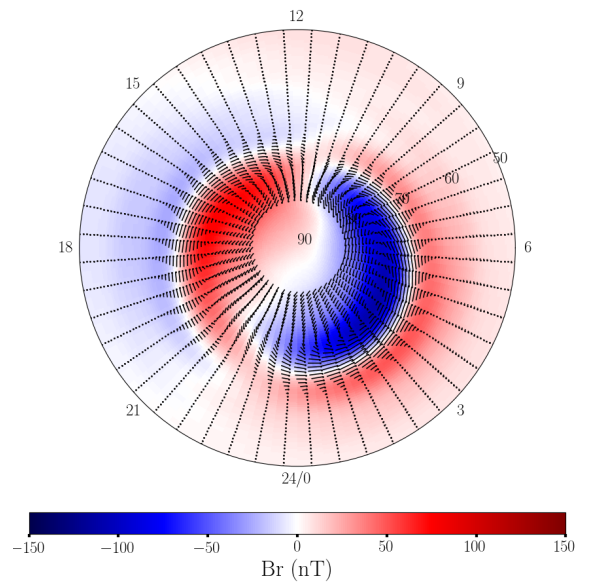Amps Current Structure Bz= -5

(d) IMF Bz=-5, IMF By=0

Average Current Structure IMF By>0

Amps Current Structure By= +5

-150   −100   −50   0   50   100   150
Average Evaluated Br (nT)

−150   −100   −50   0   50   100   150
Br (nT)

(e) Positive IMF Bz

(f) IMF Bz=0, IMF By=+5

Average Current Structure IMF By<0

Amps Current Structure By= -5

-150   −100   −50   0   50   100   150
Average Evaluated Br (nT)

−150   −100   −50   0   50   100   150
Br (nT)

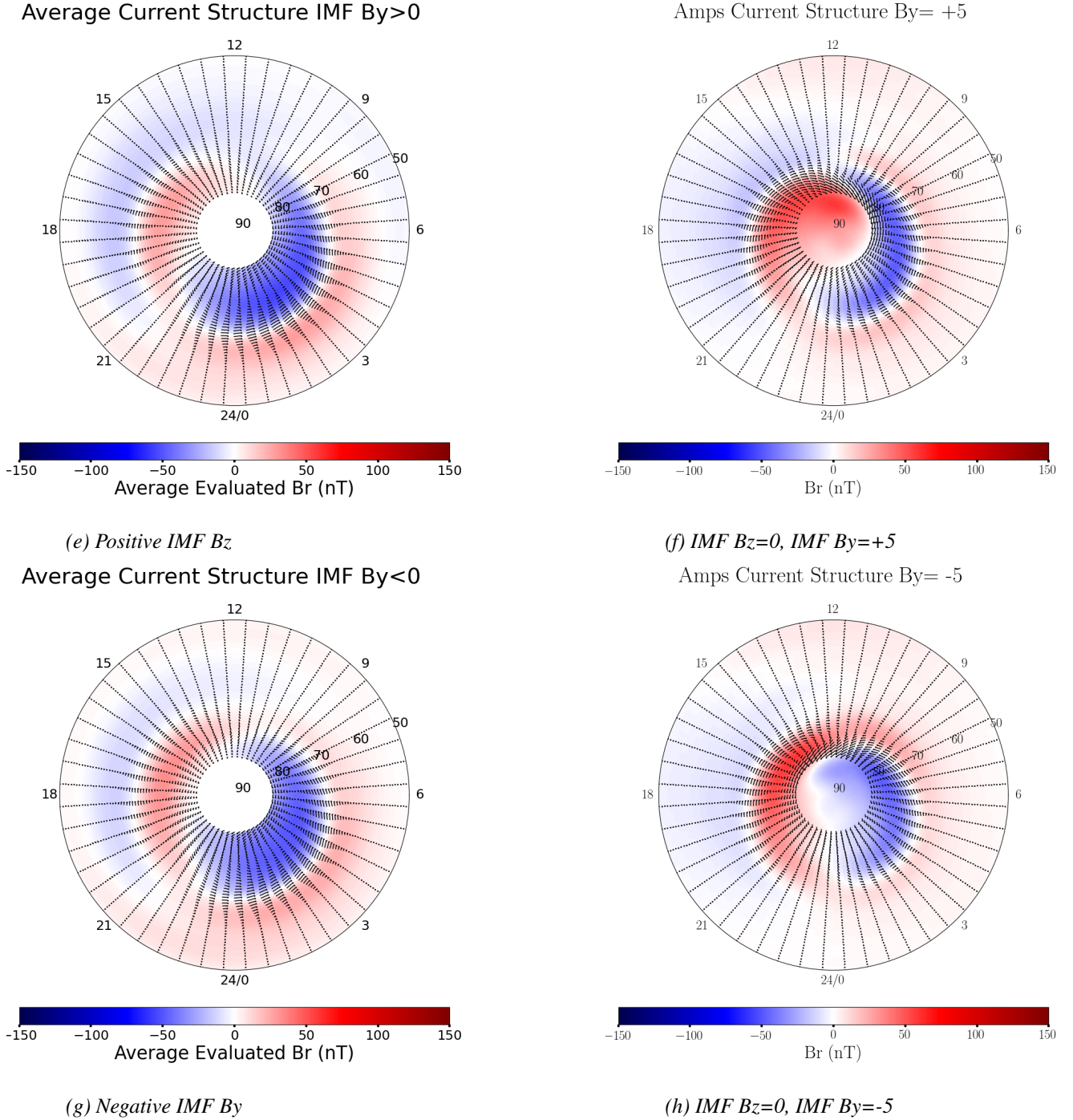*(g) Negative IMF By*

(h) IMF Bz=0, IMF By=-5

Figure 4.1: SECS average current structure for various IMF conditions compared with the AMPS predicted structure (Laundal and Toresen, 2018). On the left the equivalent sheet current densities and radial magnetic field perturbations evaluated along the 105° magnetic meridian are placed in bins of size 0.5 MLT and averaged. For each plot the evaluated meridian properties are first filtered by the IMF condition that is present at the time ($B_z > 0$, $B_z < 0$, $B_y > 0$ and $B_y < 0$), using data from OMNI (King and Papitashvili, 2005), before being binned and averaged. On the right are equivalent sheet current densities evaluated using the AMPS model every 0.5 MLT and at the same magnetic latitudes that are used to evaluate the proprieties along the meridian. The radial magnetic perturbations using the default AMPS mlt-mlat grid. The AMPS inputs for solar wind velocity, dipole tilt and f10.7 solar flux are 350kms$^-$1, 0°, 80 solar flux units respectively. While, the IMF inputs are varied for each plot

Figure 4.1 shows the average divergence-free currents and radial magnetic field

evaluated along the meridian using the SECS model when the IMF is under 4 specific conditions that are expected to produce different structures (left side). Similar conditions are then put in the AMPS model in order to draw a comparison (right side). Unfortunately an exact match between these models cannot be expected due to the different nature of how the figures are produced. The AMPS model takes an input of exact solar wind and IMF conditions to derive the divergence-free currents and radial magnetic field. Whereas, the SECS model is filtered by a condition and then averaged. This means that the SECS model can be skewed due to anomalous events and variable solar wind conditions. The SECS model is derived using real magnetometer data and can be considered, in essence, to form an interpolated grid to evaluate the properties. The same cannot be said about the AMPS model. The differences between these models is also an advantage as there is no overlap between the methods and similarities between the two can be ascribed to the validity of the SECS model. As expected from the current knowledge of IMF - magnetosphere interactions, the models under a negative B_z show much stronger currents and magnetic field perturbations due to the increased day side reconnection rate. The shape and latitude of the cell like structures within figure 4.1c and d are very similar. But, the primary take away is the variation between the features seen in figure 4.1a, where B_z is positive, and 4.1c, where B_z is negative. These plots demonstrate the changes that would be expected from vastly different reconnection rates and IMF - magnetosphere coupling. This following of expected behaviours from already well known physics combined with comparable changes in the AMPS model provide a good source of validation.

Figure 4.1e to h show the SECS and AMPS model when IMF B_y has different polarities. The current and radial magnetic perturbations show significantly comparable structure between the SECS and AMPS model. The changes in AMPS model output due to a different B_y can be similarly observed in the SECS model, for example the positive B_r cell is poleward of the negative B_r cell at 12 MLT for a positive B_y and they are switched for a negative B_y. Most importantly, the similarity of the current structures observed in the models bring validity to studies into the current output from the SECS model.

In resolution of this section, the SECS model created within this study shows enough similarity with the AMPS model and with the expected physical response to changes within the IMF conditions that it can be said that there is indeed validity in this model. Consequently it can be said that the application of the SECS method has be done successfully and correctly.

4.2   Electrojet Detection

In this section, figures on the occurrence and properties of the electrojets, that are detected using the technique discussed in section 3.8, are presented. Using the algorithm, the first three strongest eastward and the first three strongest westward electrojets are detected and recorded. The strongest electrojet, referred to as the primary electrojet, is the focus of this section.
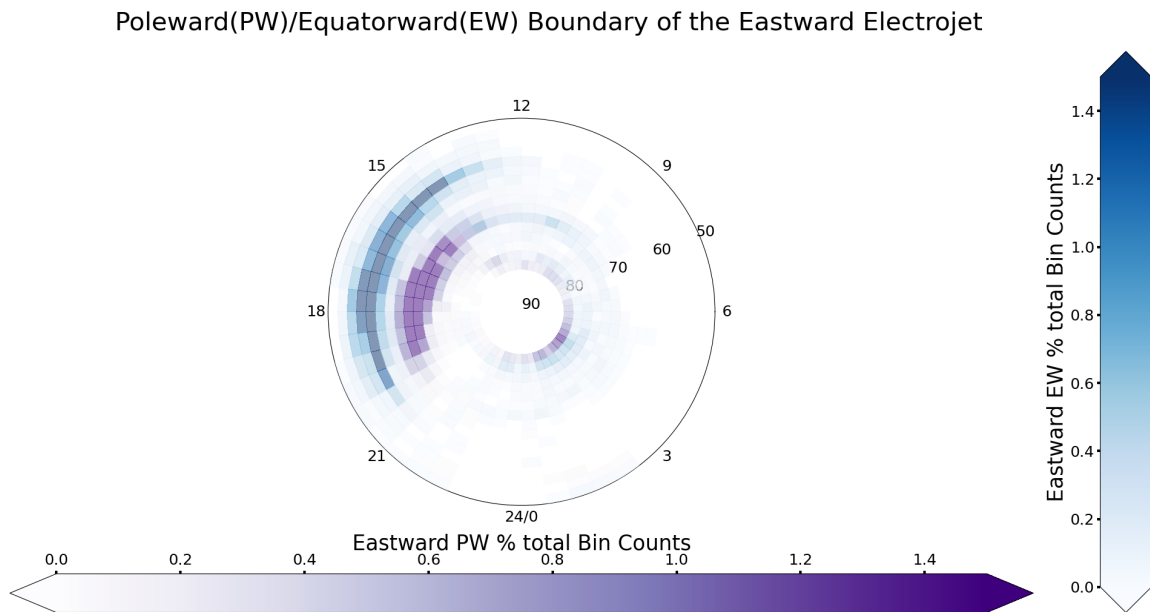
Poleward(PW)/Equatorward(EW) Boundary of the Eastward Electrojet

Figure 4.2: Polar histogram showing the eastward electrojet's most common location of poleward and equatorward boundaries for the strongest electrojet detected per minute with a peak sheet current density greater than $0.05Am^{-1}$.

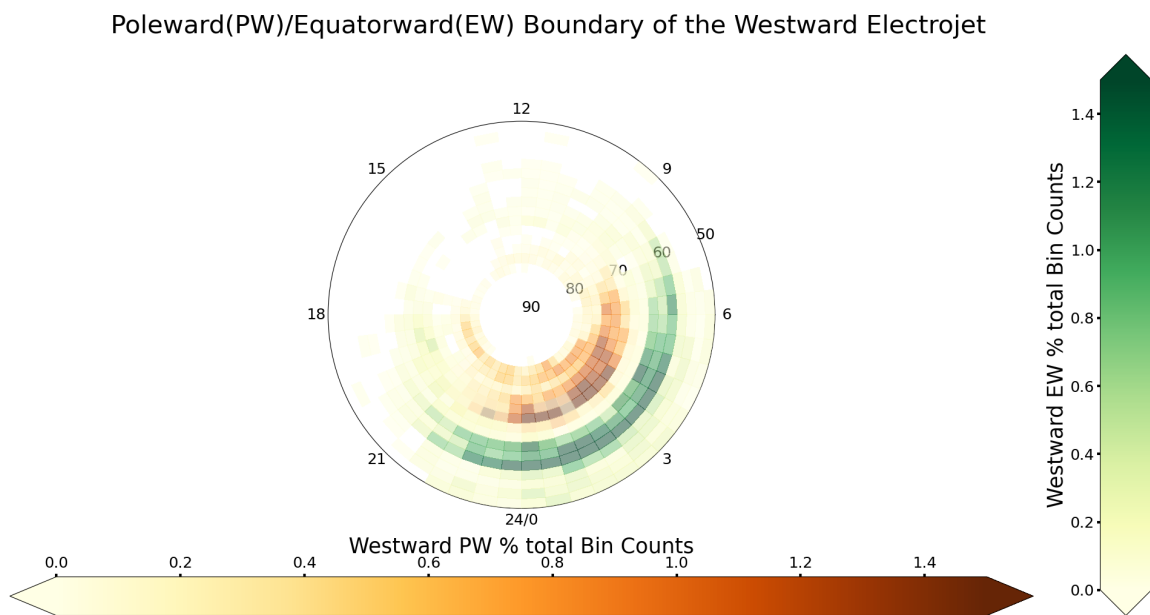Poleward(PW)/Equatorward(EW) Boundary of the Westward Electrojet

Figure 4.3: Polar histogram showing the westward electrojet's most common location of poleward and equatorward boundaries for the strongest electrojet detected per minute with a peak sheet current density less than $-0.1Am^{-1}$.

In figure 4.2 the poleward and equatorward boundaries of the primary eastward electrojet, that have a peak sheet current density greater than 0.05 Am^{-1}, are placed in mlt and mlat bins of size 0.5 and 2 respectively. The bins have subsequently been normalised by the total number of primary eastward electrojets that contribute to the histogram. In terms of the MLT location of the electrojets, it can be seen clearly that they are most commonly observed between 15 and 20 MLT. In comparison with the SECS plots in figure 4.1 there is an agreement that the algorithm has worked. The stronger

currents for the eastward electrojet, under all IMF conditions, are centred around this MLT window and bounded by comparable mlats to the most common poleward and equatorward boundaries in the histogram. Furthermore it is expected that the eastward electrojet will become more disjointed, weaker and harder to detect as the pre-midnight sector is approached anti-clockwise from the dusk flank. This is the region where the Harang discontinuity alters the dynamics. In figure 4.3 the polar histogram is repeated for the westward electrojet, where the peak sheet current density is required to be greater than $0.1\ Am^{-1}$. In this figure it can be seen, once again, that the algorithm is working effectively by comparing the high count bins with regions of elevated westward currents in the SECS plots within figure 4.1. There is still significant westward electrojet detection extending into the pre-midnight sector, however, this is expected from the current understanding of the Harang discontinuity, see figure 2.8. The variable nature of the Harang discontinuity due to its substorm origin explains the reduced detection of the westward electrojet within the pre-midnight sector when compared with the post-midnight to 5 MLT sector.

In summation, figures 4.2 and 4.3 not only demonstrate statistics that agree with plots of the average values from the initial meridians, justifying the effectiveness of the electrojet detection algorithm, but also agree with the current understanding of the eastward and westward electrojet. This furthers the validity of the SECS model and justifies that the electrojet detection algorithm extracts the information from the meridians in a correct manner and produces a data product that agrees with known physics.

4.3 Solar Variability Effects on Polar Equivalent Currents

This section uses knowledge on how solar activity affects geomagnetic activity, and subsequently polar ionosphere characteristics, to validate the integrity of the SECS model and electrojet detection algorithm.
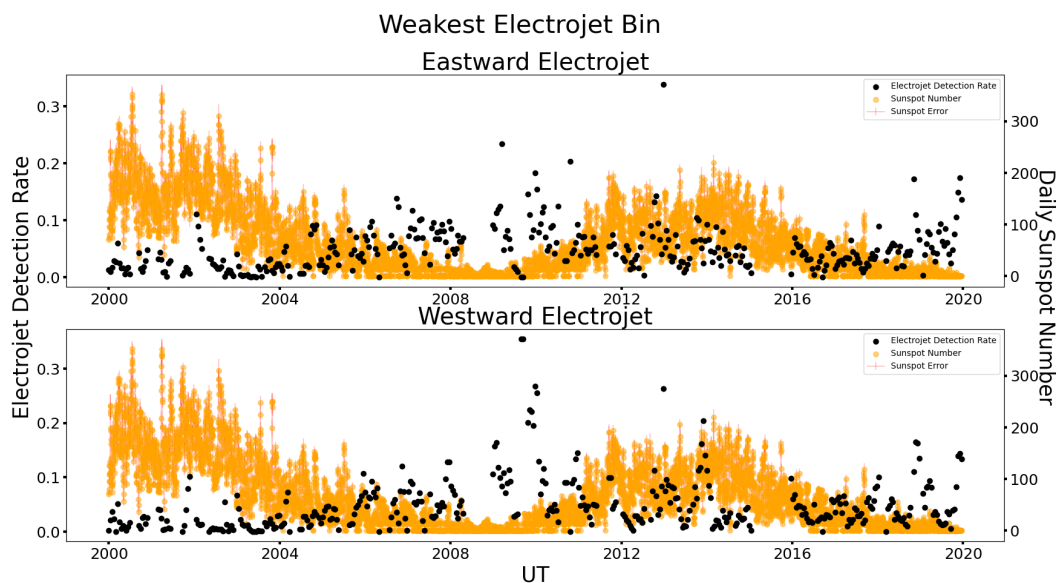

Figure 4.4: Daily sunspot number and detection rate of the weakest primary electrojet current bin normalised by the data coverage. The daily sunspot number has been taken from SILSO World Data Center (0).
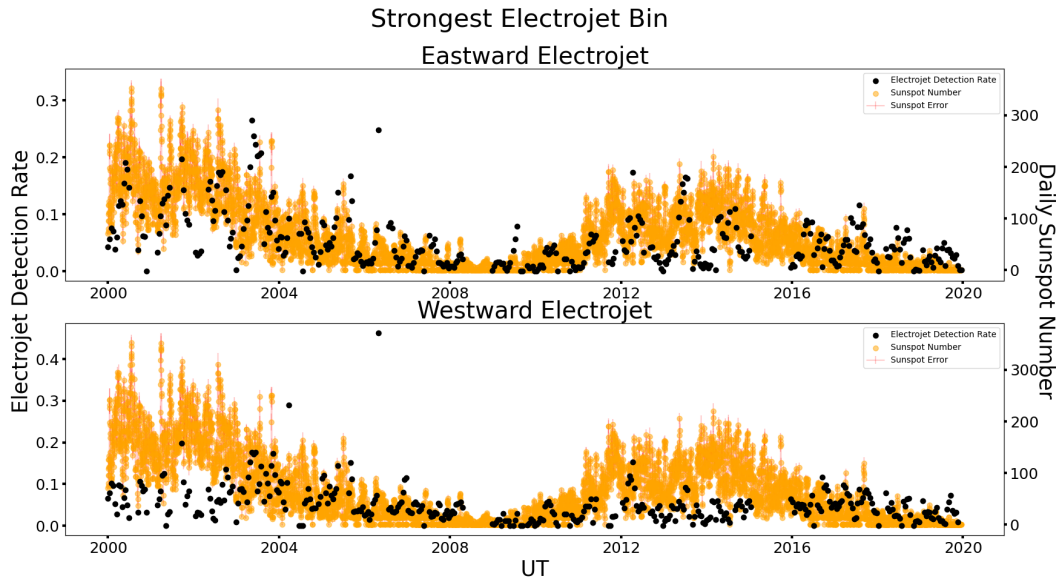
Figure 4.5: Daily sunspot number and detection rate of the strongest primary electrojet current bin normalised by the data coverage. The daily sunspot number has been taken from SILSO World Data Center (0).

The solar cycle, introduced in section 2.1, is a variability in solar activity over a period of average 11 years. A proxy for solar activity is the number of sunspots on the photosphere. Figures 4.4 and 4.5 use the sunspot number to visualise if a similar solar cyclic trend is observable within the electrojets. To create these figures, the eastward and the westward electrojets are independently sorted into 20 quantile bins based on the total current through the electrojet. A rolling window with a frequency of 15 days and a size of 30 days is applied to the binned jets to find how many times an electrojet of each bin is detected. To adjust for periods where there is no data from the SECS model, due to gaps within magnetometer data, the counts are then normalised by the amount of data available for each rolling window. This means that the resulting values represent how often an electrojet of each bin strength is found as a fraction of the opportunity for an electrojet to be detected, in terms of data being available. Figures 4.4 and 4.5 show the results from the bin with the lowest current boundaries and highest current boundaries respectively. It can be seen that the eastward and westward electrojet detection in figure 4.4 shows an anti solar cycle trend. While, figure 4.5 shows a trend comparable to the solar cycle. The figures show that during weak solar activity it is more likely that a weak electrojet is detected. while in a periods of high solar activity it is more common to detect a stronger electrojet. With our current understanding of solar impacts on geomagnetic activity this is justified. Higher solar activity is known to cause a greater disruption to the magnetosphere, an increase in dayside reconnection, more dynamic IMF magnetosphere coupling and an increase in ionospheric plasma density. The resulting impacts on the polar ionosphere are an increase in the amount and velocity of magnetic field lines convected across the polar cap. Consequently, the tailward reconnection is more frequent and releases a greater amount of energy. This can then be seen within the dynamics of the magnetic flux return flow along the dawn and dusk flanks of the polar ionosphere. Through the relations, equations and theories discussed within chapter 2, the electrojets are amplified in strength.

The detection of electrojets in relation to their strength has shown a clear solar cycle trend that is justified by the current physical understanding of solar-magnetosphere-ionosphere interactions. This therefore adds to the validity of the SECS model and electrojet detection algorithm.

4.4   Data Bias

The section presents the biases within the data set from model. This will allow consideration to be taken when analysing the results in chapter 5.

All sites must be available at the same time to create the SECS model. The reason for this is that if the site coverage changes, differences in the current and magnetic field that is modelled between different magnetometer set ups cannot be clearly attributed to changes in conditions. Also, to perform long period statistics it is desirable to keep the location of the SEC poles, evaluation points and magnetometer sites consistent. Otherwise, all elements of the model would have to be recalculated every time there is a change. If this can occur for each minute of the data set then the time it would take to compute the SECS model would make such a study as this impossible to perform within a sensible time. Therefore, when one site has no data for a specific time there is no data from the SECS model.
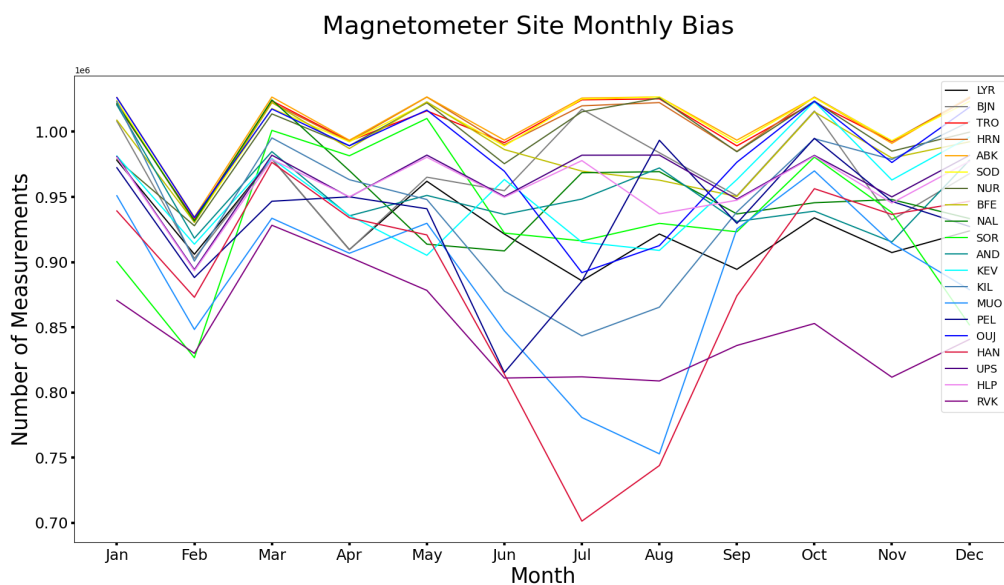

Figure 4.6: Monthly bias in data availability for each site used for the SECS analysis
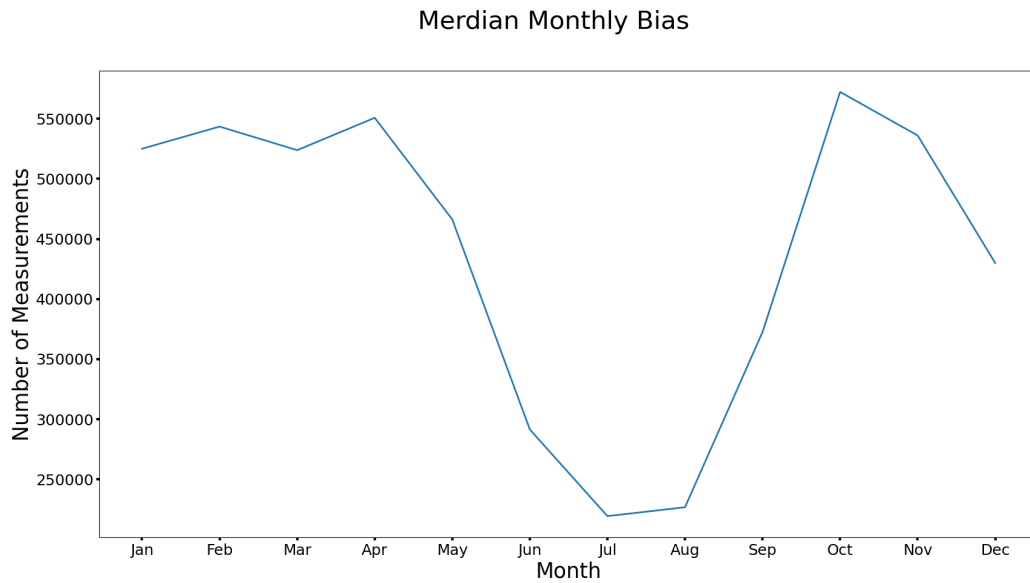
Figure 4.7: Monthly bias for when all the sites selected have data at the same time

Figure 4.6 and 4.7 show the amount of data available in each site that is used for the study each month and the amount of data when all the sites are available together each month respectively. A number of sites show a dip in the amount of data from May until October. Most significantly Muonio (MUO) and Hankasalmi (HAN) show around 30% less data in July and August respectively. This is shown clearly in figure 4.7 where the number of times the meridian is evaluated in July and August is less than 50% of the surrounding months. This will unfortunately make the summer less statistically valid than other seasons. However with time period of data chosen, there will still be significant validity to any trends observed during the summer.

There is also a yearly bias in the availability of data from the magnetometer sites at the same time.
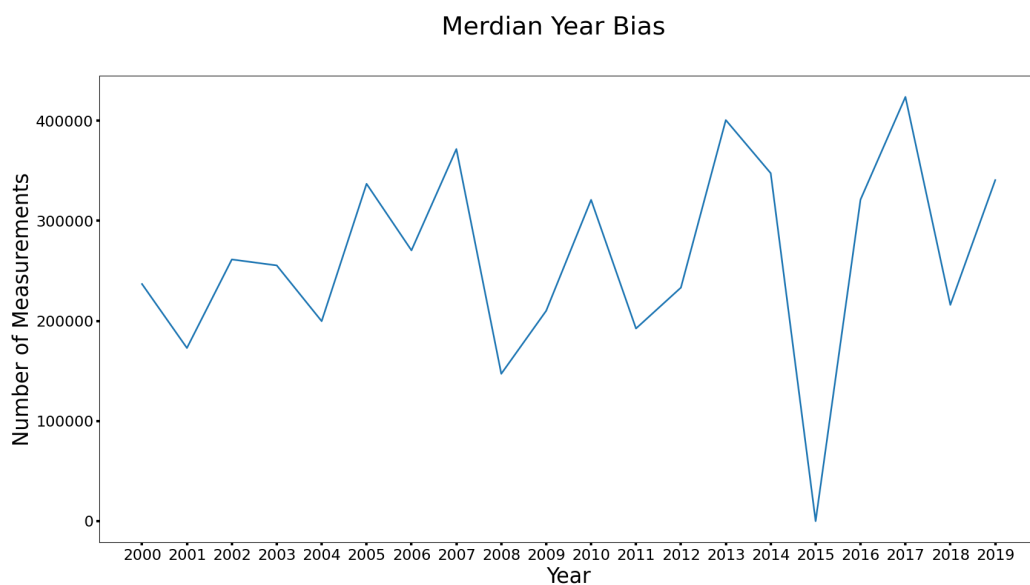

Figure 4.8: Yearly bias in data availability when all sites are available concurrently

Figure 4.8 shows the amount of times the model is able to evaluate properties along the meridian. There is a large in 2015 this is due to the magnetometers in Muonio and Hankasalmi not being available for most of that year. The reasons for this are unknown.

Another the bias that is checked is the amount of times the model is able to evaluate properties long the meridian at each MLT sector.
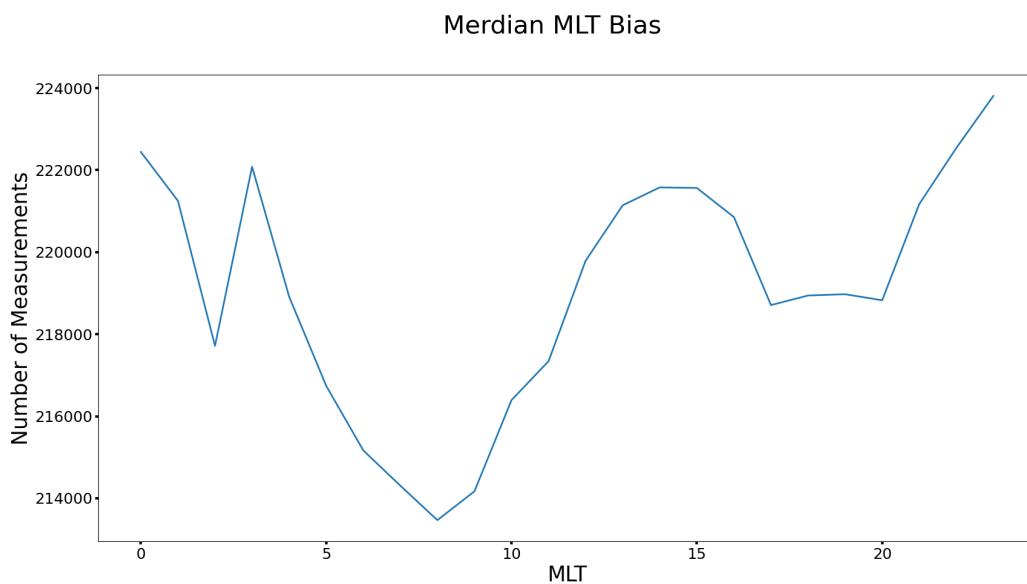
Figure 4.9: MLT bias in data

Figure 4.9 shows the amount of times properties along the meridian are evaluated. There are some fluctuations between each MLT however, the differences are insignificant and unlikely to cause noticeable biases within any trends observed in chapter 5.

A number of studies use a dipole tilt angle to sort data instead of seasons, an advantage is that you have a defined IMF-magnetosphere geometry making it easier to draw conclusions from the results. However, it is known that when selecting a magnetic meridian it will spend more time in certain MLTs depending on the tilt angle. This therefore means that there will be greater data at some MLTs than other for the currents and magnetic field perturbations evaluated along the meridian.

Merdian MLT Bias for Dipole Tilt<-10
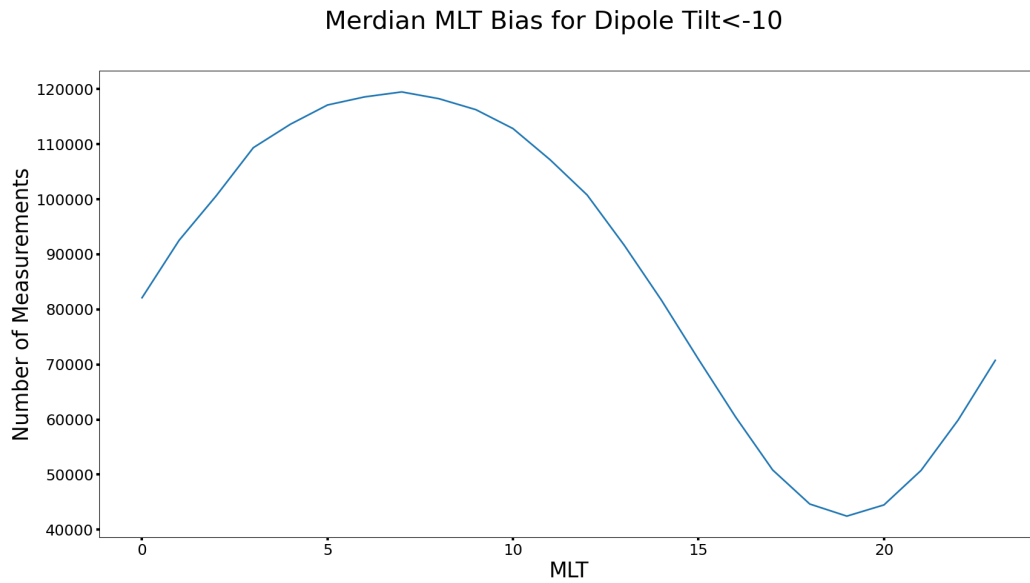
Figure 4.10: MLT bias in data for a dipole tilt angle less than $-10°$

Merdian MLT Bias for Dipole Tilt>10
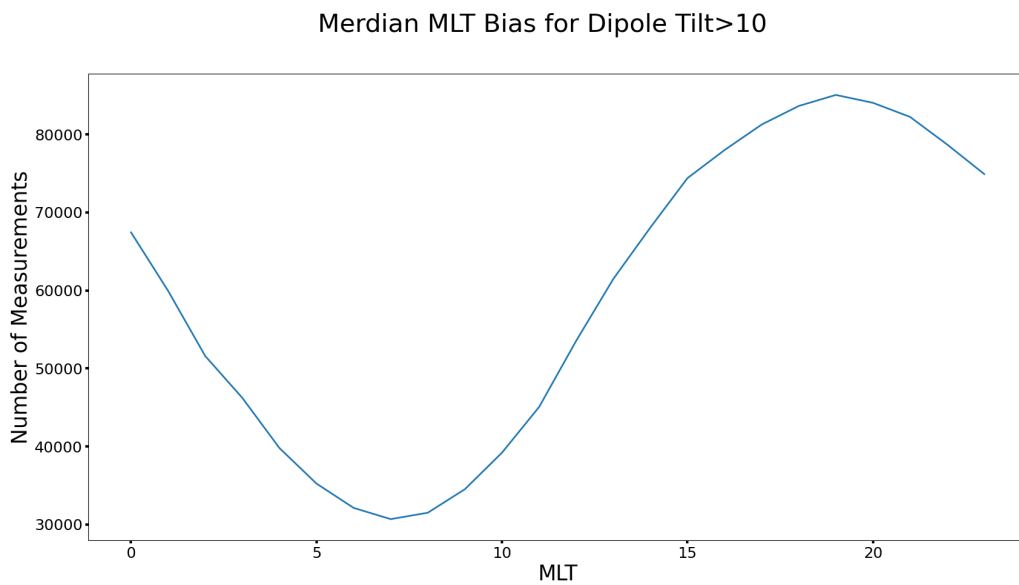
Figure 4.11: MLT bias in data for a dipole tilt angle greater than $10°$

Figure 4.10 and figure 4.11 show the amount of times the meridian is evaluated at each MLT when the dipole tilt angle is less than $-10°$ and greater than $10°$ respectively. It can be seen that for a dipole tilt of less than $-10°$ there is an increasing amount of data towards 7 MLT and a decreasing amount of data towards 18 MLT.

Chapter 5

IMF By and Seasonal Effects on Electrojet Properties

With the prior chapter presenting arguments for the validity of the SECS model and electrojet detection algorithm, the following chapter aims to present a statistical analysis of the electrojet profile along the $105°$ magnetic meridian. The analysis will in particular investigate the explicit B_y effect on divergence free currents in the northern polar ionosphere. It, wherever possible, ascribes the features and behaviours observed to known physical processes.

5.1 Primary Electrojet Explicit By Effect

The explicit B_y effect, introduced in section 2.4, is a change in the magnetosphere and ionosphere response to different polarities of IMF B_y. The most relevant for this study, is the work by *Holappa and Mursula* (2018) where it is shown, using the AL index, that the westward electrojet is suppressed in the northern hemisphere for B_y negative during the winter and shows a small suppression for B_y positive in the summer. Whereas, the AU index shows no explicit B_y effect. Results of the SECS model are first presented to show the explicit B_y effect on the properties of the electrojets and then later are discussed in order to apply a physical interpretation to the features present.

5.1.1 Results

In this section properties of the primary westward and eastward electrojets, evaluated from the electrojet detection outlined in section 3.8, are presented in a way that highlights the differences between the influence of B_y positive and negative in the summer and winter. Three electrojet properties; the width, peak amplitude and total current, are binned by the IMF B_y condition that corresponds to each data point and averaged. The seasons summer and winter are chosen by using data from May to July and November to January respectively.

The westward electrojet properties are presented first and can be used to draw comparisons between the explicit B_y effect on this more in depth analysis of the westward electrojet properties and the results found in *Holappa and Mursula* (2018). The total current through the electrojet is found by integrating the east-west sheet current den-

sity profiles, such as those seen in figure 3.12. This property can be considered a good measure of the overall strength of the electrojet.
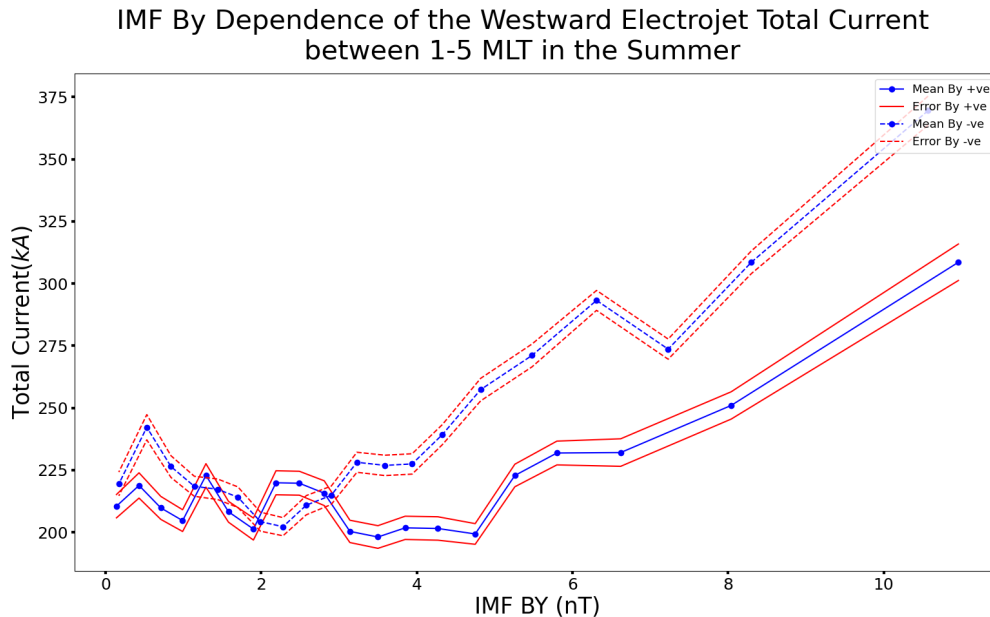
(a) Summer (May, June and July)
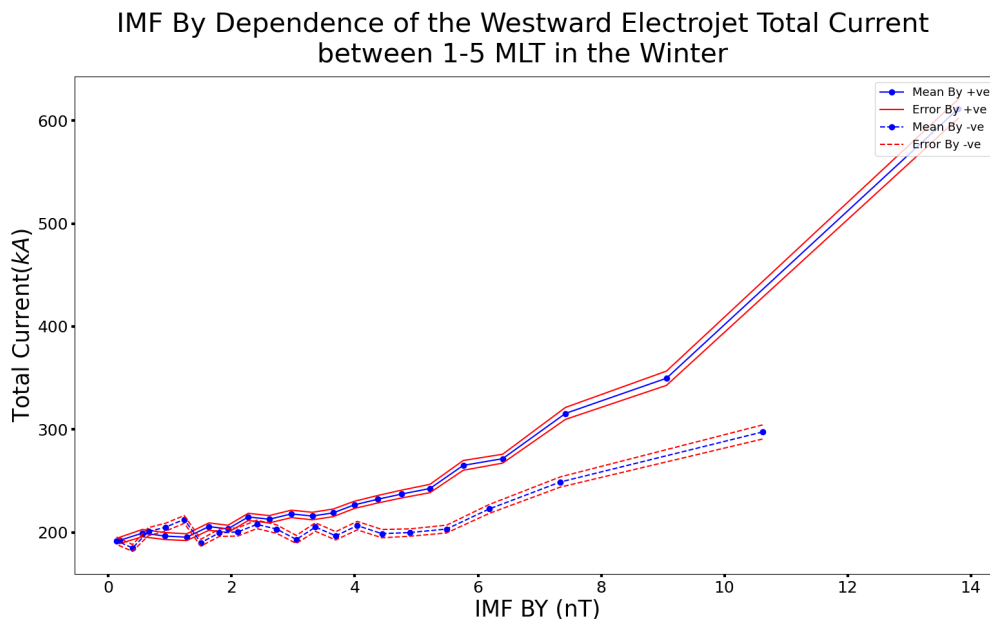
(b) Winter (November, December and January)

Figure 5.1: Binned averages of the total current through the primary westward electrojet between 1 and 5 MLT. Created using two sets of twenty quantile bins, one set for IMF $B_y > 0$ and one for the $B_y < 0$. The currents are placed in a particular set of bins and then subsequently one bin from that set, depending on the polarity and magnitude of B_y at the time of the data point as taken from the OMNI 1 minute averaged data set (King and Papitashvili, 2005) which time shifts the solar and IMF parameters to represent their progression to the bow shock

Figure 5.1 shows the average total current through the primary westward electrojet for different B_y polarity and magnitude. This is done using one minute averaged data

from OMNI (*King and Papitashvili*, 2005) which time shifts the solar and IMF parameters to represent their progression to the bow shock. The IMF B_y bins are defined by treating positive and negative polarities separately and using twenty quantiles for each, this ensures that there is the same amount of total current data in each bin. Figure 5.1a and b show the influence of B_y on the total current through the westward electrojet for the summer (May, June, July) and winter (November, December, January) respectively. Solid and dashed blue lines show the average current in the positive and negative B_y bins respectively. The red lines are plotted to show an envelop of the standard error of mean calculated in each bin around the averaged values. The peak sheet current density is the maximum east-west absolute sheet current density found in the electrojets profile. For the westward electrojet, this property is comparable to the AL index and is used as the selection criteria to define an electrojet out of the data product produced from the electrojet detection algorithm. After analysing the statistics of the algorithm's output and weak meridian profiles, a limit of 0.1 Am^-1 peak sheet current density is used to distinguish between reliable and unreliable electrojet information.

(a) Summer (May, June and July)

IMF By Dependence of the Westward Electrojet Peak
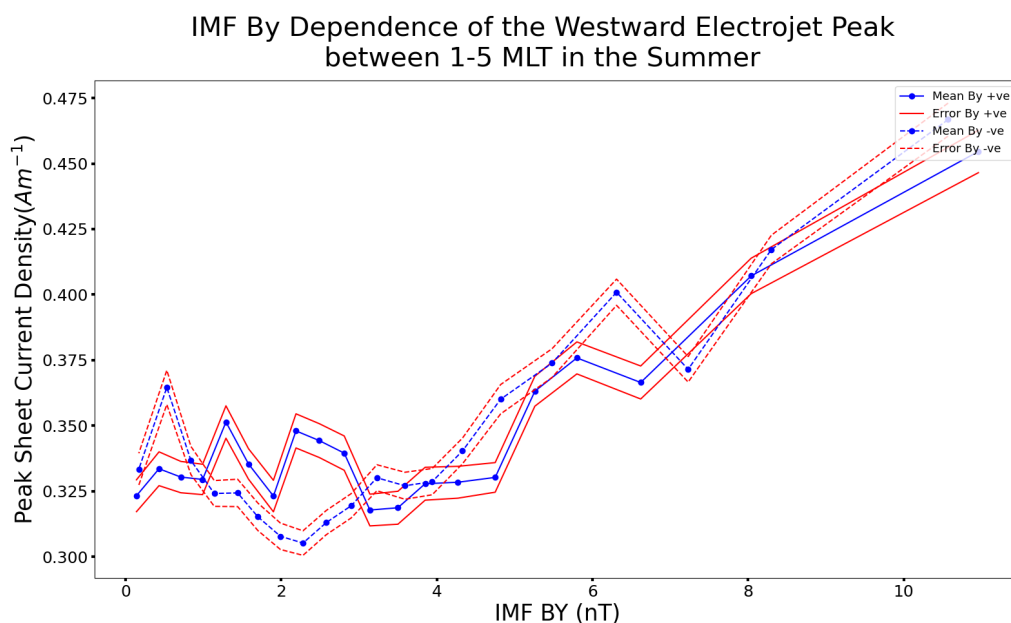between 1-5 MLT in the Winter

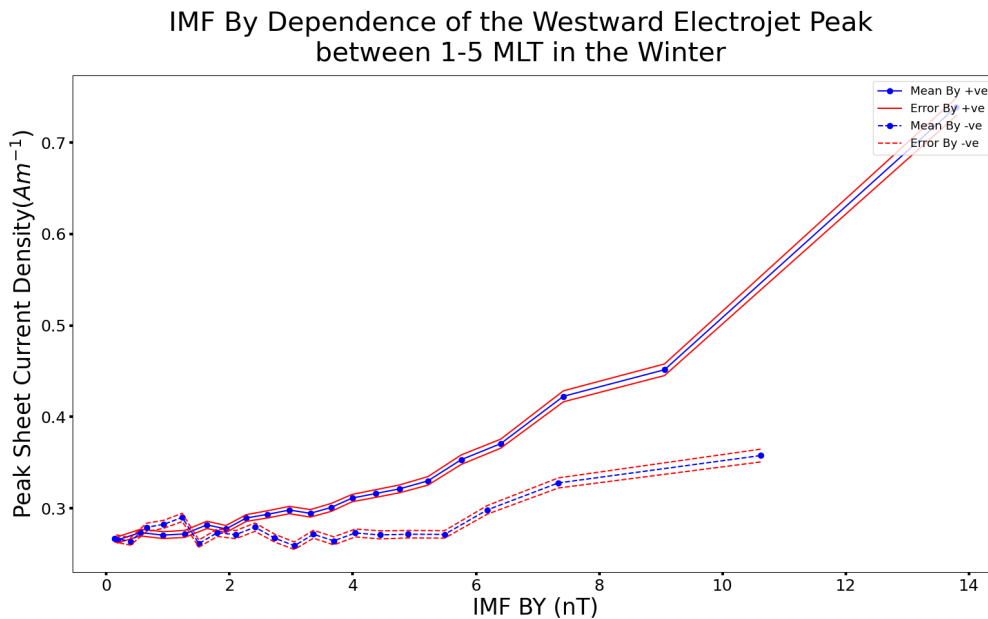*(b) Winter (November, December and January)*

Figure 5.2: Binned averages of the peak sheet current density of the primary westward electrojet between 1 and 5 MLT. Created using two sets of twenty quantile bins, one set for IMF $B_y > 0$ and one for the $B_y < 0$. The peaks are placed in a particular set of bins and then subsequently one bin from that set, depending on the polarity and magnitude of B_y at the time of the data point as taken from the OMNI 1 minute averaged data set (King and Papitashvili, 2005) which time shifts the solar and IMF parameters to represent their progression to the bow shock

Figure 5.2 shows the peak sheet current density of the primary westward electrojet profile for different B_y polarity and magnitude. The bins are defined in the same way as figure 5.1. Figure 5.2a and b show the influence of B_y on the peak sheet current density of the westward electrojet for the summer (May, June, July) and winter (November, December, January) respectively.

The last westward electrojet property presented is the width. This is found by finding the difference in the electrojet boundaries from the electrojet detection algorithm. This property gives an insight into the shape of the westward electrojet and the extent of its effects.

IMF By Dependence of the Westward Electrojet Width
between 1-5 MLT in the Summer

(a) Summer (May, June and July)

IMF By Dependence of the Westward Electrojet Width
between 1-5 MLT in the Winter

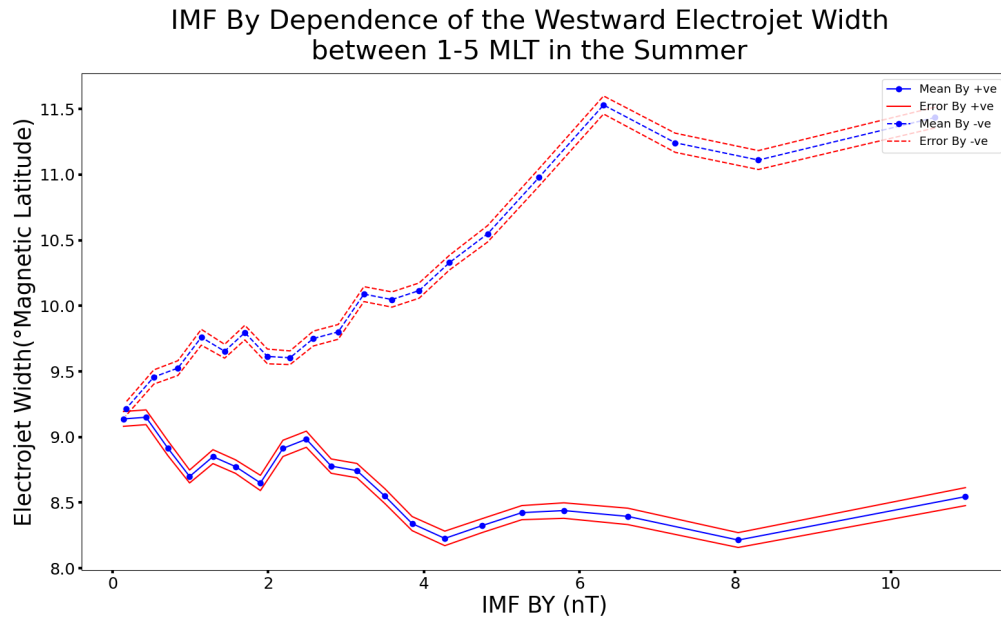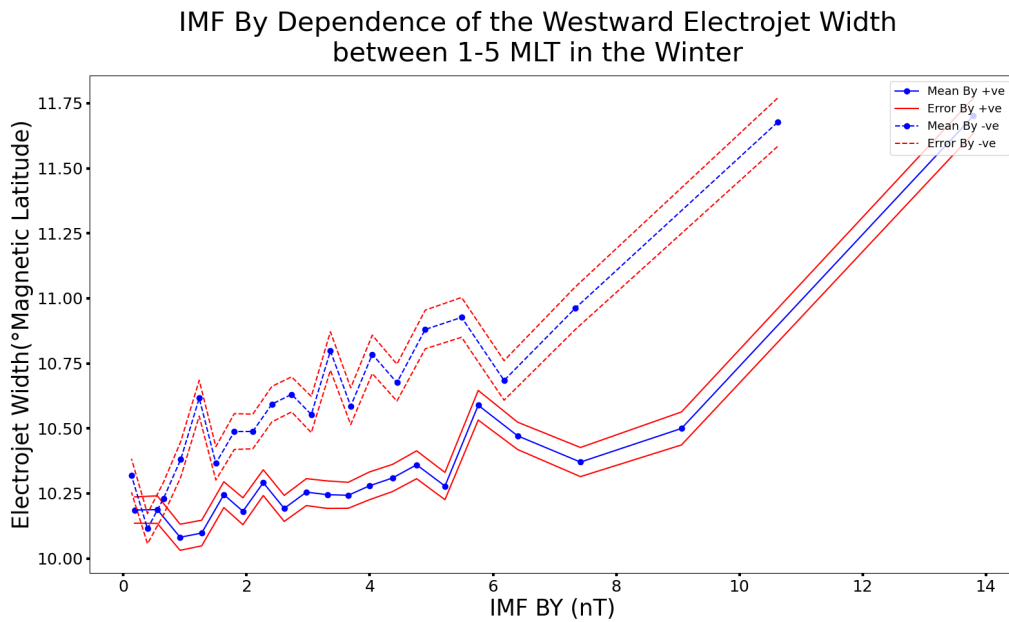*(b) Winter (November, December and January)*

Figure 5.3: Binned averages of the width of the primary westward electrojet between 1 and 5 MLT. Created using two sets of twenty quantile bins, one set for IMF $B_y > 0$ and one for the $B_y < 0$. The widths are placed in a particular set of bins and then subsequently one bin from that set, depending on the polarity and magnitude of B_y at the time of the data point as taken from the OMNI 1 minute averaged data set (King and Papitashvili, 2005) which time shifts the solar and IMF parameters to represent their progression to the bow shock

Figure 5.3 shows the widths of the primary westward electrojet for different B_y polarity and magnitude. The bins are defined in the same way as figure 5.1. Figure 5.3a and b show the influence of B_y on the width of the westward electrojet for the summer

(May, June, July) and winter (November, December, January) respectively.

      The eastward electrojet properties are presented next and can be used to show that there is in fact an explicit B_y effect in some properties of the eastward electrojet yet finding an agreement with the results found in *Holappa and Mursula* (2018), where there was no explicit B_y effect within the AU index. The total current through the eastward electrojet is found in the same way as the westward electrojet. It is a property that is a good indication of the strength of the eastward electrojet. A comparison with values for the westward electrojet can enable a view into the ionosphere dawn-dusk asymmetry due to the influence of night side magnetosphere processes.
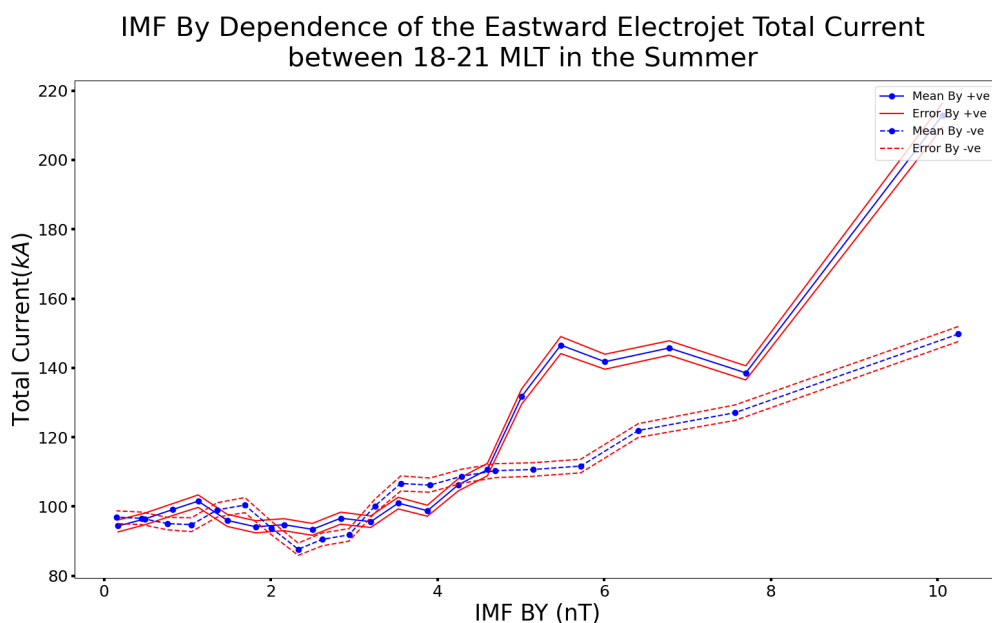
(a) Summer (May, June and July)

(b) Winter (November, December and January)

Figure 5.4: Binned averages of the total current through the primary eastward electrojet between 18 and 21 MLT. Created using two sets of twenty quantile bins, one set for IMF $B_y > 0$ and one for the $B_y < 0$. The currents are placed in a particular set of bins and then subsequently one bin from that set, depending on the polarity and magnitude of B_y at the time of the data point as taken from the OMNI 1 minute averaged data set (King and Papitashvili, 2005) which time shifts the solar and IMF parameters to represent their progression to the bow shock
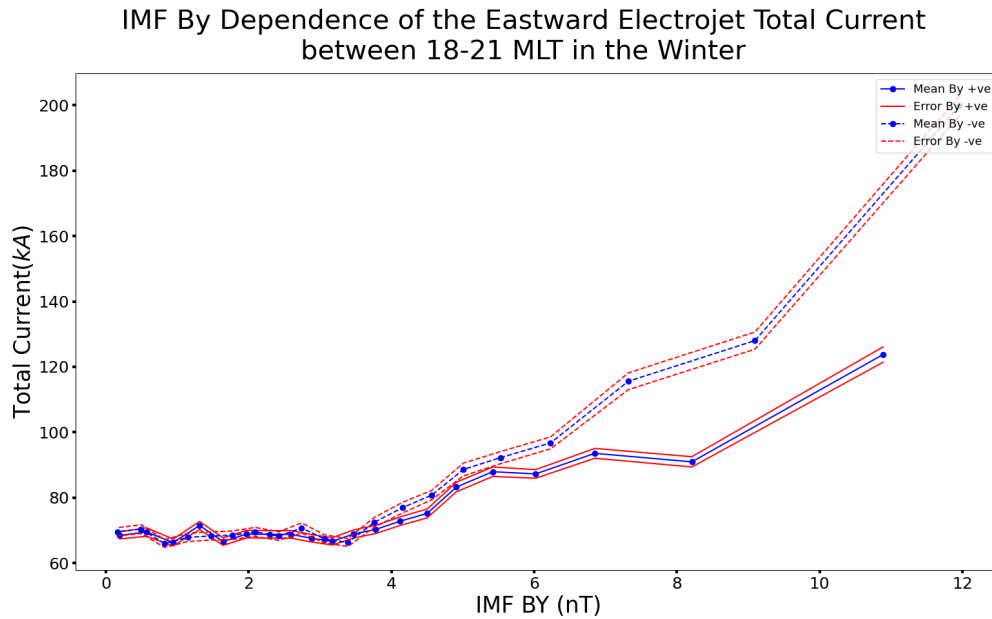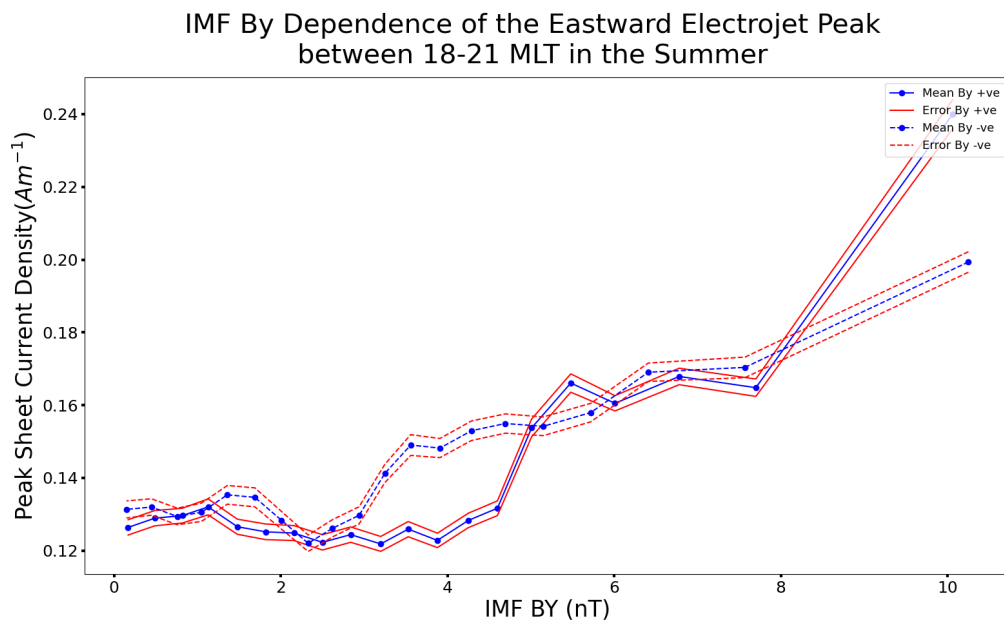
Figure 5.4 shows the average total current through the primary eastward electrojet for different B_y polarity and magnitude. This is done using one minute averaged data from OMNI (*King and Papitashvili*, 2005) which time shifts the solar and IMF parameters to represent their progression to the bow shock. The analysis is performed in the same way as is done fore the westward electrojet and the bins are defined in the same as figure 5.1. Figure 5.4a and b show the influence of B_y on the total current through the eastward electrojet for the summer (May, June, July) and winter (November, December, January) respectively. Solid and dashed blue lines show the average current in the positive and negative B_y bins respectively. The red lines are plotted to show an envelop of the standard error of mean calculated in each bin around the averaged values.

The peak sheet current density is the maximum east-west absolute sheet current density found in the electrojets profile. For the eastward electrojet, this property is comparable to the AU index and is used as the selection criteria to define an electrojet out of the data product produced from the electrojet detection algorithm. After analysing the statistics of the algorithm's output and weak meridian profiles, a limit of 0.05 $Am^{-}1$ peak sheet current density is used to distinguish between reliable and unreliable electrojet information.

IMF By Dependence of the Eastward Electrojet Peak
between 18-21 MLT in the Summer

(a) Summer (May, June and July)

IMF By Dependence of the Eastward Electrojet Peak
between 18-21 MLT in the Winter

(b) Winter (November, December and January)
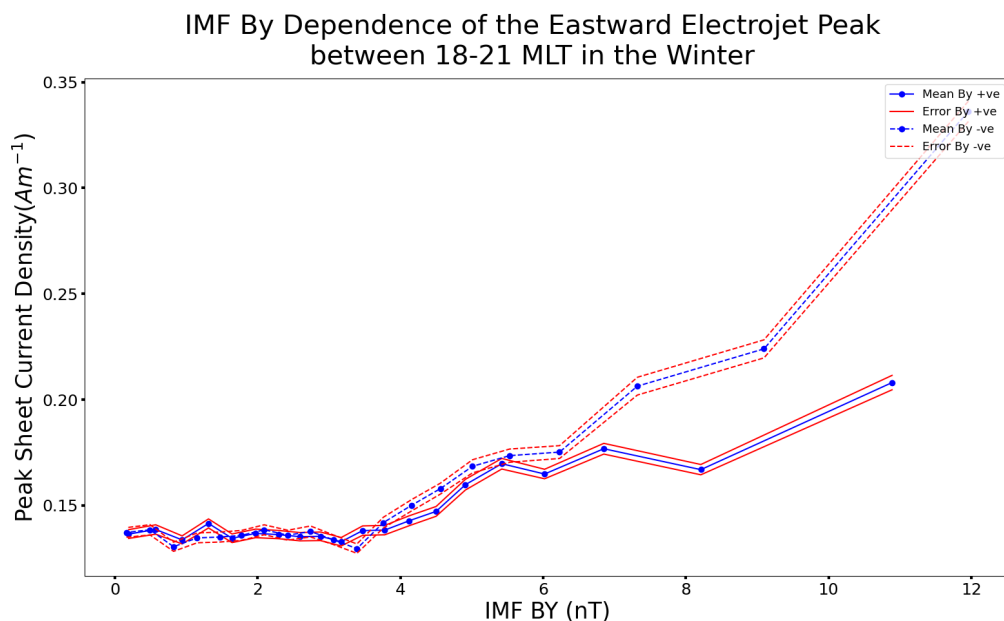
Figure 5.5: Binned averages of the peak sheet current density of the primary eastward electrojet be-
tween 18 and 21 MLT. Created using two sets of twenty quantile bins, one set for IMF $B_y > 0$ and one
for the $B_y < 0$. The peaks are placed in a particular set of bins and then subsequently one bin from
that set, depending on the polarity and magnitude of B_y at the time of the data point as taken from the
OMNI 1 minute averaged data set (King and Papitashvili, 2005) which time shifts the solar and IMF
parameters to represent their progression to the bow shock

Figure 5.5 shows the peak sheet current density of the primary eastward electrojet
profile for different B_y polarity and magnitude. The analysis is performed in the same
way as is done fore the westward electrojet and the bins are defined in the same as
figure 5.1. Figure 5.5a and b show the influence of B_y on the peak sheet current density
of the eastward electrojet for the summer (May, June, July) and winter (November,

December, January) respectively.

    The last eastward electrojet property presented is its width. This is found by finding the difference in the electrojet boundaries from the electrojet detection algorithm. This property gives an insight into the shape of the eastward electrojet and the extent of its effects. When combined with the values from the westward electrojet it allows a view into the structure and morphology and the night side ionosphere.
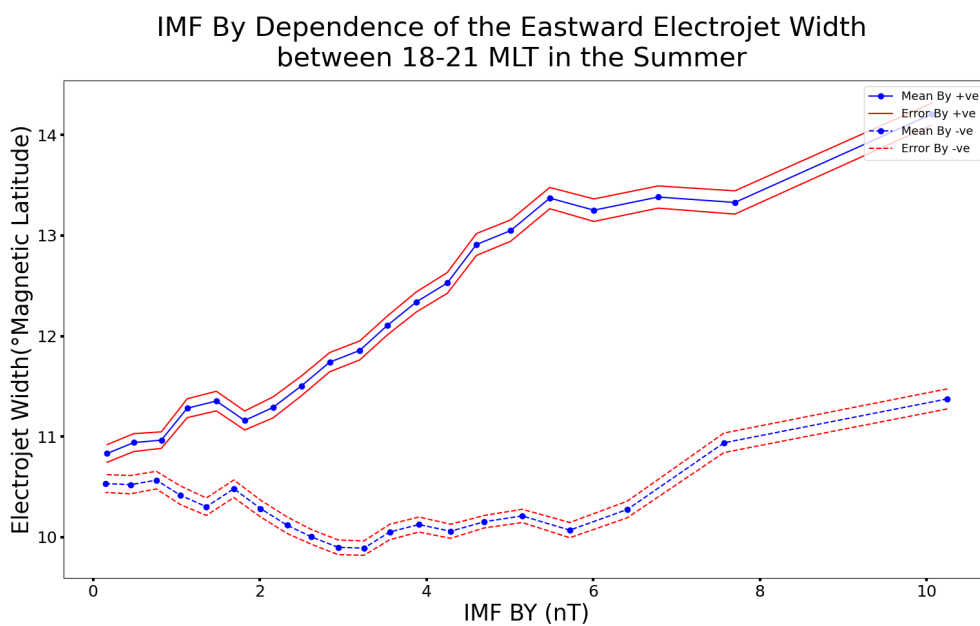

(a) Summer (May, June and July)

(b) Winter (November, December and January)

Figure 5.6: Binned averages of the width of the primary eastward electrojet between 18 and 21 MLT. Created using two sets of twenty quantile bins, one set for IMF $B_y > 0$ and one for the $B_y < 0$. The widths are placed in a particular set of bins and then subsequently one bin from that set, depending on the polarity and magnitude of B_y at the time of the data point as taken from the OMNI 1 minute averaged data set (King and Papitashvili, 2005) which time shifts the solar and IMF parameters to represent their progression to the bow shock
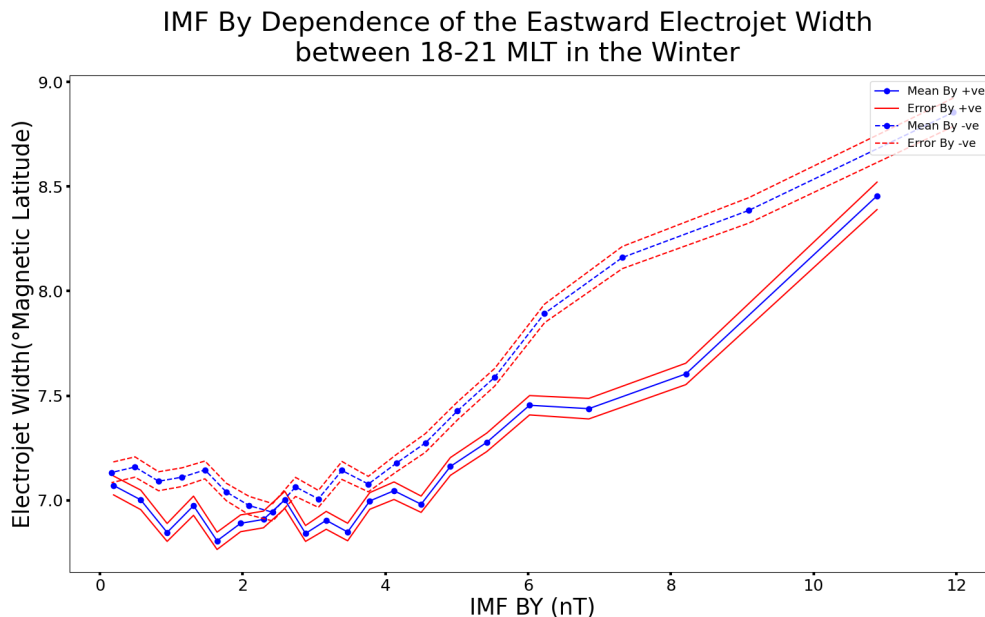
Figure 5.6 shows the widths of the primary eastward electrojet for different B_y polarity and magnitude. The analysis is performed in the same way as is done fore the westward electrojet and the bins are defined in the same as figure 5.1. Figure 5.6a and b show the influence of B_y on the width of the eastward electrojet for the summer (May, June, July) and winter (November, December, January) respectively.

5.1.2   Discussion

This section discusses the results presented in section 5.1.1 and begins by verifying the explicit B_y effect on the electrojets that is seen in previous studies. It goes on to use the unique data set of electrojet properties to investigate the explicit B_y effect further and attempts to attribute the trends seen to physical processes within the ionosphere and magnetosphere.

The peak value of the westward electrojet, figure 5.2, is by its nature, comparable to the AL index. *Holappa and Mursula* (2018) showed that the AL index is suppressed significantly during the winter when B_y is negative and less clearly when B_y is positive during the summer. Therefore, it is expected that the peak sheet current density of the primary westward electrojet would exhibit these same trends. It is clear that during the winter, when the magnitude of B_y is greater than $2nT$, there is an explicit B_y effect on the peak sheet current density. The average peak is shown to be much larger for positive B_y than negative B_y. However, during the summer there is no clear trend that shows an explicit B_y effect on the peak sheet current density of the primary westward electrojet.

Holappa and Mursula (2018) doesn't find a large effect during the summer and it could be a possibility that either the peak doesn't show exactly what the AL index does or it could be because of the irregular data coverage in the summer months, as seen in figure 4.6. Although the investigation of the peak value of the westward electrojet doesn't add to the current knowledge on the explicit B_y effect, it does confirm observations using a new data product.

The total current through the westward electrojet, figure 5.1, is not comparable to previous studies as it can only be found by resolving the entire sheet current density profile of the electrojet. In both the summer and winter, the strength of the primary westward electrojet shows an explicit B_y effect similar to what *Holappa and Mursula* (2018) observed in the AL index. During the winter the westward electrojet is stronger when B_y is positive and when B_y is negative during the summer. The next step is to explain what mechanism is making the strength of the westward electrojet have an explicit B_y effect during the summer when there is none observable in the peaks of the westward electrojet. By analysing the width of the westward electrojet, the controlling property that introduces an explicit B_y effect into the strength of the westward electrojet can be found, figure 5.3. During the winter there is small preference for wider primary westward electrojet when B_y is negative. This insignificant width difference has little effect on the electrojet strength. The B_y influence on the widths is in opposition to what is seen in the total current through the westward electrojet. It can be concluded that during the winter the explicit B_y effect on the strength of the westward electrojet is controlled by how the peak of the westward electrojet changes due to different polarities of B_y. In the summer however, there is a large B_y effect on the width of the primary westward electrojet. With little to no effect seen in the peak of the westward electrojet, it can be concluded that during the summer the explicit B_y effect on width of the westward electrojet imposes the signatures seen in its strength.

Before investigating the physical processes that drive the observations seen in the westward electrojet, it is important to analyse the eastward electrojet to understand dusk side ionosphere dynamics and then find the driving the mechanisms for the explicit B_y effect.

The peak value of the primary eastward electrojet, figure 5.5, is comparable to the AU index. *Holappa and Mursula* (2018) found no clear explicit B_y effect in the AU index, and differences during the equinoxes were ascribed to the Russell McPherron effect (*Russell and McPherron*, 1973). During the winter there is a small explicit B_y effect on the peak of the primary eastward electrojet at large magnitudes of B_y. The peak is higher for B_y negative than B_y positive when B_y is greater than $6nT$. This is not something observed by *Holappa and Mursula* (2018) in the AU index, however they did not investigate the influence of both the magnitude and polarity of B_y on the AU index. During the summer there is no clear explicit B_y effect on the peak of the primary eastward electrojet, agreeing the AU investigation by *Holappa and Mursula* (2018).

The total current through the eastward electrojet, figure 5.4, is also not comparable to previous studies as it is only made possible by resolving the eastward electrojet's sheet current density profile. When the magnitude of B_y is less than $5nT$, there is not an explicit B_y effect in the strength of the primary eastward electrojet. However for stronger magnitudes of B_y, there is an explicit B_y effect on the strength of the primary eastward electrojet in both the summer and winter. During the winter B_y negative creates a larger current through the primary eastward electrojet and during the summer B_y

positive does the same. Similar to the westward the electrojet, the widths of the primary eastward electrojet, figure 5.6, show an insignificant explicit B_y effect during the winter and it can be seen that the explicit B_y effect in the strength of eastward electrojet when the magnitude of B_y is large is driven by the effects in the peak sheet current density of the westward electrojet. However, during the summer there is a large explicit B_y effect on the width of the primary eastward electrojet for all magnitudes of B_y. The eastward electrojet is much wider when B_y is positive than negative. However, the total current through the primary eastward electrojet doesn't show this signature and the peak of the eastward electrojet doesn't show anything that counters the effect from the widths.

With an explicit B_y effect during the summer on both the eastward and westward electrojet, with the eastward also not showing a change in its strength, an analysis of the average electrojet profile for the eastward and westward electrojet and during the summer and winter may help to understand the dynamics in play.

Figure 5.7: Average sheet current density profile during the winter and summer for the westward electrojet between 1 and 5 MLT

Average Eastward Current between 1-5 MLT
in the Summer

(a) Summer (May, June and July)

Average Eastward Current between 1-5 MLT
in the Winter
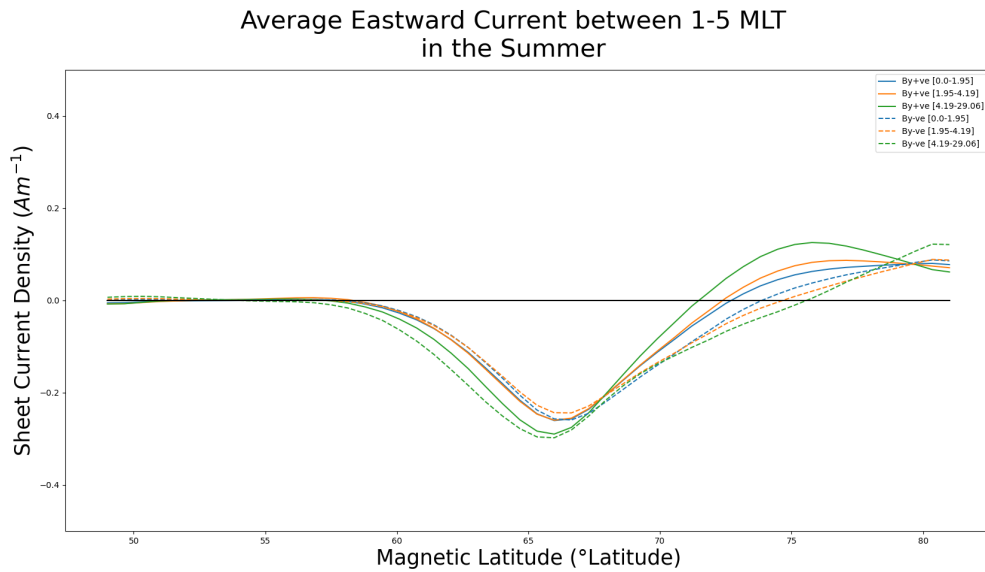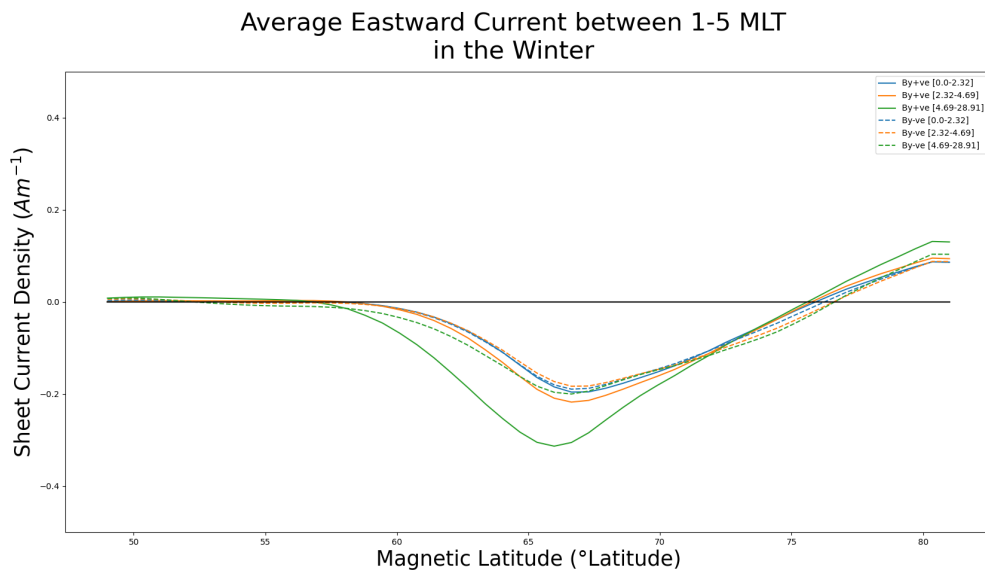
(b) Winter (November, December and January)

Figure 5.7 shows the average of the westward electrojet sheet current density profiles, that contribute to the westward electrojet properties presented in section 5.1.1, in the summer and winter for different B_y polarity and magnitude. This is done using one minute averaged data from OMNI (*King and Papitashvili*, 2005) which time shifts the solar and IMF parameters to represent their progression to the bow shock. In these plots it can be seen clearly that the explicit B_y effect on widths of the westward electrojet during the summer is due to an explicit B_y effect on the westward electrojets poleward boundary. In both seasons the equatorward boundary shows some variation due to changes in the magnitude of B_y but, the poleward boundary varies little during the winter and largely during the summer. During the summer the poleward boundary

is shifted closer to the equator for B_y positive and increasing magnitude. B_y negative shifts the poleward boundary closer to the pole for increasing B_y magnitude. The explicit B_y effect on the poleward boundary of the westward electrojet during the summer appears to explain the explicit B_y effect seen in the width of the westward electrojet and, subsequently, the total current through the westward electrojet.

The next step is to analyse the average eastward electrojet profiles to see if there is a similar behaviour that can explain the seasonal explicit B_y effect on the eastward electrojet width.

Figure 5.8: Average sheet current density profile during the winter and summer for the eastward electrojet between 18 and 21 MLT
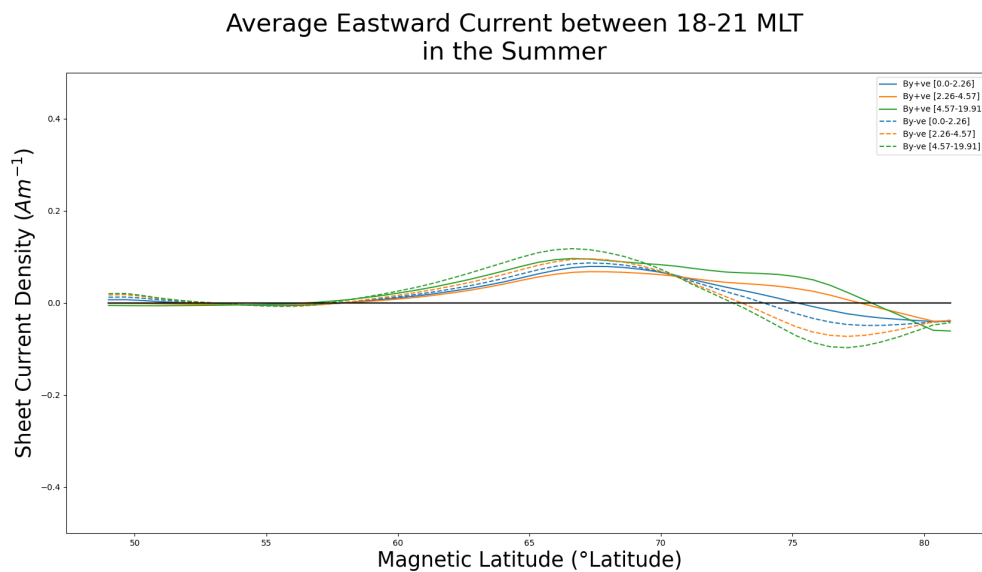

(a) Summer (May, June and July)
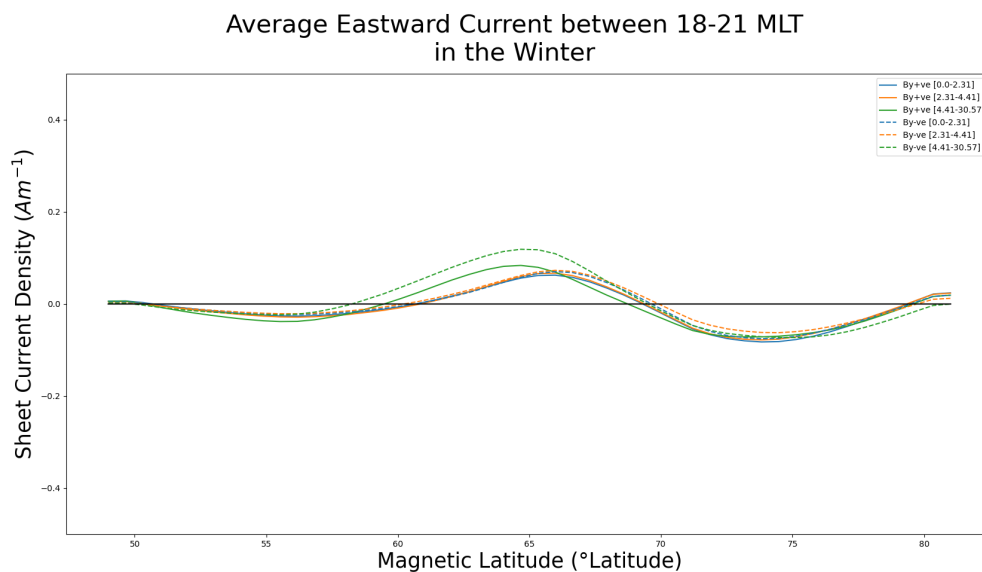
(b) Winter (November, December and January)

Figure 5.8 shows the average eastward electrojet sheet current density profile in the

summer and winter for different B_y polarity and magnitude. This is done using one minute averaged data from OMNI (*King and Papitashvili*, 2005) which time shifts the solar and IMF parameters to represent their progression to the bow shock. Similar to the westward, the equatorward boundary of the eastward electrojet shows some variation in the summer and winter due to the magnitude of B_y and the poleward boundary shows very little variation during the winter. However, during the summer the poleward boundary of the eastward electrojet is shifted equatorward for a negative B_y and increasing magnitude. Positive B_y shifts the poleward boundary of the eastward electrojet towards to the pole as the magnitude of B_y increases. This once again explains the explicit B_y effect observed in the widths of the primary eastward electrojet and the total current through the eastward electrojet, when the magnitude of B_y is greater than $5nT$.

Explanations for the parallel nature of the equatorward boundary of the eastward and westward electrojet for the polarity of B_y suggest that it is related to the strength of dayside opening of magnetic flux. In the IMF, stronger B_y is often correlated with stronger dayside coupling and as such this increases the amount of opened magnetic field lines on the dayside and, after convection across the polar cap, creates an expanded auroral oval due to processes in the magnetotail. This subsequently manifests as a more equatorward electrojet boundary.

The explicit B_y effect on the poleward boundary of the westward and eastward electrojets during the summer and not the winter needs further investigation. As discussed in the section 2.2, the two largest influences on the strength and structure of the electrojets is the ionospheric conductance, Hall and Pedersen, and ionospheric convection. During the northern hemisphere summer there is a positive dipole tilt and higher conductance in the northern ionosphere, due to an increase in solar irradiance. The change in dipole tilt can effect the typical dayside IMF-magnetosphere coupling and, consequently, ionospheric convection. During the summer the divergence free current is much closer to resembling the Hall currents across the entire polar ionosphere, as such changes in the Hall conductance in the summer compared to winter can have a large impact on the electrojets. However, it is not clear how the explicit B_y effect in particle precipitation, found by *Holappa et al.* (2020b), would change the conductance in a way that causes the observations seen in the poleward boundary of the electrojets.

Pettigrew et al. (2010) performed a statistical study on ionospheric convection in the northern and southern hemisphere for B_y positive and B_y negative and for positive, negative and neutral dipole tilt angles.
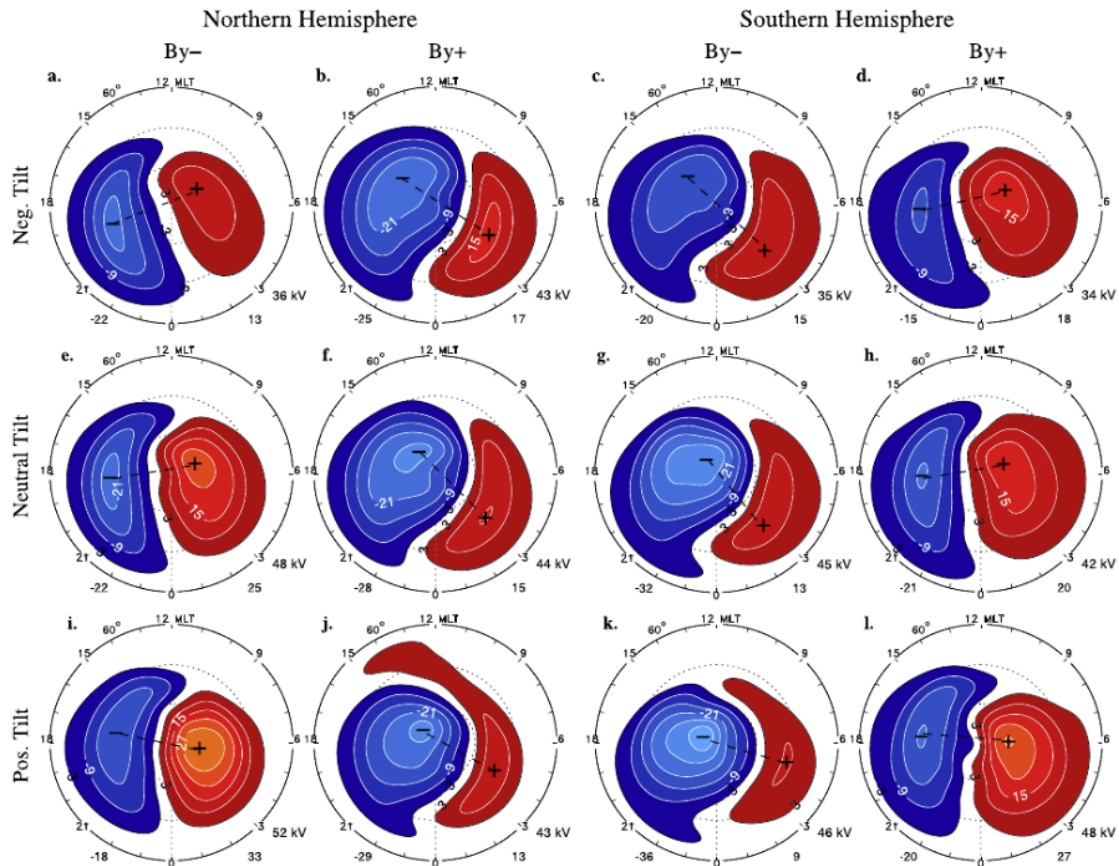
Figure 5.9: Statistical convection patterns sorted by tilt. IMF By+/, 5 nT < BT< 10 nT, taken from Pettigrew et al. (2010)

Figure 5.9 shows what *Pettigrew et al.* (2010) found. Looking at the positive dipole tilt plots in the northern hemisphere, which is the typical condition during the summer, it can be seen that the convection cell associated with the westward electrojet, in red in figure 5.9, is small and contracted for B_y positive and large and rounded during B negative. This large difference in the convection cells is not seen for a negative dipole tilt in the northern hemisphere, the typical condition during the winter. This suggests that for the westward electrojet the poleward boundary is dependent on the changes observed in the statistical ionospheric convection cells with different polarities of B_y. There is a similar effect on the convection cell associated with the eastward electrojet, in blue in figure 5.9. This leads to a conclusion that narrower, contracted ionospheric convection cells lead to lower poleward boundaries of the electrojets and the reverse can be said for the larger, rounded convection cells. This brings us one step closer to finding the mechanisms behind the summer explicit B_y effect on the poleward boundary of the electrojets. Signatures in the ionospheric convection suggest that there is a mechanism within the dayside IMF-magnetosphere coupling that is changing the convection path of the magnetic field lines. *Reistad et al.* (2019) noticed a similar behaviour when looking at the polar cap electric field. After further investigation they identified that lobe reconnection was causing different convection cells and, consequently, altering the statistics of the ionospheric convection during the summer. Lobe reconnection is a coupling of the IMF with magnetic field lines within the magnetolobes. It is known to occur more frequently when B_z is positive and when the dipole tilt angle is towards the

Sun (*Crooker and Rich*, 1993; *Frey et al.*, 2004b; *Koustov et al.*, 2017; *Østgaard et al.*, 2018; *Reistad et al.*, 2019; *Wilder et al.*, 2010; *Yakymenko et al.*, 2018). It is important to visualise how lobe reconnection driven cells and Dungey cycle driven cells interact in order to see if they can be used to explain the summer B_y effect on electrojet width.
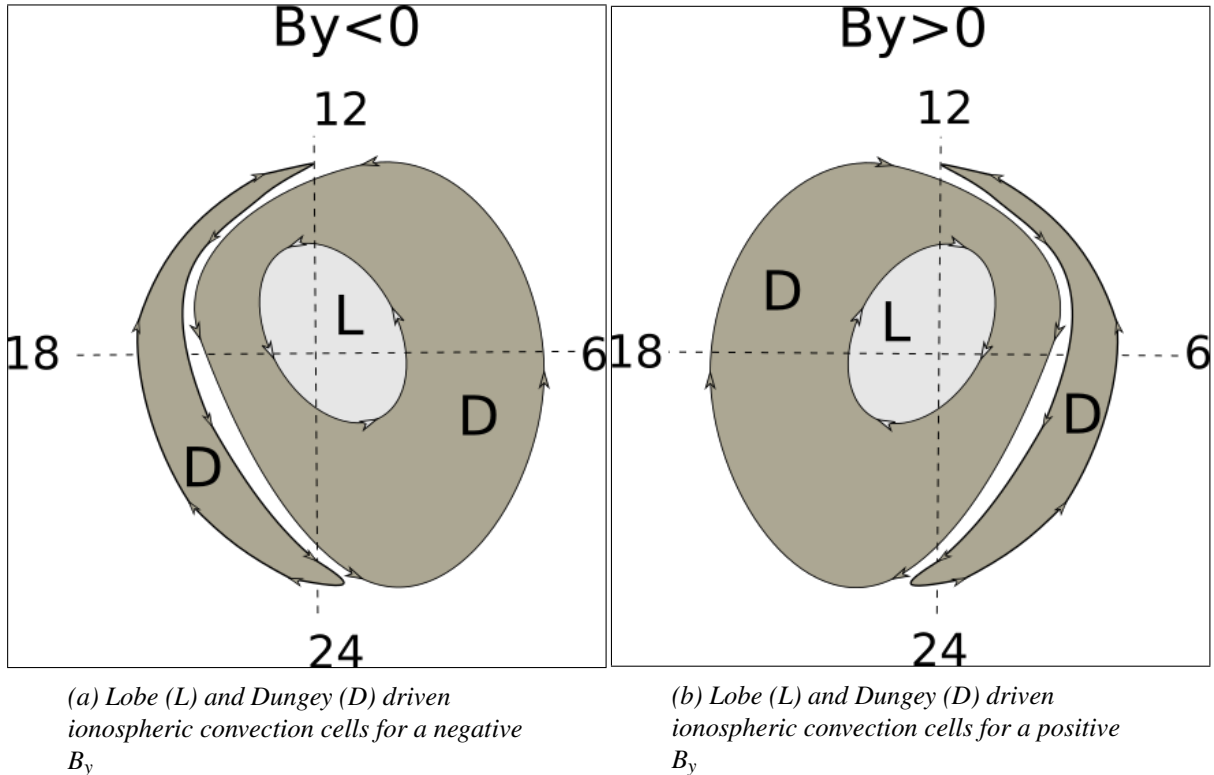

(a) Lobe (L) and Dungey (D) driven ionospheric convection cells for a negative B_y

(b) Lobe (L) and Dungey (D) driven ionospheric convection cells for a positive B_y

Figure 5.10: Conceptual illustration of Lobe (L) and Dungey (D) driven ionospheric convection cells for a negative B_y (left) and a positive B_y (right)

Figure 5.10 is a simple diagram designed to show the lobe and Dungey cells under positive and negative B_y during northern hemisphere summer. The superposition of these cells will give the overall convection in the polar ionosphere and the divergence free current that makes up the electrojets will be in opposition of the direction ionospheric convection and scaled by its magnitude. When B_y is negative, the lobe cell creates more current in the direction of the westward electrojet at high latitudes. The electrojet detection algorithm then finds the poleward boundary of westward electrojet at higher latitudes. When B_y is positive, the westward electrojet only lies on a contracted Dungey cell and therefore poleward boundary is shifted towards the equator and dependent on the location of the reversal of ionospheric convection direction within the duskside Dungey cell. This effect is the same for the eastward electrojet. When B_y is positive the lobe cell is on the side of the eastward electrojet and therefore the algorithm finds a more poleward boundary for the eastward electrojet. When B_y is negative the convection cell on the dusk side is just a contracted Dungey cell and the algorithm finds the poleward boundary to be more equatorward.

Through a rigorous investigation it has now been shown that the explicit B_y effect in the summer on the width of the primary eastward and westward electrojet is due to a shift in the poleward boundary of the electrojets driven by lobe reconnection. It is also clear that the polarity of B_y is an important factor in the coupling of the IMF with the

magnetolobe and the convection of those field lines.

5.2 Multiple Electrojets

The electrojet detection algorithm, described in 3.8, finds the properties of up to three westward and three eastward electrojets within each eastward sheet current density profile along the profile. Within this section the probability of detecting multiple electrojets is used to investigate the B_y effect on the disruption of the auroral electrojets. Results that show the multiple electrojet probability for different seasons and B_y polarity are introduced and later the mechanisms that create the trends seen are discussed.

5.2.1 Results

In this section the probability of detecting multiple electrojets along a meridian is presented with the goal of understanding the mechanisms that cause a disruption to the eastward and westward electrojet and how season and the polarity of B_y can affect the location where the disruption is most common.

The probability of detecting multiple electrojets is depicted in a polar plot to show the MLT location with the highest probability. This is performed after first separating the data set by season, summer and winter, and then by the polarity of B_y at the time of the meridian. One minute averaged data from OMNI (*King and Papitashvili*, 2005), which time shifts the solar and IMF parameters to represent their progression to the bow shock, is used for the B_y condition at the time of the meridian. The occurrence of two or more electrojets is then binned by its MLT location, where the bins are of size 0.5. The same binning is then performed on the availability of the meridian properties for each season and B_y condition. Subsequently, the bins containing the occurrence of multiple electrojet can be normalised by the availability of meridian properties, thus returning the probability of detecting multiple electrojets in each MLT bin.

During the summer the conductance is known be higher and more uniform in the polar ionosphere. Therefore, the electrojets are less structured and more impervious to disruption.
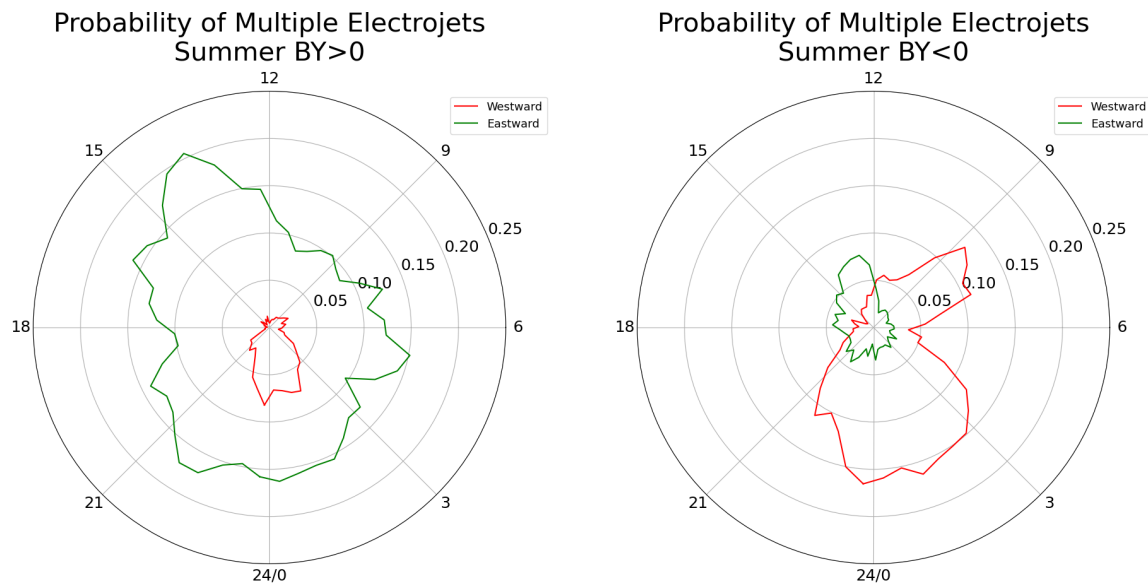
(a) Summer (May, June and July) and By>0   (b) Summer (May, June and July) and By<0

Figure 5.11: Polar plots showing the probability of multiple electrojets during the summer (May, June, and July) for positive and negative B_y conditions. The radial component of each plot shows the probability of detecting multiple electrojets in bins of 0.5 MLT. The probabilities are calculated by normalising the occurrence of two or more electrojets by the availability of meridian properties evaluated using the model

Figure 5.11 shows the probability of two or more electrojets being detected along the meridian in bins of 0.5 MLT for positive and negative B_y conditions and during the summer. The filtering by B_y condition is done using the one minute averaged data from OMNI (*King and Papitashvili*, 2005), which time shifts the solar and IMF parameters to represent their progression to the bow shock, at the time of the each data point. The probabilities are shown as the radial component of the plots and are calculated by normalising the MLT bins containing the occurrence of two or more electrojets by the occurrence of meridian evaluation within those bins.

In the northern hemisphere the occurrence of substorms during the winter is much greater. During the winter the conductance is lower and particle precipitation makes it less uniform and more structured. Consequently, there is an expectation that the disruption of the electrojets is increased overall with particular significance at MLTs close to the Harang discontinuity where substorm onsets are most common. Figure 5.12 shows the probability of two or more electrojets being detected along the meridian in bins of 0.5 MLT for positive and negative B_y conditions and during the winter. The filtering by B_y condition is done using the one minute averaged data from OMNI (*King and Papitashvili*, 2005), which time shifts the solar and IMF parameters to represent their progression to the bow shock, at the time of the each data point. The probabilities are shown as the radial component of the plots and are calculated by normalising the MLT bins containing the occurrence of two or more electrojets by the occurrence of meridian evaluation within those bins.
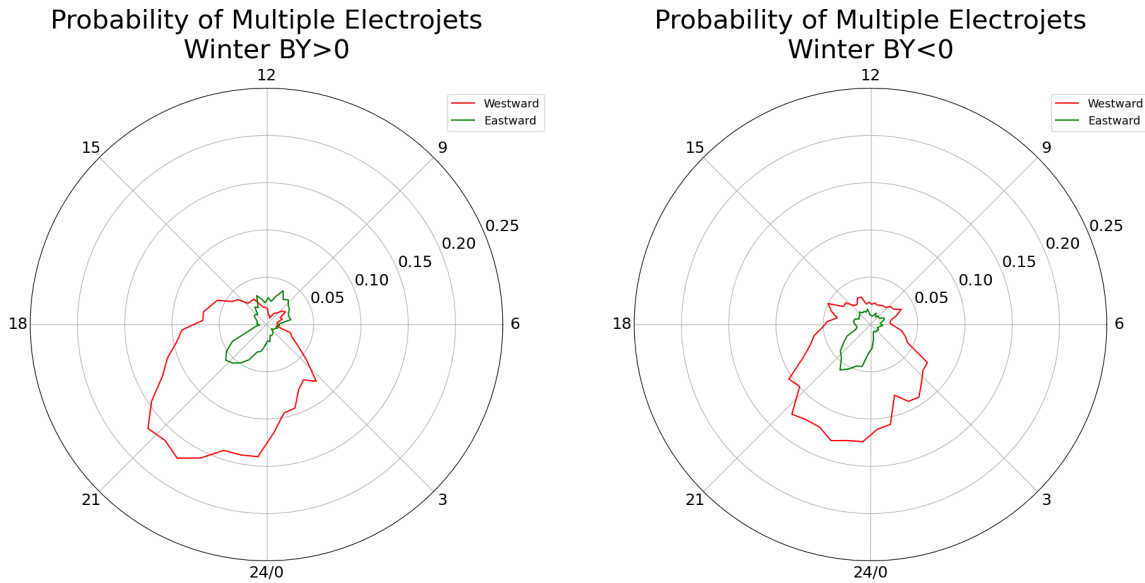
(a) Winter (November, December and January) and By>0

(b) Winter (November, December and January) and By<0

Figure 5.12: Polar plots showing the probability of multiple electrojets during the winter (November, December and January) for positive and negative B_y conditions. The radial component of each plot shows the probability of detecting multiple electrojets in bins of 0.5 MLT. The probabilities are calculated by normalising the occurrence of two or more electrojets by the availability of meridian properties evaluated using the model

5.2.2   Discussion

This section discusses the results introduced in section 5.2.1, attempting to find the underlying processes that drive the disruption of the electrojets and the B_y effect on those processes.

    The disruption of the electrojets during the winter, figure 5.12, is more prominent in pre midnight MLT sector which is the region of the Harang discontinuity and where substorm onsets occur most frequently. This supports the hypothesis that during the winter electrojet disruption is caused by substorm onsets. It is unclear as to why during the winter it is more likely to see multiple westward electrojets than eastward electrojets, however, it may be related to westward electrojets being typically stronger than eastward electrojets. The winter exhibits a B_y effect in the location where multiple electrojets are most probable for both the eastward and westward electrojet. A positive B_y shifts the location of most common disruption towards earlier MLTs, while a negative B_y shifts it towards midnight. This suggests that there is a change in the MLT location of the Harang discontinuity and, consequently, the most common MLT of substorm onsets. *Ostgaard et al.* (2011) investigated the effect of IMF clock angle on the location of substorm onsets. This can be compared to the B_y dependence of electrojet disruption.
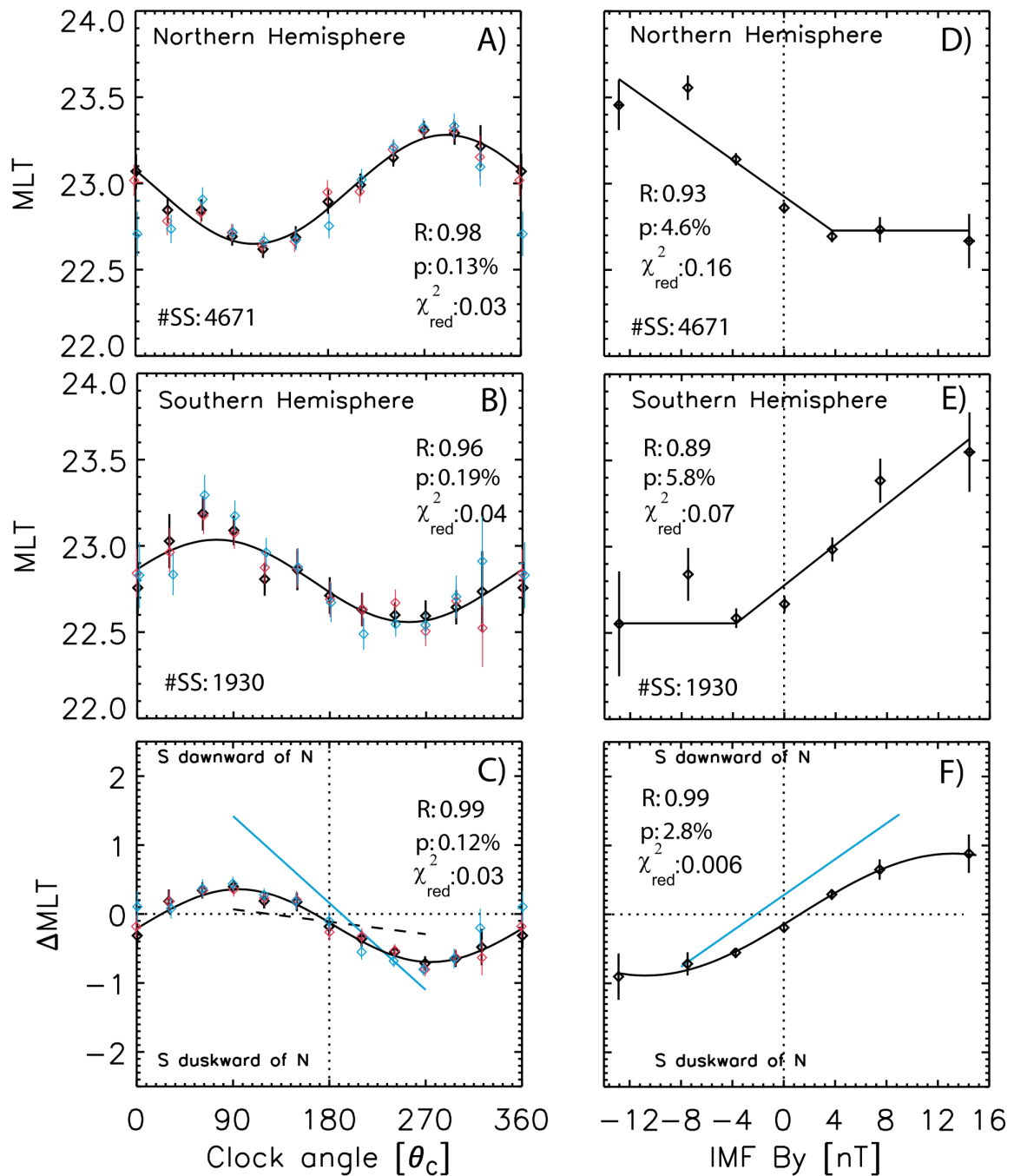
Figure 5.13: Substorm onset location statistics due to a changing IMF clock angle. Taken from Ost-gaard et al. (2011)

Figure 5.13 is taken from *Ostgaard et al.* (2011) and shows MLT location of sub-storm onsets in the northern and southern hemisphere for different IMF clock angles. Figure 5.13 A) shows the MLT location of substorm onsets for the northern hemisphere and can be compared with the most probable location of multiple electrojets in figure 5.11 and 5.12. A clock angle of 90° (270°) is where the IMF is orientated to be purely in the positive (negative) *y* direction in the *y-z* plane. Clock angles close to 90° (270°) in figure 5.13 can be compared with the most probable location of multiple electrojets when B_y is positive (negative). At clock angles close to 90° the MLT location of sub-storm onsets tends towards lower MLTs, which is the same trend observed in the most

probable location of multiple electrojets during the winter. At clock angles close to 270° the MLT location of substorm onsets is shifted towards magnetic midnight. This is once again the same trend observed in the most probable location of multiple electrojets during the winter. *Ostgaard et al.* (2011) confirms that the B_y effect on the MLT location of electrojet disruption during the winter is the same that is seen on substorm onsets.

The summer trends in the electrojet disruption, figure 5.11, do not show such a clear pattern. In the summer the electrojets are expected to be structured and more impervious to disruption, but the probability of disruption should still be higher in the region of the Harang discontinuity, the pre midnight MLT sector. For B_y positive the probability of finding multiple westward electrojets is greatly reduced. There is an opposite effect on the probability of multiple eastward electrojets, they are much larger at all MLTs than any of the other plots. The most probable location for multiple eastward electrojets is between 14 and 15 MLT and it is not significantly prominent in comparison to other MLT sectors. When B_y is negative the peak probability of multiple westward electrojets returns to values comparable to the winter, however there is an extra peak close to 9 MLT and the multiple eastward electrojet probabilities peak close to 13 MLT. In the summer it is clear that multiple electrojets is not well correlated with substorm onsets and that other processes are affecting the eastward sheet current densities resulting in electrojet disruption at different MLTs.

Chapter 6

Summary

This chapter discusses how the goals of this study have been addressed, summarises how the methodology used in this study was reached and the conclusion drawn from the electrojet properties that the model and electrojet detection algorithm found.

6.1   Methodology

This section outlines the core concepts and developments that have been made to create the SECS model used in this study.

Chapter 3 takes the reader through the steps taken to create the robust and optimised model used for this study. Firstly the concept of SECS is introduced and it demonstrated how the superposition of spherical elementary current systems can be used to describe a divergence free and curl free current system, with a different set up of equations for the two systems. Next it is shown that magnetometer measurements can be used to constrain SECS allowing it create a representation of the currents within the ionosphere. However, ground magnetic field measurements only give a view into the divergence free ionospheric currents. Two methods are introduced that can improve the physicality of the divergence free currents evaluated using the SECS model. Truncated SVD is most often used with SECS to improve it, one of its advantages is the simplicity in its implementation. However, recent work in *Laundal et al.* (2020), introduced regularisation as a better why to optimise the SECS model. This regularisation technique allows knowledge on the gradients in the currents to be applied to model and produces a much more physical result than the with truncated SVD whilst not straying too far from the information provided from the magnetometer data.

Telluric currents, introduced in section 2.3, are a problem for ground magnetic field measurements. This is because the magnetometers measure the superposition of the magnetic field from the telluric currents in the ground and the ionospheric currents. If a SECS model uses the magnetometer data without adjusting for telluric currents the divergence free currents evaluated will not be representative of those in the ionosphere. The image current technique, outlined in *Juusola et al.* (2016), and telluric SEC poles, an idea introduced in *Pulkkinen et al.* (2003b), are two methods discussed to adjust the SECS model for the influence of telluric currents. The image current technique applies an assumption between the relationship of the ionospheric currents and telluric currents, while the telluric SEC poles only make assumptions about the depth of the

telluric currents. After testing and investigation the image current technique is found to be effective, computationally efficient and does not increase model complexity significantly. It is therefore used in the model for this study. The final key component of the SECS model used in this study is the choice of the SEC pole locations. This study chose to use a cubed sphere projection, designed in *Ronchi et al.* (1996), which allows the SEC poles be regularly spaced and the gradients of the SEC pole amplitudes, used to regularise the model, to be calculated with ease.

Once an optimised model and appropriate SEC pole grid were achieved, the model was evaluated at $105°$ magnetic longitude for all times when the selected magnetometer sites were available. This longitude was chosen at it went through the region of highest magnetometer site density, making it the most accurate region of the model. The divergence free current in the east and north directions and the radial magnetic field perturbations where evaluated along the meridian were recorded. The purpose of this study was to analyse the changes within the eastward and westward electrojet due to different polarities of IMF B_y. To achieve this an algorithm was designed that could take an input of the eastward sheet current density profile and identify the electrojet properties every minute. The properties identified are the electrojet boundaries, peak sheet current density, width and the total current through the electrojet. This was done for up to three westward and three eastward electrojets within each east sheet current density profile to enable an investigation into the occurrence of multiple electrojets in one location.

6.2   Results

The purpose of this study is to investigate the explicit B_y effect on electrojet properties using SECS. This section summarises the results produced to address this research question and outlines the conclusions reached.

Chapter 5 has presented and discussed the B_y and seasonal effects on the electrojets detected using the algorithm outlined in section 3.8.

The properties of the primary eastward and westward electrojets are presented and discussed first in section 5.1.1 and 5.1.2, respectively. As expected from the work by *Holappa and Mursula* (2018), the peak sheet current density in the westward electrojet between 1 and 5 MLT, which is comparable to the AL index, shows an explicit B_y effect during the winter. The results depict a stronger peak for B_y positive than for B_y negative. The less significant explicit B_y effect on the AL index observed by *Holappa and Mursula* (2018) during the summer did not manifest in the peak of the westward electrojet. However, there is an explicit B_y effect in the total current through the westward electrojet during the summer and a must stronger effect during the winter.

The B_y effect on the widths of the eastward and westward electrojet has provided a new insight into electrojet dynamics. It has been found that during the summer there is a clear B_y effect on the widths of the electrojets. When B_y is positive the eastward electrojet is wider and when B_y is negative the westward electrojet is wider. Through further analysis, it is found that the change in the poleward boundary under different B_y polarity and magnitude is the primary factor that drives this clear difference in electrojet widths. Using earlier studies on dipole tilt and B_y effects on ionospheric convection the B_y effect on the poleward boundary of the electrojets is attributed an increased occur-

rence of lobe reconnection during the summer. Lobe reconnection driven ionospheric convection cells are greatly influenced by the polarity of B_y and the combination of these cells and typical Dungey cycle driven cells can increase the poleward extent of the eastward electrojet when B_y is positive and the westward electrojet when B_y is negative.

The electrojet detection algorithm finds the properties of up to three westward and three eastward electrojets in each meridian. Section 5.2.1 and 5.2.2 use this information to generate statistics that show the most probable MLT location of multiple electrojets. Separation into season and B_y polarity allowed an investigation into the mechanisms behind the disruption of electrojets. During the winter disruption of the eastward and westward electrojet is found to occur most commonly within the Harang discontinuity and B_y effects on the MLT location of peak probability follows similar trends to substorm onsets, as seen by *Ostgaard et al.* (2011). During the summer the behaviours are much more obscure and there is no easy comparison with substorm onsets. Possible explanations may lie in the effect of lobe reconnection cells, discussed in section 5.1.2, or differences in the conductance in the summer compared to winter that introduce new mechanisms for electrojet disruption and reduce the disruption cause by substorm onsets.

6.3   Concluding Remarks

In conclusion, this study has successfully outlined the advantages and disadvantages of different methodology that can be used for SECS. It has created a user friendly model that can easily be used for further investigations into divergence-free currents. The model output has been used to show clear explicit B_y effects in the properties of eastward and westward electrojets, some of which are in line with prior research and some that are new information that allow increased clarity in the workings of polar ionosphere dynamics within the northern hemisphere. Finally, the detection of multiple electrojets has allowed the disruption of electrojets during the winter to be attributed to the onset of substorms.

Chapter 7

Future Work

The main focus of this project was to develop robust methodology for the analysis of divergence-free currents using the SECS method and incorporate new inversion techniques. There is wide range of opportunities for further study using the techniques discussed. The code written for this thesis has been made available on GitHub, the link for the repository is in appendix A. Subsequently a number of further investigations could be made using this code: a different set of magnetometers could be used, the southern hemisphere divergence-free currents could be investigated or a greater focus could be made on individual events. To address the focus of the Dynamics of the Asymmetric Geospace research group, in which this study took place, conjugate chains of magnetometers in the northern and southern hemisphere, such as Greenland and Antarctica, could be used in further work to investigate the north-south asymmetries in divergence-free currents. Moreover, the difference in the explicit B_y effect on the two hemisphere's westward and eastward electrojets could be investigated. Furthermore, the possibility to expand the base code to allow the integration of satellite magnetometer measurements would allow the modelling of the curl-free currents and, therefore, would allow the full current vector to be investigated.

Not only does the methodology and code available allow for different uses and further development, the data products produced from this study can be investigated and utilised. For example, figure 3.10 shows one substorm event. Over 200 similar time series plots have been produced for substorms observed in the northern hemisphere. As mentioned in section 3.7.1, evidence of ULF waves can be found within these plots and the representation of the divergence-free currents in this way allows a unique view at substorm dynamics. These plots await further investigation and discussion which could find other phenomena within these plots that are yet to be identified.

The investigation of electrojet characteristics within this study has not been done in this way before. In future research a correlation with other data sets and further investigations into the data collected could yield a greater insight into the driving mechanisms for electrojet properties and the influence of electrojet changes on the polar ionosphere and magnetosphere dynamics.

Appendix A

Python Code

The following link: https://github.com/08walkersj/SECpy, is to a GitHub repository containing the code to create the model and analyse the meridian.

Bibliography

Akasofu, S. I. (1964), The development of the auroral substorm, *Planetary and Space Science*, *12*(4), 273–282, doi:10.1016/0032-0633(64)90151-5. 2.2.1

Amm, O. (1997), Ionospheric Elementary Current Systems in Spherical Coordinates and Their Application, *Tech. Rep. 7*, doi:10.5636/jgg.49.947. 3.1, 3.1

Amm, O., and A. Viljanen (1999), Ionospheric disturbance magnetic field continuation from the ground to the ionosphere using spherical elementary current systems, *Earth, Planets and Space*, *51*(6), 431–440, doi:10.1186/BF03352247. 3.1

Angelopoulos, V., J. P. McFadden, D. Larson, C. W. Carlson, S. B. Mende, H. Frey, T. Phan, D. G. Sibeck, K. H. Glassmeier, U. Auster, E. Donovan, I. R. Mann, I. J. Rae, C. T. Russell, A. Runov, X. Z. Zhou, and L. Kepko (2008), Tail reconnection triggering substorm onset, *Science*, *321*(5891), 931–935, doi:10.1126/science.1160495. 2.2.2

Bart, H., I. Koltracht, A. Markus, and L. Rodman (2004), *Linear Algebra and Its Applications: Preface*, *Linear Algebra and Its Applications*, vol. 385, second ed., 1–6 pp., Addison-Wesley, doi:10.1016/j.laa.2004.03.003. 3.5, 3.5, 3.5

Biskamp, D. (1994), Magnetic reconnection, doi:10.1016/0370-1573(94)90110-4. 2.1.1

Crooker, N. U., and F. J. Rich (1993), Lobe cell convection as a summer phenomenon, *Journal of Geophysical Research: Space Physics*, *98*(A8), 13,403–13,407, doi:10.1029/93ja01037. 5.1.2

Dresden, A. (1920), The fourteenth western meeting of the american mathematical society, *Bulletin of the American Mathematical Society*, *26*(9), 385–396, doi:10.1090/S0002-9904-1920-03322-7. 3.5

Frey, H. U., S. B. Mende, V. Angelopoulos, and E. F. Donovan (2004a), Substorm onset observations by IMAGE-FUV, *Journal of Geophysical Research: Space Physics*, *109*(A10), doi:10.1029/2004JA010607. 3.7.1, 3.10, 3.7.1

Frey, H. U., N. Østgaard, T. J. Immel, H. Korth, and S. B. Mende (2004b), Seasonal dependence of localized, high-latitude dayside aurora (HiLDA), *Journal of Geophysical Research: Space Physics*, *109*(A4), A04,303, doi:10.1029/2003JA010293. 5.1.2

Friis-Christensen, E., and J. Wilhjelm (1975), Polar cap currents for different directions of the interplanetary magnetic field in the Y-Z plane, *Journal of Geophysical Research*, *80*(10), 1248–1260, doi:10.1029/ja080i010p01248. 2.4

Fukushima, N. (1994), Some topics and historical episodes in geomagnetism and aeronomy, *Journal of Geophysical Research*, *99*(A10), 19,113, doi:10.1029/94ja00102. 1, 2.9, 2.2.3

Gjerloev, J. W. (2012), The SuperMAG data processing technique, *Journal of Geophysical Research: Space Physics*, *117*(9), doi:10.1029/2012JA017683. 3.6, 3.7, 3.8, 3.9, 3.10, 3.7.1

Harang, L. (1946), The mean field of disturbance of polar geomagnetic storms, *Journal of Geophysical Research*, *51*(3), 353, doi:10.1029/te051i003p00353. 2.2.2

Helman, D. S. (2013), Earth electricity: A review of mechanisms which cause telluric currents in the lithosphere, *Annals of Geophysics*, *56*(5), doi:10.4401/ag-6184. 2.3

Helmholtz, H. (1858), Über Integrale der hydrodynamischen Gleichungen, welche den Wirbelbewegungen entsprechen, *Journal fur die Reine und Angewandte Mathematik*, *1858*(55), 25–55, doi:10.1515/crll.1858.55.25. 1, 2.2.3

Holappa, L., and K. Mursula (2018), Explicit IMF By Dependence in High-Latitude Geomagnetic Activity, *Journal of Geophysical Research: Space Physics*, *123*(6), 4728–4740, doi:10.1029/2018JA025517. 1, 2.4, 5.1, 5.1.1, 5.1.1, 5.1.2, 6.2

Holappa, L., T. Asikainen, and K. Mursula (2020a), Explicit IMF By Dependence in Geomagnetic Activity: Modulation of Precipitating Electrons, *Geophysical Research Letters*, *47*(4), doi:10.1029/2019GL086676. 1

Holappa, L., T. Asikainen, and K. Mursula (2020b), Explicit IMF Dependence in Geomagnetic Activity: Modulation of Precipitating Electrons, *Geophysical Research Letters*, *47*(4), doi:10.1029/2019gl086676. 2.4, 5.1.2

Jones, A. G. (1980), Geomagnetic induction studies in Scandinavia. I. Determination of the inductive response function from the magnetometer array data., *Journal of Geophysics - Zeitschrift fur Geophysik*, *48*(3), 181–194. 3.6.2

Juusola, L., O. Amm, and A. Viljanen (2006), One-dimensional spherical elementary current systems and their use for determining ionospheric currents from satellite measurements, *Earth, Planets and Space*, *58*(5), 667–678, doi:10.1186/BF03351964. 3.1

Juusola, L., K. Kauristie, H. Vanhamäki, A. Aikio, and M. van de Kamp (2016), Comparison of auroral ionospheric and field-aligned currents derived from Swarm and ground magnetic field measurements, *Journal of Geophysical Research A: Space Physics*, *121*(9), 9256–9283, doi:10.1002/2016JA022961. 3.6.2, 6.1

King, J. H., and N. E. Papitashvili (2005), Solar wind spatial scales in and comparisons of hourly Wind and ACE plasma and magnetic field data, *Journal of Geophysical Research: Space Physics*, *110*(A2), A02,104, doi:10.1029/2004JA010649. 4.1, 5.1, 5.1.1, 5.2, 5.3, 5.4, 5.1.1, 5.5, 5.6, 5.1.2, 5.1.2, 5.2.1, 5.2.1, 5.2.1

Kissinger, J., F. D. Wilder, R. L. McPherron, T. S. Hsu, J. B. Baker, and L. Kepko (2013), Statistical occurrence and dynamics of the Harang discontinuity during steady magnetospheric convection, *Journal of Geophysical Research: Space Physics*, *118*(8), 5127–5135, doi:10.1002/jgra.50503. 2.2.2

Koskinen, H. E. J., and T. I. Pulkkinen (1995), Midnight velocity shear zone and the concept of Harang discontinuity, *Journal of Geophysical Research*, *100*(A6), 9539, doi:10.1029/95ja00228. 2.2.2, 2.8

Koustov, A. V., K. N. Yakymenko, and P. V. Ponomarenko (2017), Seasonal effect for polar cap sunward plasma flows at strongly northward IMF Bz, *Journal of Geophysical Research: Space Physics*, *122*(2), 2530–2541, doi:10.1002/2016JA023556. 5.1.2

Kulsrud, R. M. (2001), Magnetic reconnection: Sweet-Parker versus Petschek, *Earth, Planets and Space*, *53*(6), 417–422, doi:10.1186/BF03353251. 2.1.1

Laundal, K., J.-H. Yee, V. G. Merkin, J. W. Gjerloev, H. Vanhamäki, J. P. Reistad, M. Madelaire, and K. Sorathia (2020), Electrojet estimates from mesospheric magnetic field measurements, doi:10.1002/ESSOAR.10504160.1. 3.2, 3.7, 6.1

Laundal, K. M., and M. Toresen (2018), klaundal/pyAMPS: pyAMPS 0.1.0, doi:10.5281/ZENODO.1182931. 4.1, 4.1

Laundal, K. M., S. E. Haaland, N. Lehtinen, J. W. Gjerloev, N. Østgaard, P. Tenfjord, J. P. Reistad, K. Snekvik, S. E. Milan, S. Ohtani, and B. J. Anderson (2015), Birkeland current effects on high-latitude ground magnetic field perturbations, *Geophysical Research Letters*, *42*(18), 7248–7254, doi:10.1002/2015GL065776. 2.2.3, 3.1

Liou, K. (2010), Polar Ultraviolet Imager observation of auroral breakup, *Journal of Geophysical Research: Space Physics*, *115*(12), n/a–n/a, doi:10.1029/2010JA015578. 2.2.2, 3.7.1, 3.10, 3.7.1

Liou, K., T. Sotirelis, and E. Mitchell (2020), Control of the East-West Component of the Interplanetary Magnetic Field on the Occurrence of Magnetic Substorms, *Geophysical Research Letters*, *47*(5), doi:10.1029/2020GL087406. 1

Loureiro, N. F., and D. A. Uzdensky (2015), Magnetic reconnection: From the Sweet-Parker model to stochastic plasmoid chains, *Plasma Physics and Controlled Fusion*, *58*(1), 014,021, doi:10.1088/0741-3335/58/1/014021. 2.1.1

McPherron, R. L. (1970), Growth Phase of Magnetospheric Substorms, *Journal of Geophysical Research: Space Physics*, *75*(28), doi:https://doi.org/10.1029/JA075i028p05592. 2.2.1

Milan, S., M. Lester, T. Yeoman, T. R. Robinson, M. Uspensky, and J.-P. Villain (2004), HF radar observations of high-aspect angle backscatter from the E-region, *Ann. Geophys.*, *22*, doi:10.5194/angeo-22-829-2004. 2.1

Milan, S. E., L. B. Clausen, J. C. Coxon, J. A. Carter, M. T. Walach, K. Laundal, N. Østgaard, P. Tenfjord, J. Reistad, K. Snekvik, H. Korth, and B. J. Anderson (2017), Overview of Solar Wind–Magnetosphere–Ionosphere–Atmosphere Coupling and the Generation of Magnetospheric Currents, doi:10.1007/s11214-017-0333-0. 2.2, 2.6

Newell, P. T., and J. W. Gjerloev (2011a), Evaluation of SuperMAG auroral electrojet indices as indicators of substorms and auroral power, *Journal of Geophysical Research: Space Physics*, *116*(12), doi:10.1029/2011JA016779. 3.10, 3.7.1

Newell, P. T., and J. W. Gjerloev (2011b), Substorm and magnetosphere characteristic scales inferred from the SuperMAG auroral electrojet indices, *Journal of Geophysical Research: Space Physics*, *116*(12), n/a–n/a, doi:10.1029/2011JA016936. 3.10, 3.7.1

Ohma, A., J. P. Reistad, and S. M. Hatch (2020), Modulation of magnetospheric substorm frequency : Dipole tilt and IMF B y effects, *Submitted to Geophysical Research Letters*, pp. 1–13, doi:10.1002/ESSOAR.10503810.3. 2.4

Ostgaard, N., K. M. Laundal, L. Juusola, A. Åsnes, S. E. Håland, and J. M. Weygand (2011), Interhemispherical asymmetry of substorm onset locations and the interplanetary magnetic field, *Geophysical Research Letters*, *38*(8), n/a–n/a, doi:10.1029/2011GL046767. 5.2.2, 5.13, 5.2.2, 6.2

Østgaard, N., J. P. Reistad, P. Tenfjord, K. M. Laundal, T. Rexer, S. E. Haaland, K. Snekvik, M. Hesse, S. E. Milan, and A. Ohma (2018), The asymmetric geospace as displayed during the geomagnetic storm on 17 August 2001, *Annales Geophysicae*, *36*(6), 1577–1596, doi:10.5194/angeo-36-1577-2018. 5.1.2

Penrose, R. (1955), A generalized inverse for matrices, *Mathematical Proceedings of the Cambridge Philosophical Society*, *51*(3), 406–413, doi:10.1017/S0305004100030401. 3.5

Pettigrew, E. D., S. G. Shepherd, and J. M. Ruohoniemi (2010), Climatological patterns of high-latitude convection in the Northern and Southern hemispheres: Dipole tilt dependencies and interhemispheric comparisons, *Journal of Geophysical Research: Space Physics*, *115*(7), doi:10.1029/2009JA014956. 5.1.2, 5.9, 5.1.2

Pulkkinen, A., O. Amm, and A. Viljanen (2003a), Separation of the geomagnetic variation field on the ground into external and internal parts using the spherical elementary current system method, *Earth, Planets and Space*, *55*(3), 117–129, doi:10.1186/BF03351739. 2.3, 3.6.2

Pulkkinen, A., O. Amm, and A. Viljanen (2003b), Separation of the geomagnetic variation field on the ground into external and internal parts using the spherical elementary current system method, *Earth, Planets and Space*, *55*(3), 117–129, doi:10.1186/BF03351739. 3.6.1, 3.6.2, 6.1

Reistad, J. P., K. M. Laundal, N. Østgaard, A. Ohma, E. G. Thomas, S. Haaland, K. Oksavik, and S. E. Milan (2019), Separation and Quantification of Ionospheric Convection Sources: 2. The Dipole Tilt Angle Influence on Reverse Convection Cells During Northward IMF, *Journal of Geophysical Research: Space Physics*, *124*(7), 6182–6194, doi:10.1029/2019JA026641. 5.1.2

Reistad, J. P., K. M. Laundal, A. Ohma, T. Moretto, and S. E. Milan (2020), An Explicit IMF B y Dependence on Solar Wind-Magnetosphere Coupling, *Geophysical Research Letters*, *47*(1), doi:10.1029/2019GL086062. 1, 2.4

Richmond, A. (1995), Ionospheric Electrodynamics, in *Handbook of Atmospheric Electrodynamics*, vol. 1, edited by Hans Volland, pp. 249–290, CRC Press, doi:10.1201/9780203713297. 2.7

Richmond, A. D. (2007), Ionosphere, in *Encyclopedia of Geomagnetism and Paleomagnetism*, pp. 452–454, Springer Netherlands, doi:10.1007/978-1-4020-4423-6{_}159. 2.5

Robinson, R. M., R. R. Vondrak, K. Miller, T. Dabbs, and D. Hardy (1987), On calculating ionospheric conductances from the flux and energy of precipitating electrons, *Journal of Geophysical Research*, *92*(A3), 2565, doi:10.1029/ja092ia03p02565. 2.2

Ronchi, C., R. Iacono, and P. S. Paolucci (1996), The ".Cubed sphere": A new method for the solution of partial differential equations in spherical geometry, *Journal of Computational Physics*, *124*(1), 93–114, doi:10.1006/jcph.1996.0047. 3.2, 6.1

Russell, C. T., and R. L. McPherron (1973), Semiannual variation of geomagnetic activity, *Journal of Geophysical Research*, *78*(1), 92–108, doi:10.1029/ja078i001p00092. 5.1.2

Seki, K., A. Nagy, C. M. Jackman, F. Crary, D. Fontaine, P. Zarka, P. Wurz, A. Milillo, J. A. Slavin, D. C. Delcourt, M. Wiltberger, R. Ilie, X. Jia, S. A. Ledvina, M. W. Liemohn, and R. W. Schunk (2015), A Review of General Physical and Chemical Processes Related to Plasma Sources and Losses for Solar System Magnetospheres, doi:10.1007/s11214-015-0170-y. 2.4

Shang, W. S., B. B. Tang, Q. Q. Shi, A. M. Tian, X. Y. Zhou, Z. H. Yao, A. W. Degeling, I. J. Rae, S. Y. Fu, J. Y. Lu, Z. Y. Pu, A. N. Fazakerley, M. W. Dunlop, G. Facskó, J. Liu, and M. Wang (2020), Unusual Location of the Geotail Magnetopause Near Lunar Orbit: A Case Study, *Journal of Geophysical Research: Space Physics*, *125*(4), doi:10.1029/2019JA027401. 2.1.2

SILSO World Data Center (0), The International Sunspot Number, *International Sunspot Number Monthly Bulletin and online catalogue*, p. {}. 4.4, 4.5

Taltavall, T. R. (1915), Aurora and Earth currents, *Telegr. Teleph. Age Telegr. Teleph. Radio*, *33*(23), 549. 2.3

Tanskanen, E. I., A. Viljanen, T. I. Pulkkinen, R. Pirjola, L. Häkkinen, A. Pulkkinen, and O. Amm (2001), At substorm onset, 40% of AL comes from underground, *Journal of Geophysical Research: Space Physics*, *106*(A7), 13,119–13,134, doi:10.1029/2000ja900135. 2.3

Untiedt, J., and W. Baumjohann (1993), Studies of polar current systems using the IMS Scandinavian magnetometer array, *Space Science Reviews*, *63*(3-4), 245–390, doi:10.1007/BF00750770. 3.1

Vanhamäki, H., and L. Juusola (2020), Introduction to Spherical Elementary Current Systems, in *Ionospheric Multi-Spacecraft Analysis Tools*, pp. 5–33, Springer International Publishing, doi:10.1007/978-3-030-26732-2{_}2. 1, 3.1, 3.1, 3.2, 3.1.2

Vanhamäki, H., O. Amm, and A. Viljanen (2003), One-dimensional upward continuation of the ground magnetic field disturbance using spherical elementary current systems, *Earth, Planets and Space*, *55*(10), 613–625, doi:10.1186/BF03352468. 3.1.1

Vasyliunas, V. M. (2012), The physical basis of ionospheric electrodynamics, *Annales Geophysicae*, *30*(2), 357–369, doi:10.5194/angeo-30-357-2012. 2.2

Vasyliunas, V. M., and P. Song (2005), Meaning of ionospheric Joule heating, *Journal of Geophysical Research: Space Physics*, *110*(A2), 2301, doi:10.1029/2004JA010615. 2.2

Vennerstrøm, S., and E. Friis-Christensen (1987), On the role of IMF B y in generating the electric field responsible for the flow across the polar cap, *Journal of Geophysical Research*, *92*(A1), 195, doi:10.1029/ja092ia01p00195. 2.4

Wang, Y. (2016), Introduction, in *Magnetic Cloud Boundary Layers and Magnetic Reconnection*, pp. 1–21, Springer Berlin Heidelberg, Berlin, Heidelberg, doi:10.1007/978-3-662-48310-7{_}1. 2.1, 2.2

Wilder, F. D., C. R. Clauer, and J. B. Baker (2010), Polar cap electric field saturation during interplanetary magnetic field Bz north and south conditions, *Journal of Geophysical Research: Space Physics*, *115*(10), n/a–n/a, doi:10.1029/2010JA015487. 5.1.2

Wolfe, J. H., and D. S. Intriligator (1970), The solar wind interaction with the geomagnetic field, *Space Science Reviews*, *10*(4), 511–596, doi:10.1007/BF00172537. 2.3

Yakymenko, K. N., A. V. Koustov, and R. A. Fiori (2018), Interhemispheric Asymmetry of the Sunward Plasma Flows for Strongly Dominant IMF BZ > 0, *Journal of Geophysical Research: Space Physics*, *123*(1), 315–325, doi:10.1002/2017JA024644. 5.1.2